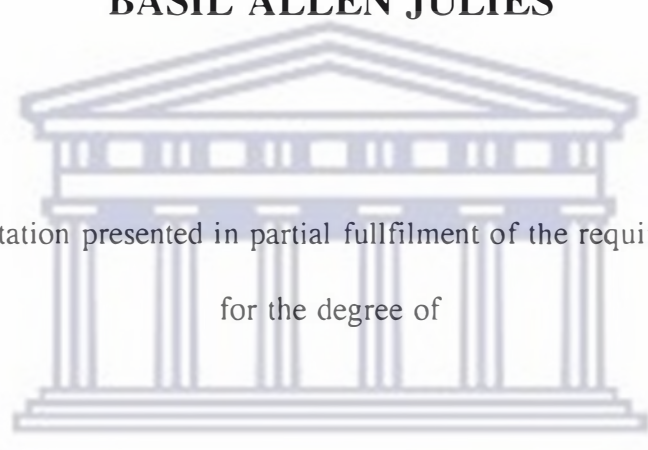# CROSS-SECTIONAL TRANSMISSION ELECTRON

MICROSCOPY

OF NICKEL SILICIDE FORMATION

BY

BASIL ALLEN JULIES

Dissertation presented in partial fullfilment of the requirements

for the degree of

MASTER OF SCIENCE

to the

DEPARTMENT OF PHYSICS

UNIVERSITY OF THE WESTERN CAPE

Promotor : Prof. D. Knoesen
Co-promotor : Dr. R. Pretorius

NOVEMBER 1993

"I declare that

CROSS-SECTIONAL TRANSMISSION ELECTRON MICROSCOPY

OF

NICKEL SILICIDE FORMATION

is my own work and that all the sources I have used or quoted have been indicated and acknowledged by means of complete references."

To my parents

ACKNOWLEDGEMENTS

ABSTRACT

Silicides play a significant role in modern device technology. The operation of electronic devices heavily relies on the specific properties of metal-semiconductor interfaces. Although semiconductor technology has proven very successful in utilizing the properties of materials the knowledge on formation, structure and electrical behaviour of interfaces is still far from complete. In this study an investigation into the Ni-Si binary system was made. Several techniques namely Rutherford Backscattering Spectroscopy, Transmission Electron Microscopy, Scanning Electron Microscopy, Auger Emission Spectroscopy and X-ray Diffraction were employed in the characterization of nickel thin films on silicon and the respective silicides which were formed. Special attention was given to the phase transition from NiSi to $NiSi_2$.

First phase formation, namely Ni_2Si, was investigated at a vacuum furnace temperature of 290°C. This phase was found to be polycrystalline and grew in layers of uniform thickness with sharp Si-silicide and Ni-silicide interfaces. Growth continued until all the Ni-metal was consumed. Second phase formation (NiSi) was observed at 330°C only after the Ni_2Si has grown to its full thickness. This polycrystalline phase also grows in layers. These layers however, are not of uniform thickness, the interfaces between the silicide and silicon substrate therefore being less regular. It was found that NiSi grains could assume one of two crystal structures, orthorhombic or a FeSi cubic structure. Generally it seems as if NiSi initially crystallizes into an orthorhombic crystal structure, before undergoing an allotropic transformation to the FeSi cubic structure. Micro-diffraction was used to characterize individual grains.

Final phase formation ($NiSi_2$) was mainly examined at 750°C. A scanning electron microscopy investigation showed that after 5 minutes of annealing islands of $NiSi_2$ was observed in a NiSi matrix. With longer annealing times these islands grew laterally and eventually joined up with others. Cross-sectional transmission electron microscopy very firmly confirms the presence of $NiSi_2$ surrounded by NiSi. Rutherford backscattering, X-Ray diffraction and Auger electron spectroscopy complement these results. Scanning electron microscopy shows that after the coalescence of individual $NiSi_2$ islands, holes appear on the grain boundaries. These holes probably result from an accumulation of vacancies on the grain boundaries during $NiSi_2$ formation which occurs via Ni diffusion in NiSi into the underlying silicon. As the $NiSi_2$ phase continues to grow these holes increase in size and later take on the same crystal structure as the surrounding cubic $NiSi_2$ grains. Although the reaction: $NiSi + Si \Rightarrow NiSi_2$ is thermodynamically favourable to occur at 750°C, it was found that even after 15 minutes of annealing at 750°C, some grains were still NiSi while many others had switched to $NiSi_2$. Identification was once again done by micro diffraction. This means that there is more than just the thermodynamic aspect involved in deciding when NiSi should transform to $NiSi_2$. A model has therefore been proposed in which the major factors in determining the time lapse for transformation to take place are presented. This model generally presents an atomistic approach which centres around the degree of Ni diffusion across the grain boundary of two individual grains. Observations also suggests that $NiSi_2$ results from NiSi by a diffusion process although nucleation can take place at random. This model must not be seen as contradictory to models proposed in the literature which only allow for non-uniform growth at the $Si-NiSi_2$ interface, but must rather be seen as complementing it by allowing for diffusion processes as well.

UITTREKSEL

Silisiedes speel 'n belangrike rol in die vervaardiging van Si-gebaseerde mikroelektroniese stroombane veral in die spesifieke eienskappe van metaal-halfgeleier intervlakke. Alhoewel die toepassing van materiale in die halfgeleier tegnologie besonder suksesvol is ,is daar nog steeds 'n gebrek aan kennis aangaande die vorming, struktuur en elektriese karakteristieke van intervlakke. In hierdie studie word die Ni-Si binêre sisteem ondersoek. Verskeie tegnieke onder andere Rutherfordterugvertrooiing, Transmissie Elektronmikroskopie, ˊ Skandeer Elektronmikroskopie, Auger Elektronspektroskopie en X-Straaldiffraksie was gebruik tydens hierdie studie. Die fase oorgang van NiSi na $NiSi_2$ het spesiaale aandag geniet.

Die eerste fase is Ni_2Si wat by 'n temperatuur van 290°C vorm. Hierdie fase is polikristallyn en groei in lagies van uniformige diktes met skerp, definitiewe intervlakke. Groei vind plaas totdat al die Ni-metaal opgebruik is. Die vorming van die tweede fase by 330°C vind plaas slegs nadat die Ni_2Si lagie sy maksimum dikte bereik het en groei ook in lagies wat polikristallyn van aard is. Hierdie lagies is egter nie uniform in dikte nie en dus is die intervlakke ook nie reëlmatig nie. In hierdie ondersoek is daar ook gevind dat NiSi korrels een van twee kristalstrukture kon aanneem, naamlik 'n orthorombiese of 'n FeSi kubiese struktuur. Oor die algemeen kom dit voor of NiSi eers in 'n orthorombiese kristalstruktuur kristalliseer voordat dit 'n allotropiese transformasie na die FeSi kubiese struktuur ondergaan. Mikrodiffraksie is gebruik om die individuele korrels te identifiseer.

Die finale fase naamlik $NiSi_2$ was grotendeels by 'n temperatuur van 750°C ondersoek. 'n Skandeer elektronmikroskopie studie dui aan dat $NiSi_2$ eilande in 'n NiSi matriks na 5 minute se verhitting waargeneem word. By verdere verhitting vind laterale groei plaas totdat die eilande uiteindelik met mekaar saamsmelt. Transmissie elektronmikroskopie bevestig die teenwoordigheid van $NiSi_2$ in 'n NiSi matriks. Rutherford-terugverstrooiing, X-straal diffraksie en Auger elektronspektroskopie ondersteun hierdie resultate. Na samesmelting van die individuele $NiSi_2$ eilande, word gate op die korrelgrense gevorm, waarskynlik deur akkumulasie van vakatures op die korrelgrense tydens $NiSi_2$ formasie en deur die diffusie van Ni in NiSi na die onderliggende Si. Hierdie openinge neem toe in grootte tydens $NiSi_2$ groei en neem later dieselfde kubiese kristalstruktuur as die omliggende $NiSi_2$ aan. Alhoewel die reaksie: $NiSi + Si \Rightarrow NiSi_2$ bevoordeel word by 750°C word gevind dat na 15 minute se verhitting by hierdie temperatuur, sommige korrels steeds NiSi is terwyl ander alreeds na $NiSi_2$ oorgeskakel het. Dit impliseer dat die termodinamiese aspek nie die enigste proses is wat in ag geneem moet word tydens die oorskakeling na die finale fase nie. 'n Model is dienooreenkomstig voorgestel waarin die belangrikste faktore vir transformasie in ag geneem is. Die model maak gebruik van 'n atomistiese benadering wat gebaseer is op die mate van Ni diffusie oor die korrelgrens van twee individuele korrels. Die resultate stel voor dat $NiSi_2$ vanaf NiSi deur 'n diffusie proses gevorm word alhoewel nukleasie willekeurig plaas kan vind. Hierdie model moet nie gesien word in teenstelling met modelle uit die literatuur nie, maar moet eerder gesien word as aanvullend aangesien dit ook diffusie prosesse in ag neem.

CONTENTS

CHAPTER 1

INTRODUCTION, BACKGROUND AND SCOPE OF THE INVESTIGATION

1.1   IMPORTANCE OF THIN FILM STRUCTURES

The invention of the transistor in 1947 [OS-90] and the development of integrated circuits in 1958 [vdH-88] are undoubtedly responsible for the transition from the industrial era to the information era.   Since its introduction 15 years ago as a technique for microelectronics fabrication, the Very Large Scale Integration (VLSI) technology has become the cornerstone of various electronics systems including the two most vital technologies of the information society, namely computers and communication systems.   Microelectronics circuits are characterised by their complexity (measured by the number of components per chip which increases with chip size (and packing density) and performance (reflected in high speed and low power consumption).   Today the demand on the system-oriented chips from the electronics industry, is pushing the physical dimension of the components and the chips complexity to their extremes (see fig 1.1).   The Metal-Oxide-Semiconductor (MOS) transistors are generally considered the technology driver of the miniaturization.   They are characterized by low power consumption and high packing density, and are challenging bipolar transistors in terms of device speed [Os-82].

Transition metal-silicon thin film systems have been investigated extensively, with emphasis placed on the utilization of metal silicides as ohmic or Schottky contacts, interconnects and gates in Si devices [Mu-83].   This is not only because the silicide-Si interface has electrical properties suitable for contacts to very small junctions, but also because the silicide layer can improve junction

reliability by providing an effective barrier against Al penetration into the junction [Tu-78]. In general, materials for metallization applications in Si technology are required to have properties such as

1) low resistivity,

2) process compatibility in terms of depositions, formation, etching and adhesion to another metallization layer,

3) good mechanical stability, in particular good adhesion to Si and SiO_2, and

4) high thermal stability in an inert ambient and preferably also in an oxidizing ambient.
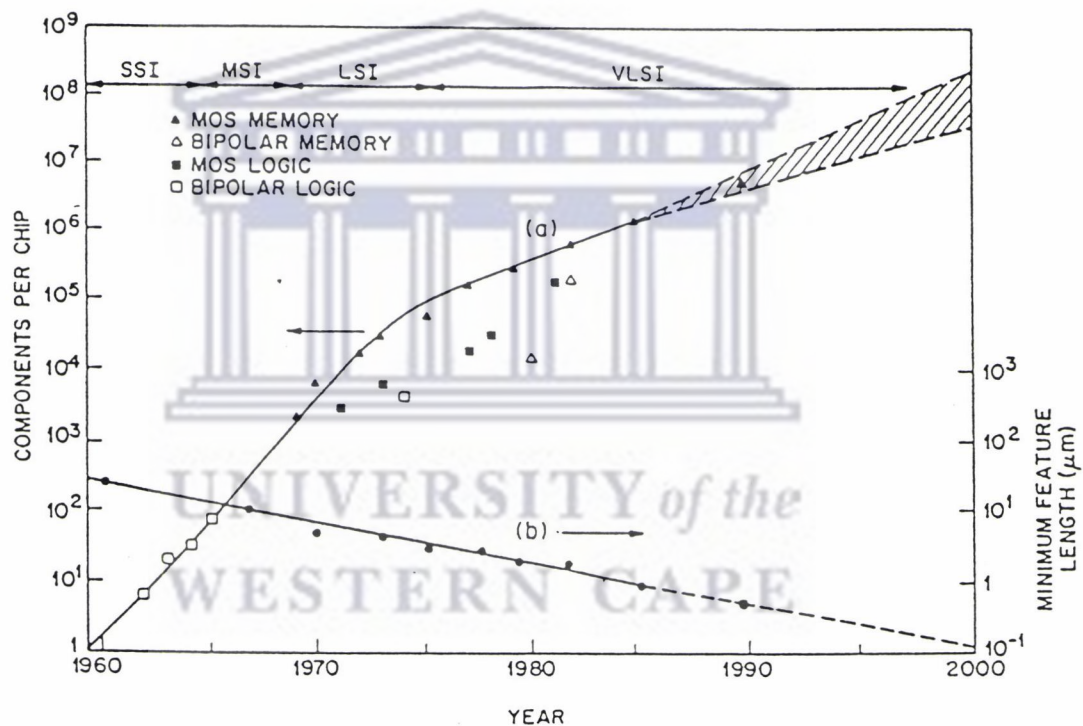
Figure 1.1 : *Development of chips complexity and minimum feature size of the components [Sh-81].*

Furthermore, materials for contact applications are required to have a low barrier height to both n- and p- type silicon (giving low contact resistivity) as well as to consume a minimal part of the junction for contact formation. Materials for gate application should have an adequate work function to Si [Oe-88], whereas interconnection materials should be resistant to damage by high current density.

2

Several of the above mentioned requirements are satisfied by metal silicides which in addition to their low resistivity are characterized by high thermal stability and good contact properties to Si. Even though metals or polysilicon have superior properties in some respects, the overall advantage with silicides makes them increasingly interesting for metallization in the emerging Ultra Large Scale Integration (ULSI) technology. Interfaces occupy a special position regarding the formation of silicide layers and the eventual device performance. They are abrupt transitions (no more than a few atomic layers thick) between layers and represent the chemically reactive zones for silicide formation. As such they are sensitive to the influence of internal stress, intrinsic defects, impurity atoms and the thermodynamic forces of enthalpy and entropy, all of which are factors that exert direct control on interface reactions. It is also in this narrow region that the electronic properties of a device are determined [Br-82]. Research has demonstrated the use of epitaxial silicide layers as VLSI transistors [He-85]. $NiSi_2$ is one of the most studied silicide systems, particularly due to its electronic properties and excellent epitaxial behaviour on single crystal silicon. Research on silicide forming systems is an ongoing activity not only to serve academic understanding but also in response to stimulation from technology and its needs.

1.2   METAL SILICIDE FORMATION

Many silicides can be formed by solid-state reaction of metal and Si at a temperature well below the eutectic temperature of the system [Co-82]. Usually silicide formation is obtained with either isothermal furnace annealing or Rapid Thermal Annealing (RTA). Other techniques such as laser, electron beam and ion beam mixing can also be used to induce the silicide formation [Ar-77]. From a thermodynamic point of view, the formation process is a consequence of the free energy decrease in such a reaction, and some external energy input can substantially accelerate the silicide formation by changing the thermodynamic energy of the system. When a metal in contact with silicon is heated and a metal silicide is formed, the phase of the silicide depends on the temperature of formation (see fig 1.2). The reaction occurs between two different kinds of solids: the silicon substrate which is covalently bonded single crystal, and the thin film which is metallic and fine grained. Three different classes of silicides are

3

mainly found, namely metal-rich silicides, monosilicides and disilicides, which typically start to form at about 200, 400 and 600°C respectively [Tu-78]. In figure 1.2 the formation of cobalt silicide at various temperatures is illustrated. The metal-rich Co_2Si forms at approximately 350°C. Upon further heat treatment the monosilicide, CoSi,

eg Co:

$$Co + Si\ (100) \longrightarrow Co_2Si \longrightarrow CoSi \longrightarrow CoSi_2$$
$$350°C \qquad 425°C \qquad 550°C$$
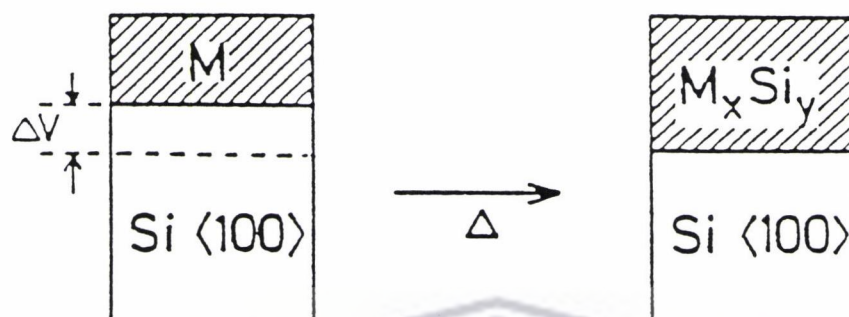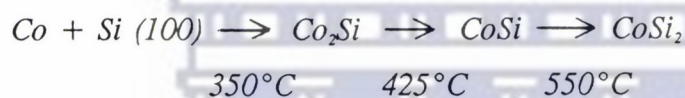
Figure 1.2 : *Schematic diagram of metal silicide formation.*

forms at about 425°C and the disilicide, $CoSi_2$ at about 550°C. The latter phase is called the "end phase" as no further change in phase occurs at higher temperatures.

1.3 DIFFUSING SPECIES

During metal silicide formation mass transport is facilitated by the movement of an atomic species in the diffusion couple. The specific transport mechanism and the diffusing species involved in any such interaction are to a large extent intrinsic properties of the specific binary system. In a silicon - metal binary system the silicide phase can grow by metal diffusion, silicon diffusion, or both. The specific diffusion mechanism and the degree to which a certain atomic species contributes to mass transport, are dependent on sample characteristics such as crystal structure, thermodynamic properties, chemical reactivity, the relative availability of reactants, etc. It is, however, possible to tailor experimental conditions to enforce different formation mechanisms and to change the dominant diffusing species of specific interactions. It was for instance shown that by introducing gold into the Co-Si binary system, a change

4

of both the growth mechanism and the identity of the diffusing species was brought about during $CoSi_2$ formation [Ra-87].

As further identification of the diffusing species in different phase formations, both inert markers and radioactive tracers are utilized to provide complementary information on the diffusing species in different phases. When using inert markers, conclusions concerning the identity of the moving species can be derived purely from the direction of marker displacement during growth of the respective silicide phases. Additional information regarding the possible diffusion mechanisms involved in any specific case are obtained by using radioactive silicon or radioactive metal markers [Pr-81, Ba-82]. Some of the marker results reported are summarized in table 1.1 below. The experimental evidence thus point to the fact that the metal atoms are the major moving species during the growth of Ni_2Si, NiSi and $NiSi_2$.

1.4 DIFFUSION MECHANISMS

There are two main approaches to diffusion theory:

(1)   the atomistic approach, where the atomic nature of the diffusing substance is explicitly considered; and

(2)   the continuum approach, where the diffusing substance is treated as a continuous medium and the atomic nature of the diffusion process is ignored [Ma-68]. Many useful equations result from the continuous approach. For example, general thermodynamic equations can be found which relate diffusion fluxes to thermodynamic driving forces.

This approach in one sense simplifies the problem since it directly relates the initial and final states, but is limited in its results since it ignores the details of the atomic motions. In order to obtain a more complete picture of diffusion phenomena, the atomistic approach will now be considered.

In any crystal, there is a regular array of lattice sites which are energetically favoured

5

positions for atoms. The basic assumption made to explain diffusion is that each diffusing atom makes a series of jumps between the various equilibrium lattice sites.

Table 1.1 : *Marker experiments used to study nickel silicide formation on single crystal silicon.*

SILICIDE	DIFFUSING SPECIES	MARKER OR TRACER	REFERENCES
Metal-rich-silicide	Ni	Xe	[Ce-74,Tu-75,Ch-75,Tu-77]
Ni_2Si	Ni	^{31}Si	[Pr-71,Pr-78]
	Ni	^{56}Ni	[Ba-81]
	Ni	Ag	[Hu-85]
	Ni	^{31}Si	[Pr-80]
	Ni	W	[Af-85]
Mono-silicide	Ni	Xe	[Fi-81]
	Ni	^{56}Ni	[Ba-82]
NiSi	Ni	^{31}Si	[Bo-82(a)]
	Ni	Pt	[Fi-78]
	Ni	^{16}O	[Sc-81]
Disilicide	Ni	Xe	[d'H-82]
	Ni	^{56}Ni	[Ba-82]
$NiSi_2$	Ni	W	[Li-83]
	Ni	$Xe,^{18}O$	[Li-84(a)]

The theory of specific heats clearly demonstrates that atoms oscillate around these lattice sites. The jumps can therefore come about if the oscillations become large enough. These jumps are in more or less random directions and allow the atoms to migrate through the crystal. Since the presence of defects in a crystal normally accounts for the mobility of atoms in crystal lattices, diffusion does not occur in a perfect crystal. The direct exchange mechanism and the ring mechanism (explained later in this section) are special mechanisms which may be described as defect independent processes, mainly because the defect, a vacancy, is created and destroyed at the same time. Basic diffusion mechanisms [Bo-82(a)] in crystals are listed in Table

6

1.2 and some of them are illustrated in figures 1.3(a)-(h).

Table 1.2 : *Basic diffusion mechanisms in crystals.*

TYPE	DEFECT INVOLVED	MECHANISM
Defect independent processes	—	Direct exchange Ring
Defect dependent processes	Interstitial	Direct interstitial Interstitialcy (indirect interstitial) Crowdian Dissociative
	Vacancy	Vacancy* Divacancy Relaxation
	Line and Surface	Pipe diffusion Surface diffusion Grain boundary diffusion*

* Most common mechanisms in nickel silicide formation.

Vacancy mechanism

In thermal equilibrium, any crystal at a temperature above absolute zero contains a certain number of vacant lattice sites. These vacancies provide an easy path for diffusion.

The elementary atom jump in the vacancy mechanism is the jump of an atom into a neighbouring vacancy (see figure 1.3(a)). The site previously occupied by the atom then is vacant, so that in effect the atom and vacancy merely exchange positions.
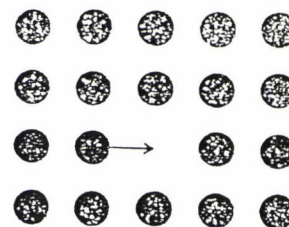
Figure 1.3(a) : *Vacancy mechanism, elementary jump.*

7

Grain boundary diffusion

The term grain boundary diffusion refers to atomic movement occurring in the interfacial region separating two grains. Grain boundaries provide high mobility routes for atomic migration relative to lattice diffusion. The extent to which lattice diffusion influences the material transport along grain boundaries determines the kinetic regime which prevails [Gu-78]. The three types of kinetics, called A, B and C are illustrated in figure 1.3(b).
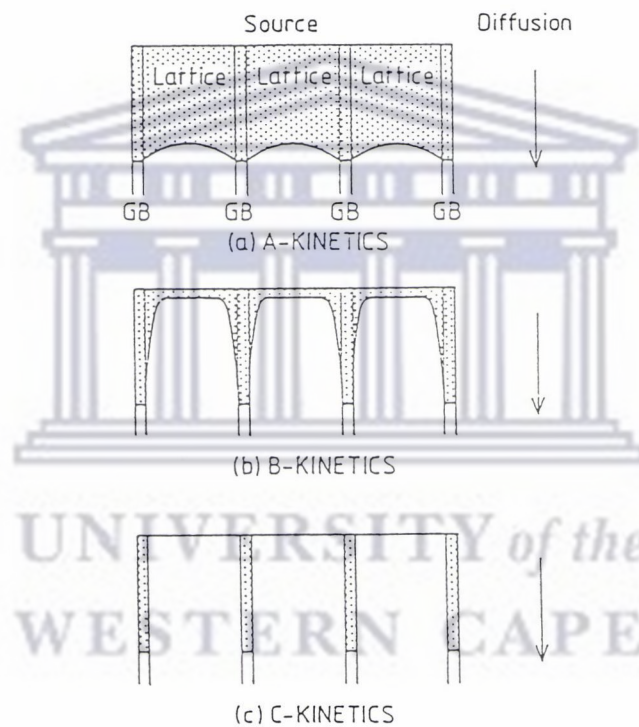
Figure 1.3(b) : *Schematic representation of the three types of grain boundary kinetics, namely (a) A-Kinetics showing grain boundary diffusion with extensive lattice diffusion, (b) B-Kinetics, where each boundary is assumed to be isolated and the diffusion flux at large distances in the lattice is very small, and (c) C-kinetics where lattice diffusion is considered negligible and significant atomic transport occurs only within the grain boundaries. (Note that vertical line indicate grain boundaries and curved lines are isoconcentration contours, while the diffusion source coincides with the top horizontal lines.)*

8

The distinguishing feature of A-Kinetics is the extensive contribution of lattice diffusion. The grain boundaries are shown here as parallel slabs. In the B-Kinetics each grain boundary is assumed to be isolated and the flux at large distances in the grains is very small. In C-Kinetics, lattice diffusion is considered negligible and significant atomic transport occurs only within the grain boundaries.

The deciding factor for A,B or C-Kinetics to occur depends on the grain boundary density, the diffusion time and temperature and the type of source (finite or infinite). Measurements in bulk materials invariably involve B-Kinetics [Sh-73, Gu-78]. Due to the very high density of structural defects such as grain boundaries in thin films, all three types of kinetics may be observed in thin film systems. The above described atomistic theory of diffusion is successful in giving a qualitative description of the atomic motion and diffusion mechanisms.

Exchange mechanism

This is possibly the simplest mechanism one can envisage for the elementary jump is the direct interchange of two neighbouring atoms as illustrated in figure 1.3 (c). This mechanism is unlikely in crystals with tightly packed atom structures since each atom in this case in closely surrounded and hemmed in by its neighbours. The atoms would need to be considerably compressed before any two could squeeze past one another and interchange positions.

Figure 1.3(c) : *Exchange mechanism*

Ring mechanism

In the Ring mechanism a number of atoms (three or more) which are situated roughly in a ring move together so that the whole ring of atoms rotates by one atom distance (figure 1.3(d)). The compressions required here are not as great as in a direct exchange mechanism.
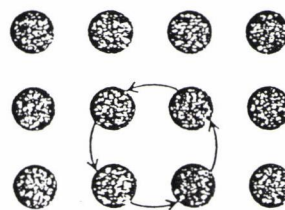
Figure 1.3(d) : *Ring mechanism*

9

Direct interstitial mechanism

In the direct interstitial mechanism, an atom moves through the crystal by jumping directly from one interstitial site to another as illustrated in Figure 1.3(e). This mechanism is particularly likely for diffusion of small impurity atoms, which easily fit into interstitial sites and in jumping do not greatly displace the solvent atoms from their normal lattice sites. This
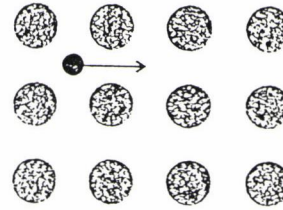
Figure 1.3(e) : *Interstitial mechanism.*

mechanism requires less energy to operate than in the previous two mechanisms.

Interstitialcy Mechanism

When the interstitial atom is nearly equal in size to the lattice atoms, diffusion is more likely to occur by the interstitialcy mechanism, also called the indirect interstitial mechanism. Here the interstitial atom does not move directly to another interstitial site. Instead it moves into a normal lattice site and the atom which was originally at the lattice site is pushed into a neighbouring interstitial site as illustrated in figure 1.3(f). Thus two jumps of the interstitialcy are required to move an atom from one lattice site to another.
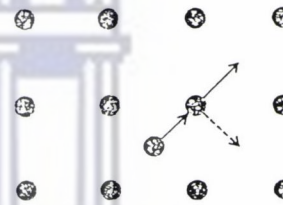
Figure 1.3(f) : *Interstitialcy mechanism. The solid arrows show displacements of the diffusing atoms during an elementary jump in a collinear interstitialcy mechanism. The dotted arrow shows an alternative (non collinear) motion for the lattice atom.*

Dissociative mechanism

The diffusing atoms occupy both substitutional and interstitial sites in this mechanism, but they are only mobile by the direct interstitial mechanism, when present in the interstitial sites.

Divacancy mechanism

The divacancy mechanism occurs when two isolated vacancies are bound together so that adjacent lattice sites are vacant. Diffusion can then proceed by these vacancies as

10

a pair, especially at high temperatures.

Crowdion mechanism

The crowdion mechanism is a type of interstitial configuration in which the additional atom is introduced into a more or less close-packed row of atoms (figure 1.3(g)). Each atom in the row, to perhaps ten atom distances from the additional atom, is displaced somewhat from the equilibrium lattice position. The crowdion configuration can move along this row. In passing down a row from one end to the other, the crowdion displaces each atom in the row one atomic distance.
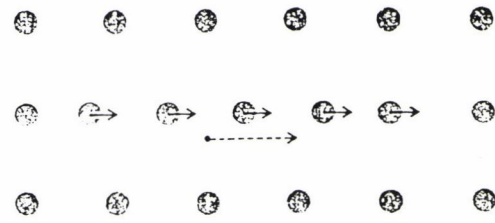
Figure 1.3(g) : Crowdion mechanism. The solid arrows show the atom displacements during an elementary jump in the crowdion mechanism. The dashed arrow gives the displacement of the center of the Crowdion imperfection.

Relaxation mechanism

If the atoms in the region of a vacancy relax inward into the vacant lattice site to such an extent that the regular lattice structure in this region disappears up to several atom distances, the resulting region is called a relaxation. This might be compared with a localized melting, leading to disorder within this region. The atoms in this region can diffuse by an irregular jostling motion similar to that for atoms in a liquid. This is illustrated in figure 1.3(h).

Figure 1.3(h) : *Relaxation mechanism. Atoms within the relaxed area move some what as in a liquid.*

Pipe diffusion

Isolated dislocations provide high mobility routes for atom migration relative to lattice diffusion. Diffusion along an edge screw or mixed dislocation is called pipe diffusion.

Surface diffusion

This mechanism includes diffusion along external and internal surfaces. Internal surfaces can be classified as grain boundaries and phase boundaries.

11

1.5 PHASE FORMATION SEQUENCE

During a solid-state reaction between silicon and metal thin films, the various silicide compounds as portrayed in the equilibrium phase diagram form in a sequential rather than in a simultaneous fashion as it occurs in bulk material [Ni-83, Tu-78]. The first phase to form when near noble metals are deposited on bulk silicon is normally a metal-rich silicide (eg. Co_2Si, Pd_2Si and Pt_2Si [Ma-80]). However, not all systems have M_2Si (M = metal) as the first phase to form. The monosilicides (MSi) were found to be the first phases to form for Fe [La-75], Mn [Su-73], Rh [Ni-83], Ir [Pe-79] and Hf [Ki-73]. After the first compound is formed, it will react with the remaining silicon to form more silicon rich compounds. The second phase then grows at the expense of the first. It has been shown that the initial growth of a specific phase on the one hand, and the relative growth or shrinkage of another co-existing phase on the other, depends on the growth conditions at the interfaces [Gö-82]. Any restriction on the supply of the reacting species would result in the nucleation and growth of another phase, which would be richer in the unlimited element. Such restrictions occur with thin films on a thick substrate.

1.6 MODELS FOR PREDICTING FIRST PHASE FORMATION

There has been considerable interest in predicting the first silicide phase to form and the sequence of subsequent phase formation in binary thin-film systems [Be-82,Ot-86]. Unlike the bulk case (involving layers which exceeds 10 μm thickness) not all compound phases present in the equilibrium phase diagram are observed in thin film systems [Pr-90,Ba-78,Ni-83]. In the case of silicides for instance, only one compound phase usually forms between the two components, silicon and metal. An example of this is the Pt-Si system (in which Pt films are deposited onto silicon), where the Pt_2Si layer forms above 200°C with no indication of the presence of the other equilibrium phases as long as both unreacted platinum and silicon are still available [Ni-83,Tu-75]. For bulk diffusion, all the compound phases given by the phase diagram are usually found. Knowledge of phase formation sequences enables the materials scientist to control experimental parameters to make specific results reproducible.

12

1.6.1 The Walser Bené model

One of the first rules for predicting phase formation was that of Walser and Bené [Wa-76]. Walser and Bené postulated that the interface between two adjacent components has an initial concentration which is near the composition of the lowest eutectic temperature in the binary system. According to the Walser and Bené model, *the first phase to nucleate and grow would be the most stable congruently melting compound adjacent to the lowest temperature eutectic on the bulk equilibrium phase diagram. This rule was relatively successful in predicting first phase formation in metal-silicon systems and was extended later by Tsaur et al [Ts-81] to subsequent phase formation sequence. This extended rule states that the next phase to form at the interface between the first phase and the remaining element (silicon or metal) would be the compound with the smallest ΔT that exist in the phase diagram between the composition of the first phase and the unreacted element.* ΔT was defined as the temperature difference between the liquidus curve and the peritectic (or peritectoid) point for the system under consideration. ΔT was considered to be zero for congruently melting compounds. In addition to the Walser-Bené rule it was proposed that the diffusing species and interfacial free energy should also be considered in predicting the first phase to form [Ro-83].

1.6.2 The effective heat of formation model

A much more fundamental approach in predicting first phase as well as subsequent phase formation was adopted by Pretorius [Pr-84] in the proposed Effective Heat of Formation (EHF) model. In this model an effective heat of formation is defined which depends on the available concentration of the reacting atomic species at the growth interface. In the EHF model Pretorius shows how heats of formation, when expressed as an effective heat of formation ($\Delta H'$), can be used in conjunction with the composition of the lowest eutectic (or liquidus minimum) of the metal-silicon binary system, to predict both the first silicide phase and the subsequent phases which form.

The effective heat of formation ($\Delta H'$) can generally be defined as.

13

$$\Delta H' = \Delta H° \times \frac{effective\ concentration\ of\ limiting\ element}{compound\ concentration\ of\ limiting\ element}$$

where $\Delta H°$ is the heat of formation of the formed compound expressed in kJ/g.atom, the units of ΔH therefore being kJ/g.atom.

Pretorius' rule [Pr-84] states that *the first silicide phase to form during metal-silicon interaction is the congruent phase with the most negative effective heat of formation ($\Delta H'$) at the concentration of the lowest eutectic temperature of the binary system. The effective heat of formation rule is extended to incorporate phase sequence stating that: "After first phase silicide formation, the next phase formed at the interface between the compound and the remaining element (Si or metal) is the next congruent phase richer in the unreacted element, which has the most negative effective heat of formation. If the compounds between a formed phase and the remaining element are all non-congruently melting compounds, the next phase that will form is the non-congruent phase with the most negative heat of formation".*

The EHF model has been successfully used in metal-silicon and metal-germanium systems to predict silicide and germanide phases formation sequence [Pr-84, Pr-90(a), Pr-91, Pr-92, Pr-92(a), Ma-93]. The validity of the EHF model has recently been extensively researched by Marais [Ma-93].

1.7 NICKEL SILICIDE FORMATION

1.7.1 Growth Kinetics

A great number of studies have been devoted to metal-silicon thin film reactions in which not only the structure and properties of the phase formed has been covered, but also the kinetics of the reactions [Ci-89]. Kinetics of reaction is divided into two main classes:

1)   Diffusion-controlled kinetics: the main characteristic being that the thickness of

14

the silicide formed increases propotionally to the square root of time; the limiting step is the diffusion of one or both of the components (Ni and Si in the case of Ni-silicides), under a constant driving force (which is the free energy of formation of the compound), through the increasing thickness of the compound layer. The compound layer formation is a fast reaction and the process is determined by the rate at which new atoms arrive at the interaction layer, thus diffusion controlled. For silicides this type of kinetics has been observed for the reaction of silicon - bearing materials with metallic substrates [Ha-65,Ga-65] as well as for the reaction of metallic films with silicon substrates [Gu-77, Tu-78].

2)   Nucleation controlled kinetics: in this the formation of the silicide takes place only at relatively high temperatures in a sudden way. In this case the new phase formation reaction is a slow process, and more than enough atoms is provided by the diffusion process. The rate of formation is the limiting factor, thus nucleation controlled. Under these circumstances the rate at which the components react with one another may be the limiting factor. In such cases the thickness of the compound layer would vary linearly with time. Some compounds are thought to grow, at least initially, according to such reaction- rate-limited kinetics [Lo-73,Kr-74]. In fact quite often the initial growth of a compound layer is likely to be complicated by nucleation phenomena. The formation of a compound layer implies necessarily the formation of new interfaces (from metal-silicon to metal-silicide plus silicide-silicon); whenever the total surface energy of the resulting system of interfaces exceeds the initial surface energy, nucleation is bound to play a significant role in governing the starting kinetics of the growth of a compound layer.

When it comes to practical applications, it is advantageous for a materials scientist to know the rate at which a specific silicide will grow. Much work has been carried out in establishing the kinetics of silicide formation, a review of which is given by Nicolet et al [Ni-83]. The rates of reaction are generally expressed in terms of silicide layer thickness per unit time of growth i.e.

$$X^2 = K(T)t \text{ for diffusion controlled growth} \qquad (1.1)$$

15

or X $=$ K(T)t for nucleation controlled growth (1.2)

where K(T) is the rate constant at a specific temperature, T, in Kelvin; "X" being the thickness of the silicide layer and "t" the time.

The Ni-Si binary system has been studied extensively with regard to the rates of reaction of the various phases. Ni_2Si was found to adopt a $t^{1/2}$ time dependence relationship with respect to layer thickness thereby indicating a diffusion controlled growth [Tu-75, Ol-76, Co-76, Sc-81 (a)]. Diffusion controlled kinetics was also found to govern NiSi formation [Sc-81(a), Sc-81,d'H-84, Ma-84]. The above results were found for polycrystalline silicon substrates as well as for (100) and (111) orientated silicon. In all these cases Rutherford Backscattering Spectrometry was used as the analytical technique. In all cases layer by layer growth were observed for both Ni_2Si and NiSi, NiSi only forming once Ni_2Si has completely grown through the entire film thickness. Experiments reported above were carried out in a temperature of 275-300°C for Ni_2Si formation and 275-350°C for NiSi formation for different times.

In contrast to the diffusion controlled growth for Ni_2Si and NiSi formation as reported above, $NiSi_2$ has been reported to form via a nucleation controlled growth process [Ba-80(a)]. The kinetics of silicide film growth depends to a large extent on the available supply of diffusing nickel or silicon atoms at the growth interface. In general this supply can be influenced by temperature, grain size, substrate orientation, interface cleanliness and thickness of the silicide film [Ba-82]. Baglin et al [Ba-80] suggest that the shift from diffusion controlled kinetics to nucleation controlled kinetics is mainly due to the remarkable volume change from the NiSi to the $NiSi_2$ structure compared to the isomorphic transformation of CoSi to $CoSi_2$ in which $CoSi_2$ growth is diffusion controlled. According to the well known relation, $\Delta G = \Delta H - T\Delta S$, the free energy ΔG can become negative at some pseudo-critical temperature T_c if the ΔS term is positive. Owing to the greater volume change in the transformation from NiSi to $NiSi_2$, the stress-strain contribution to enthalpy is greater in the Ni case than in the case of Co. One can therefore remark that the respective volume changes agree with the observed shift from a diffusion - controlled reaction for $NiSi_2$.

16

The empirical Arrhenius equation relates the rate constant to an activation energy of growth in the following way:

$$K = K_o \, e^{-Q/KT} \tag{1.3}$$

Where K = the pre-exponential factor

Q = the activation energy

and K = Boltzman's constant.

By eliminating K between equations 1.1 and 1.3 we get

$$2.303 \, \log\left(\frac{x^2}{t}\right) = 2.303 \, \log K_o - \left(\frac{Q}{K} \cdot \frac{1}{T}\right) \tag{1.4}$$

A plot of log (x^2/t) against $1/T$ yields a straight line with slope -Q/K and is called an Arrhenius plot. The activation energy Q represents the energy barrier of the limiting step in the formation process.

It was found that the presence of impurities like oxygen generally reduce the growth kinetics without changing the mode of reaction [Ni-83, Sc-82]. It was reported by Olowolafe [Ol-76] that in some cases such as Ni_2Si, growth rates depends on the crystalline orientation of the substrate. Growth rates for the various Ni-silicide phases has been summarized in table 1.3 .

1.7.2 Diffusing Species

Much work has been done on nickel silicide formation regarding the diffusing species involved [Pr-81, Bo-82, Tu-75, Tu-77, Ba-82], Si* tracer experiments on Ni_2Si growth by Pretorius [Pr-81] and Pretorius and Botha [Bo-82] in which radioactive Silicon (Si*) has been deposited on the silicon substrate followed by deposition of Ni, showed a shift of Si* tracer layer to the film surface, in addition to considerable spreading of the Si* profile. The peak shift indicates that the film growth is dominated by nickel diffusion of any kind and/or substitutional silicon motion. Results of Xenon marker experiments in Ni_2Si [Tu-75, Tu-77], in which Xenon was implanted in silicon prior to deposition of nickel, showed that the marker layer also moved towards the silicide

17

surface. From their data however, Tu et al. estimated that 95% of the silicide formation resulted from the diffusion of nickel atoms. Ni* tracer experiments by Baglin et al. [Ba-82], in which a thin layer of activated nickel on the silicon wafer was coated with non-radioactive nickel approximately 1600Å thick, also shows that the tracer tends to move to the surface but a considerable broadening of the original Ni* distribution is observed, indicating extensive self-diffusion of Ni* in the Ni$_2$Si lattice. All these experiments are consistent with the fact that Ni$_2$Si growth is due mainly to diffusion of Ni in Ni$_2$Si.

Table 1.3 : *Kinetics of nickel silicide formation by thermal heating.*

Silicide	Time dependence (t=time)	Rate of formation K(T)*	Temperature T (°C)	Substrate Si	Activation energy Q (eV)	Temperature range (°C)	Analytical technique used	References
Ni$_2$Si	t½	2.5x10^{-18}	275	<100>	1.5±0.1	200-325	RBS	[Tu-75]
	t½	2.6x10^{-18}	275	<111>	1.6±0.2	225-325	RBS	[Ol-76]
	t½	2.4x10^{-18}	275	<100>	1.5±0.2	225-325	RBS	[Ol-76]
	t½	2.3x10^{-18}	275	(poly)	1.3±0.2	225-325	RBS	[Ol-76,Na-76]
	t½	0.8x10^{-18}	275	<100>,<111>	1.3±0.1	297-430	RBS	[Co-76]
	t½	7.8x10^{-18}	292	<100>	-	-	RBS	[Sc-81(a)]
	t½	1.2x10^{-18}	275	H:Si(a)	1.4	250-325	RBS	[Hu-85(a)]
NiSi	t	2.5x10^{-18}	275	<100>,<111>	1.4±0.1	297-430	RBS	Co-76]
	t½	1.8x10^{-18}	292	<100>	-	-	RBS	[Sc-81(a)]
	t½	9.5x10^{-18}	325	<100>	-	-	RBS	[Sc-81]
	t½	2.6x10^{-18}	325	<100>	1.7	273-350	RBS	[d'H-84]
	t½	0.4x10^{-18}	325	<111>	1.7	325-400	RBS	[d'H-84]
	t½	4.3x10^{-18}	325	<100>	1.2±0.22	300-360	RBS	[Ma-84]
	t½	1.0x10^{-18}	325	<111>	1.8±0.17	320-370	RBS	[Ma-84]
NiSi$_2$	t½	7.0x10^{-18}	400	(a)	1.7	350-425	RBS	[Li-84(a)]

This table lists experimental results on the kinetics of silicide formation. The second column states how the thickness X of a silicide film grows with time t upon thermal annealing. The third column gives the rate K(T) at the specified temperature (X^2=K(T)t for a t½ time dependence, and X=K(T)t for a linear time dependence). The fifth column specifies the nature of the Si substrate. The eight column gives the analytical methods used in studying the kinetics.

In a radioactive Si* tracer experiment by Botha et al. [Bo-80] in which Si* was deposited on the Si substrate followed by the deposition of Ni, the Si* is reported to have moved to the surface of NiSi with little spreading of Si* in the silicide after a 440°C anneal. This would be expected if Ni is the only significant moving species in the growth of both Ni$_2$Si and NiSi. Finstad [Fi-81], using a xenon marker implanted

18

in Ni_2Si has also shown that diffusion of nickel dominates the growth of NiSi from Ni_2Si at 450°C. Extensive work by Baglin et al [Ba-82] also indicates that at 450°C NiSi forms mainly by the substitutional diffusion of nickel in NiSi accompanied by self-diffusion of nickel in Ni_2Si. The results of the Si^* and Ni^* tracer experiments [Bo-80, Ba-82] together with that of the Xenon marker experiment are therefore consistent with the fact that Ni is the main moving species during NiSi formation.

It was established by d'Heurle et al [d'H-82] that the main moving species during the formation of $NiSi_2$ is nickel. This was a very unexpected result since one would anticipate that in compounds with a gross imbalance in the proportion of the two constituents, the atoms constituting the majority should move most readily (e.g., as Si in $NiSi_2$ or Co in Co_2Si). This is so since these atoms are next nearest neighbours to one another, so that a defect (e.g. a vacancy) can propagate along the network constituted by the majority atoms with only minor modifications of the lattice configuration. This argument is consistent with isostructural $CoSi_2$ where Si has been reported to be the main moving species. Ni^* tracer experiments by Baglin et al [Ba-82] also confirms that Ni is the main moving species during $NiSi_2$ formation. A possible explanation for the high diffusivity of nickel might be the presence of vacancies on the nickel lattice sites [d'H-82].

Table 1.1 gives a summary of results from marker or tracer experiments in which nickel was shown to be the dominant diffusing species during nickel silicide formation. This means that the growth of Ni_2Si is determined by the transport of mainly Ni atoms through the silicide and that the onset of the second phase NiSi is induced by a supply limitation when the Ni film is consumed. The reaction for the formation of the first two phases in the Ni-Si (thin film Ni on bulk Si) case is

$$2Ni + Si \longrightarrow Ni_2Si$$
$$\text{and} \quad Ni + Si \longrightarrow NiSi \qquad \text{respectively.}$$

When considering silicide formation, the effect of impurities, even under the most favourable conditions of evaporation and thermal heating, cannot be ruled out. The

preliminary sample cleaning procedures are also liable to leave traces of surface contamination on the single crystal Si substrates [Kn-85, vA-80]. Much work has been done on the effects of impurities on the rate of silicide formation by forming a diffusion barrier e.g. [Sc-81(a), Li-84(b),Cr-80, Ho-84, Wi-81]. It was shown by Wielunski et al and Scott et al [Wi-81, Sc-81(a)] that impurities could form a diffusion barrier that limit the supply of nickel to the growth front to such an extent that the growth of NiSi might be prompted instead of Ni_2Si.

The information quoted in table 1.1 is therefore valid for the general case in which impurity levels in the various metal-silicon systems has been reduced to insignificant quantities by careful experimental planning and precise execution thereof.

1.7.3 Diffusion Mechanism

Owing to the increasing application of metal silicide films in the technology of contacts and interconnections in semiconductor structures, it has become very important to understand the fundamental mechanisms by which silicide films can be formed. In order to grow stable films of a chosen silicide phase reproducibly, one needs to characterize the diffusion path (grain boundary, substitutional motion etc.) for both the metal and the silicon atoms as they pass through the growing layer. One should also know which of the diffusion processes provides the principal supply of atoms for silicide growth. A considerable amount of work by way of implanted inert markers in the Ni-Si system has been reported already [Tu-78, Tu-75, Ba-80, Tu-77, Fi-81]. Explicit information about diffusion mechanisms can also be obtained by using radioactive-tagged tracers of the metal and/or silicon [Pr-81,Bo-82,Ba-82].

Taking all inert marker and radioactive tracer experimental results into account, Baglin et al [Ba-82] concluded that the Ni_2Si growth is due mainly to a combination of lattice and grain boundary diffusion of Ni in Ni_2Si in roughly equal proportions. When the nickel is exhausted, NiSi forms mainly by substitutional diffusion of nickel in NiSi accompanied by self-diffusion of nickel in Ni_2Si [Ba-82]. In a xenon marker experiment, in which the marker was implanted into a thin film of NiSi initially formed

20

on its silicon substrate by the reaction of this substrate with a thin nickel film, d'Heurle et al [d'H-82] observed that the xenon marker moved to occupy a thin layer near the surface during $NiSi_2$ growth at 825°C. This not just indicates that Si is not the main diffusing species, but also suggests that $NiSi_2$ forms from NiSi mainly by the substitutional diffusion of Ni. Apparently vacancy diffusion of nickel occurs readily in $NiSi_2$ because its cubic (CaF_2 - type) lattice embodies an open cubic sublattice of nickel atoms within which substitutional diffusion takes place easily.

The above mechanisms were found for silicide growth on both (100) and (111) orientated single crystal silicon substrates. Secondary effects such as orientation and grain size will influence the relative contributions from the various diffusion paths.

1.7.4 The Ni-Si Phase Diagram

The phase of the silicide which forms when certain metals in contact with silicon are heated, depends on the temperature of formation. The phase diagram is a convenient graphical summary of the melting characteristics of a compound. The diagram is obtained from a plot of temperature versus composition between two or more elements or compounds. Many phase diagrams of metal-silicon couples in silicide forming systems have been reported in literature [Ha-58, Mo-78]. The Ni-Si phase diagram [Ba-74] is given in figure 1.4. From this diagram one observes well defined phases and eutectic melting points. The lowest temperature at which a liquid appears in the Ni-Si system is at 966°C, the temperature at which $NiSi_2$ decomposes by a peritectic reaction. In silicon device processing, silicide formation occurs via a solid state reaction well below the melting point of the reacting components and the silicide products. In this project the reaction occurs between the silicon substrate which is a covalently bonded single crystal and the thin nickel film which is fine grained with metallic bonding. The Ni-Si system consists of six compound phases of nickel silicide (see figure 1.4). Not all the equilibrium phases are present as dominant growth phases during silicide formation in thin films systems. They may nucleate, but do not grow to detectable macroscopic dimensions. A general behaviour in silicide formation is that phases grow consecutively provided that no impurities exist in the layers to retard the

21
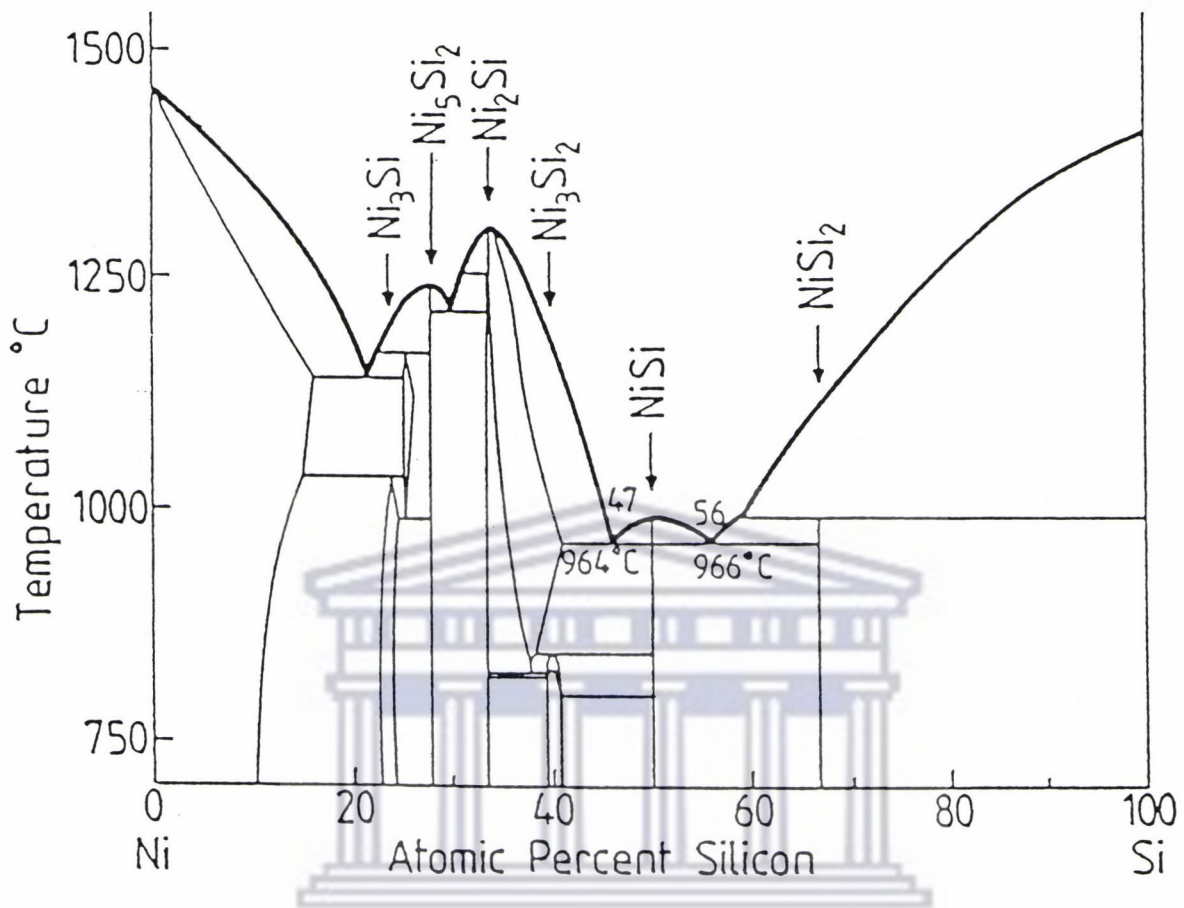
Figure 1.4 : *Phase diagram of the Ni-Si system, showing six phases of nickel silicide, varying from the metal rich phase (Ni₃Si) to the silicon rich phase (NiSi₂).*

growth kinetics.

According to the Walser and Bené [Wa-76] and Effective Heat of Formation (EHF) models [Pr-84], Ni_2Si is the first phase to nucleate in the case of thin nickel layers on bulk silicon. The extended Walser and Bené rule [Ts-81] and the EHF model furthermore predict the second and third phase to be NiSi and $NiSi_2$ respectively. This is in accordance with experimental results. The metal-rich Ni_2Si forms at approximately 200°C and upon further heat treatment the monosilicide NiSi, forms at about 350°C, while the disilicide $NiSi_2$, forms at 750°C. For samples with a thickness

22

of the Ni layer much larger than that of the Si, the phase sequence would be Ni_2Si, Ni_5Si_2 and Ni_3Si as predicted by the Pretorius [Pr-84] and the extended Walser and Bené [Ts-81] rules.

1.7.5 Crystallographic Properties

Silicon has the same outer electronic structure as carbon, and has the same crystal structure as one of the forms of carbon (diamond). However since it is more electropositive than carbon it forms compounds with many metals which have typical alloy structures (as in the case of silicides).

The crystallographic data of Ni-silicides [d'H-84, Pa-48,To-51] are given in table 1.4. Various structure has been reported for NiSi [Bo-33, Os-39, Pa-48, To-51]. The structure of nickel silicide (NiSi) was first studied by the powder method by Barén [Bo-33] who described this compound as cubic (a = 0.4437nm) of the FeSi type (see figure 1.5(c)). The unit cell of the NiSi phase contains 8 atoms. The structure of FeSi is regarded as distorted face - centred cubic, in which the presence of the silicon atoms has forced the nickel atoms out of their original positions, each by an equal amount. These translations are all in <111> directions i.e., parallel to body diagonals of the cube. Later work, also by the powder method, was undertaken by Oswana and Okamoto [Os-39]. These authors, on the basis of thermic, dilatometric and metallographic investigations, revised the Ni-Si system and tried to measure the dimensions of the unit cells of individual phases. NiSi was found to be tetragonal (a = 7.655Å, c = 8.45Å) with twenty molecules in the unit cell. However, Pauling and Soldate [Pa-48] determined the structure of NiSi to be once again of the Cubic FeSi type. From later work by Toman [To-51] the structure of NiSi has been determined to be that of a MnP structure which has a deformed NiAs arrangement (see figure 1.5(a)). The unit cell of NiAs (hexagonal) is composed of three superimposed hexagonal networks of Ni-atoms. Inside this cell one finds two As atoms diagonally disposed in the centre of two trigonal prisms such as ABDA'B'D'. In NiSi, the Ni atoms are slightly displaced horizontally as shown by the small arrows, the resulting increase in the distance between some of these Ni atoms (A,B,D) and decrease between

23

some of the others (A',B',D) causes a slight vertical displacement of the internal atoms (P in MnP, Si in NiSi) leading to a change from a hexagonal to an orthohombic structure.

**Table 1.4 :** *Crystallographic data of nickel silicides.*

SILICIDE	CRYSTAL SYSTEM	NAME OF STRUCTURE	STRUCTURE-BERICHTE CLASSIFI-CATION	LATTICE CONSTANTS OF UNIT CELL (Å)		
				A	B	C
Ni_2Si	Orthor* Hexag**	$PbCl_2$ -	C23 -	4.99 3.805	7.03	3.72 4.890
Ni_3Si_2	Orthor	-	-	10.805	12.229	6.924
NiSi	Orthor* Cubuc**	MnP FeSi	B31(12) B28	5.18 4.446	5.62	3.34
$NiSi_2$	Cubic Rhomb	CaF_2	C1	5.395 8.881	$\propto = 90°23'$	

* LOW TEMPERATURE

** HIGH TEMPERATURE

The structure of the Ni_2Si phase is closely related to the NiAs structure. Ni_2Si possesses a structure which is a distortion of Ni_2In; this latter has the structure of the nonexistent "$Ni_2 As$" which would be obtained by inserting the extra Ni atoms in the centre of the unoccupied (in NiAs) trigonal prisms such as B CDB'C'D' (see figure 1.5(b)). Small structural changes lead from NiAs to MnP (NiSi) on the one hand, to Ni_2In (Ni_2Si) on the other. We therefore observed Ni atoms with two different environments in the Ni_2In-structured Ni_2Si, namely corner atoms and internal atoms. However, only one type of silicon atom is observed. It must be noted that the respective environments of the Si and Ni atoms in NiSi are also totally different. This crystal arrangement has everything to do with the type of diffusion mechanism and the identity of the diffusing species during Ni_2Si and NiSi formation.

$NiSi_2$ adopts a CaF_2 structure (see figure 1.5(d)). In CaF_2 each Ca^{2+} ion is surrounded

24
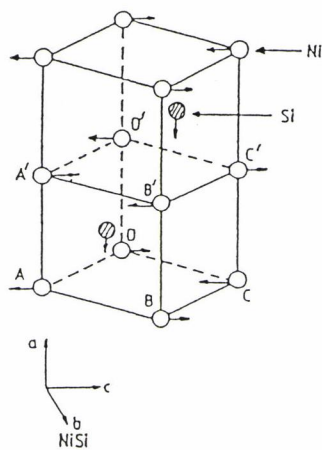
(a) The orthor. MnP (distorted NiAs) structure of NiSi
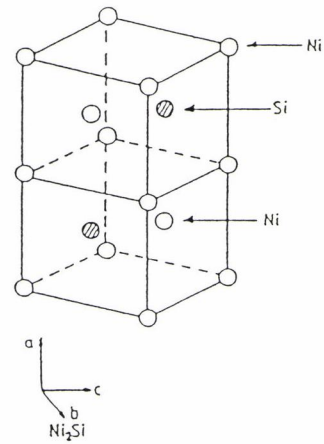
(b) The orthorhombic PbCl$_2$ (distorted Ni$_2$In) structure of Ni$_2$Si
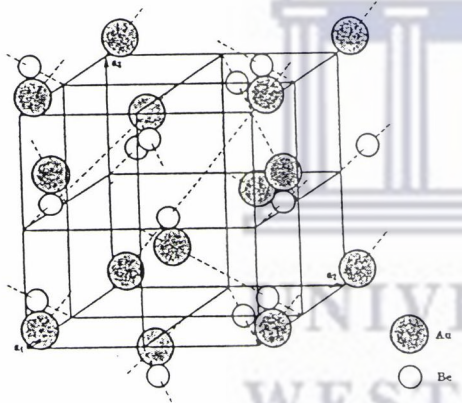
(c) The cubic FeSi structure of NiSi
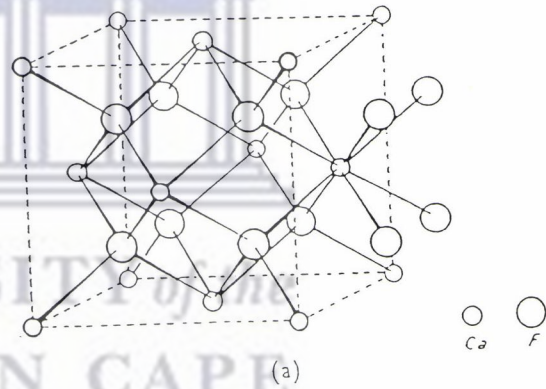
(d) The cubic CaF$_2$ structure of NiSi$_2$

Figure 1.5 : *Crystal structures of various nickel-silicide phases.*

by eight F$^-$ ions at the corners of a cube, and each F ion by four Ca^{2+} ions at the corners of a regular tetrahedron [We-62]. Thus NiSi$_2$ is composed of eight body-centre cubes adjacent to one another with all the corner sites occupied by silicon atoms. Only four of the possible eight body-centre positions are occupied

25

by nickel atoms. Under normal conditions the CaF_2 type structure is perfectly ordered and stable due to its ionic nature. However at high temperatures (above the peritectic temperature of 993°C for $NiSi_2$) it is possible that the body - centred lattice becomes disordered, providing an effective vacancy concentration of 50% which would account for the high diffusivity of nickel [d'H-82]. In addition to the cubic structure with lattice parameter a = 0.5395nm proposed for $NiSi_2$ [Do-73], a rhombohedral structure with lattice parameter a = 0.8881nm has also been reported [Sa-80].

It is therefore possible for a specific phase to adopt one of two or more different structures. Many factors, like temperature and the structual state of the previous phase, can play a role in deciding the crystal structure of the final phase.

1.8   SCOPE OF THIS INVESTIGATION

Transition - metal silicide are currently being used as essential elements in microelectronic technology. A great number of studies have been devoted to such thin film reactions in which the structure and properties of the phase formed as well as the kinetics of reactions has been covered. Interfacial properties has also become important for device reliability and efficiency for the sake of reproducibility of silicide growth, one also needs to know how different phases grow with respect to one another. This investigation was launched to investigate the growth mechanisms of different nickel silicide phase at various transition temperatures with special emphasis placed on the transition from polycrystalline NiSi to single crystal $NiSi_2$.

In chapter 2 the experimental techniques that include ultra high vacuum deposition, vacuum annealing, cross-sectional TEM specimen preparation and the various sample characterization techniques as well as the theory of the analysis techniques used in this investigation are discussed. These techniques include Rutherford backscattering Sepctrometry (RBS), Transmission Electron Microscopy (TEM) and Electron Diffraction (SAD), Scanning Electron Microscopy (SEM), Auger Emission

26

Spectroscopy (AES) and X-ray Diffraction (XRD).

In chapter 3 the experimental results are given and discussed in general. Cross-sectional Transmission Electron Microscopy was used to study the morphology of metal-silicide and silicide - silicon interfaces. Rutherford Backscattering Spectrometry and X-ray Diffraction was used to identify the various silicide phases.

Chapter 4 deals primarily with the results and discussion pertaining to $NiSi_2$ formation. Scanning Electron Microscopy shows interesting surface morphology of samples in which island-like $NiSi_2$ growth takes place in an NiSi matrix. Grain boundaries in the initial and final stages of $NiSi_2$ formation are characterized by 'holes' or 'vacancies' which extend from the surface to the silicon substrate. Cross-sectional examination in the Transmission Electron Microscope also reflects interesting phenomena during $NiSi_2$ formation. A model to account for these observations has been proposed in an effort to understand the growth kinetics and morphology involved.

In chapter 5 a summary and the conclusions are given.

UNIVERSITY *of the* WESTERN CAPE

27
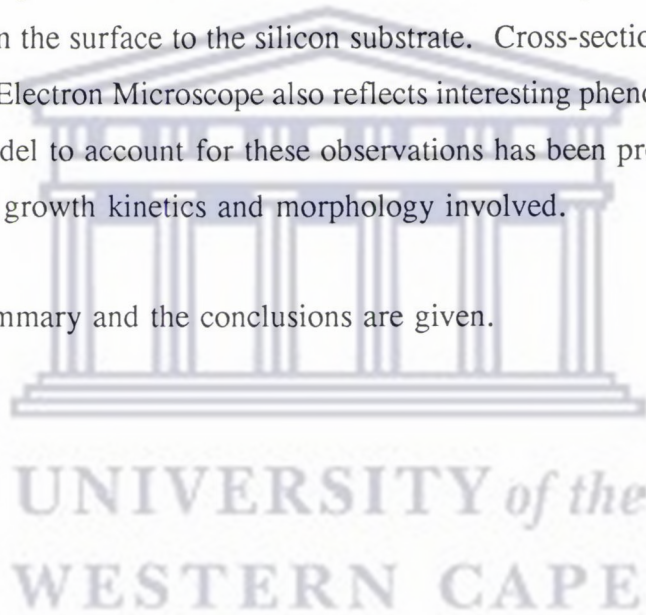
CHAPTER 2

EXPERIMENTAL PROCEDURE

2.1 SAMPLE PREPARATION

2.1.1 Substrate Preparation

Silicon wafers of 75mm diameter and a thickness of 380μm were scribed and cleaved to give $1cm^2$ substrates. The silicon, which were (100) oriented, were boron doped and had a resistivity of about 1Ωcm. The $1cm^2$ silicon chips were degreased and washed in sequence with methanol, acetone, tricholoroethylene, acetone and methanol, in an ultrasonic bath. After thorough rinsing and washing in deionized water with resistivity greater than $15M\Omega$cm, the substrates were etched for 5 minutes in a 20% HF solution to remove the native oxide layer. The samples which were properly degreased and cleaned came out dry when removed from the etchant. They were then mounted onto circular aluminium sample holders which could accommodate ten samples each. A total of six sample holders could be loaded into the evaporation chamber at a time, thereby giving the experimentalist the option to prepare six different structures. The chamber was evacuated as soon as possible to prevent the regrowth of the native oxide.

2.1.2 Vacuum evaporation

Evaporation of nickel onto the silicon substrates took place in a vacuum of the order of 10^{-7} mbar. To achieve this pressure a rotary pump was initially used for roughing to approximately $5x10^{-2}$ mbar. Two sorption pumps, containing an activated sorbet zeolite (which acted as a molecular sieve that absorb and trap gaseous molecules) and cooled with liquid nitrogen was then used until a pressure of about $1x10^{-4}$ mbar is reached. Ion pumps that cause ionization of gas molecules (by maintaining a voltage of about 6 000 V between the anode and cathode) with gathering of the molecules at the electrodes, further reduced background pressure to better than 10^{-6} mbar.

28

The vacuum was further improved to about 10^{-7} mbar by sublimation pumping which was carried out by the evaporation of titanium onto a liquid nitrogen cooled cryopanel where gettering and condensation occurred. Vacuum was maintained between 1 and 5×10^{-7} mbar during evaporations. Pressure was monitored with a thermocouple down to 10^{-2} mbar and at high vacuum with a penning gauge down to 10^{-7} mbar.

Deposition of Ni was carried out on Si substrates at ambient temperatures using an electron beam source. The electron gun, which consists of a tungsten filament, produces electrons that are focused on the hearth by a magnetic field. There are three separate hearths allowing the user to evaporate three different materials in sequence without breaking vacuum. These hearths, which are watercoaled, were thoroughly cleaned with fine emery paper before fresh materials were loaded to prevent contamination from previous evaporations. Depositions were to a large extent contamination free and no impurities in the deposited layers could be observed within the detection limits of Rutherford backscattering. Deposited thicknesses and the rate of evaporation was monitored with a vibrating quartz crystal, the frequency of which is a function of the accumulated mass of material.

2.1.3 Vacuum annealing

The thin film samples were annealed in a vacuum tube furnace. The system contained a carousel with eight boats each of which can accommodate five samples. The furnace was pre-set to the required temperature, and one boat at a time was slid into the furnace through the quartz tube for the required annealing time. The furnace is equipped with a programmable Eurotherm Type 815 unit which controlls the temperature. This unit is connected to a built-in thermocouple which is situated in the vicinity of the boat to be heated. With the built-in microprocessor, any fluctuation in temperature can immediately be detected and the necessary power to the heaters adjusted, so that a reasonably constant temperature could be maintained during the annealing process. The furnace was evacuated to a vacuum better than 10^{-5} mbar with a turbomolecular pump assisted by a liquid nitrogen cryopanel, and a penning gauge was used to monitor the pressure. Different annealing times at various temperatures ranging from room temperature to 1200°C is possible.

2.2   SAMPLE CHARACTERIZATION

2.2.1   Rutherford Backscattering Spectrometry (RBS)

Rutherford backscattering spectrometry (RBS) is a non destructive, fast, direct and precise method for obtaining elemental depth profiles in solids [Ch-78,Zi-75] and is as such an ideal technique for studying thin film systems.

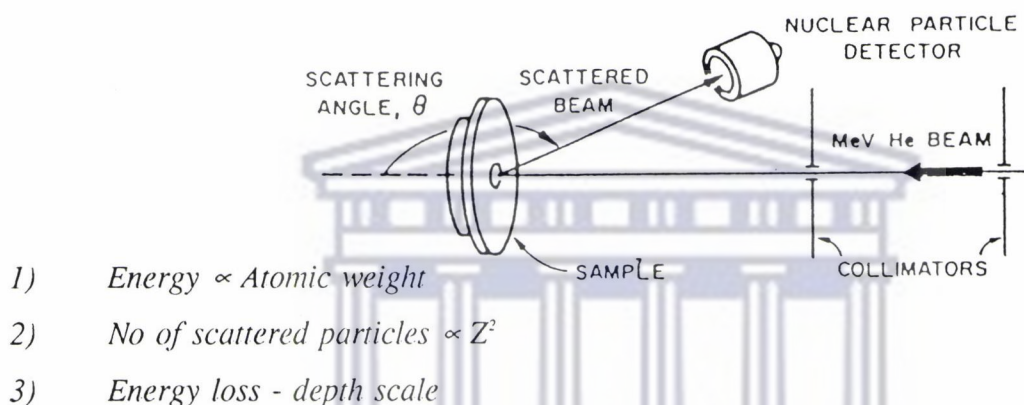Schematically the RBS technique can be explained according to figure 2.1 .

1)   *Energy ∝ Atomic weight*

2)   *No of scattered particles ∝ Z^2*

3)   *Energy loss - depth scale*

Figure 2.1 : *Schematic of the experimental set-up for Rutherford Backscattering Spectrometry. A collimated beam of He ions is incident on a planar sample. Particles scattered to an angle θ are detected by a solid state nuclear particle detector. All this apparatus must be under vacuum.*

In figure 2.1 a homogeneous, monoenergetic light ion beam is directed onto the sample, mounted in a chamber evacuated to a vacuum better than 10^{-4} mbar. The backscattered particles are detected with a solid state detector and analyzed for backscattered energies. The energy of the backscattered particles is directly proportional to the atomic weight of the atom from which it is scattered, while the number of scattered particles is directly proportional to the square of the atomic number, Z. The backscattered particle also loses energy on its inward and outward paths in the sample, thereby providing for depth analysis. There are therefore three basic concepts in backscattering spectrometry, each having an analytical capability:

30

1)   The kinematic factor which provides mass analysis,

2)   The differential scattering cross section which provide quantitative analysis, and

3)   The energy loss of a charged nuclear particle provides a method for depth analysis.

2.2.1.1   The backscattering kinematic factor

When a projectile of mass m, with energy E_o and velocity v_o collides with a stationary target atom with mass M, momentum is transferred from the projectile to the target atom. After the collision the target atom has an energy E_2 and velocity v_2, while the projectile is scattered with energy E_1 and velocity v_1 (see figure 2.2).
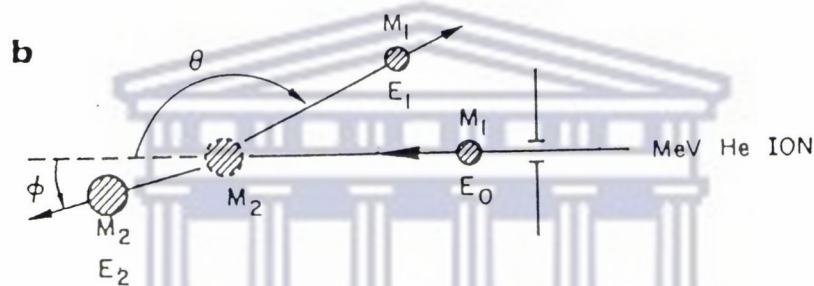

Figure 2.2 : *Schematic representation of an elastic collision between a projectile of mass m, velocity v_o, and energy E_0 and a target mass M which is initially at rest. After the collision, the projectile and the target mass have velocities and energies v_1, E_1 and v_2, E_2, respectively. The angles θ and φ are positive as shown. All quantities refer to a laboratory frame of reference.*

The energies of the scattered projectile and recoil particle can be calculated from energy and momentum conservation laws. The kinematic factor k is defined as the ratio of the projectile energies after and before collision and is given by [We78]

$$K = \frac{E_1}{E_0} = \left[\frac{m cos\theta + \sqrt{M^2 - m^2 sin^2\theta}}{m+M} \right]^2 \tag{2.1}$$

From equation 2.1 it isclear that the kinematic factor, k, depends on the scattering angle Θ in the laboratory system and the masses involved in the collision process, $K = k(M,m,Θ)$. Thus if the projectile mass, scattering angle Θ, together with the ratio E_1/E_0 is known, the target mass M can be determined.

31

2.2.1.2 Differential scattering cross section

The differential cross section is a measure of the probability for elastic scattering by coulomb interaction and is given by [We-78]

$$\frac{d\sigma}{d\Omega} = \left(\frac{zZe^2}{4E_o}\right)^2 \frac{4}{\sin^4\theta} \frac{[\cos\theta + \sqrt{1-(\frac{m}{M}\sin\theta)^2}]^2}{\sqrt{1-(\frac{m}{M}\sin\theta)^2}} \tag{2.2}$$

Where

z = atomic no. of incident ion

Z = atomic no. of target atom

θ = laboratory scattering angle

e = unit charge

Ω = finite solid angle spanned by detector

The differential scattering cross section connects the backscattering yield to quantitative analysis. It can also be seen from equation (2.2) that the sensitivity of RBS is greatest for heavy target atoms and small scattering angles.

2.2.1.3 Energy loss

When a projectile penetrates a target, it loses its energy throughout its trajectory to the electrons of the target atoms by ionization and excitation as well as by nuclear collisions. When this projectile encounters a target atom in a direct head-on elastic collision it change its trajectory into an outward direction. During its outward path it again loses energy to the target atoms until it emerges from the target. By measuring this energy loss, the depth to which the particle has penetrated can be determined. In figure 2.3 the backscattering analysis of an elemental target of atomic mass M and atomic density N is considered. The incident energy of the projectiles is E_o and the scattered particles have energy KE_o when scattered from the surface. When a particle is scattered at a depth x and emerges from the target into the

32

detector it will have lower energy because of the energy loss of the projectile in the target. The incident and scattered angles are Θ^1 and Θ_2 with respect to the normal of the target, thus
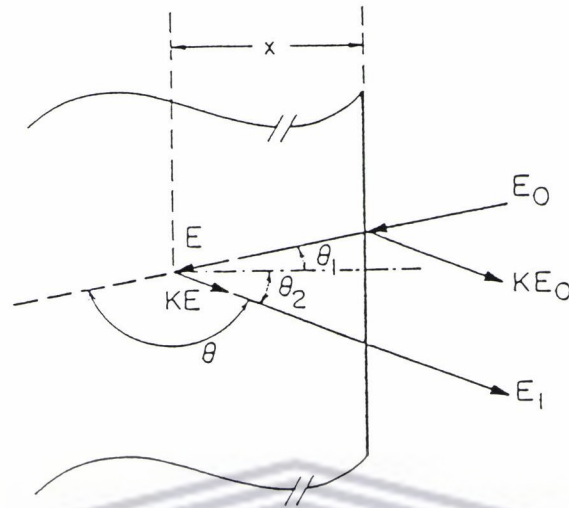

Figure 2.3 : *The definition of all the parameters necessary to describe a backscattering event at a depth in a sample. The incident beam, detector and sample normal are coplanar [Ch-78]*

the scattering angle is Θ - 180°-Θ^1 -Θ_2. The energy of the projectile at the depth x just before scattering is E and can be related to E_o by:

$$E = E_o - \int_o^{\frac{x}{\cos\theta_1}} (\frac{dE}{dx}) \, dx \qquad (2.3)$$

and since energy is also lost on its outward path, we have that the energy of the ion emerging from the sample is

$$E_1 = kE - \int_o^{\frac{x}{\cos\theta_2}} (\frac{dE}{dx}) \, dx \qquad (2.4)$$

The energy difference ΔE between particles scattered from atoms on the surface and that scattered from atoms at a given depth x is defined from the spectrum given in figure 2.3 as

$$E = kE_o - E_1 \qquad (2.5)$$

and with equation (2.3) substituted into equation (2.4), equation (2.5) becomes

$$\Delta E = K \int^{\frac{t}{\cos\theta_1}} (\frac{dE}{dx}) \, dx + \int_o^{\frac{t}{\cos\theta_2}} (\frac{dE}{dx}) \, dx \qquad (2.6)$$

33

The first term in equation (2.6) comes from the energy loss along the incident path times the kinematic factor, while the second term comes from the energy loss along the outgoing path. The integrations in equations (2.3), (2.4) and (2.6) are line integrals and is a function of energy at the given location inside the target. For thin films $(\frac{dE}{dx})$ can be considered

constant and thus a surface approximation can be made whereby this variable can be evaluated for an energy of E_o for its incident and kE_o for its outgoing path. After integration we have

$$\Delta E = [\frac{K}{\cos\theta_1} \frac{dE}{dx}|E_o + \frac{1}{\cos\theta_2} \frac{dE}{dx}|kE_o] x \qquad (2.7)$$

$$\Delta E = [S] x \qquad (2.8)$$

where [S] is the stopping factor.

The number of counts in a channel in a backscattered spectrum represents the number of backscattered ions having energies between E and E + δE that were detected. These ions originated from a thin slice, thickness δx, at a depth x inside the sample (see equation (2.8).

If Ω is the solid angle underspanned by the detector, Q the total number of particles incident on the sample, σ the differential cross section and N the atomic density of the scatterer, the height of a spectrum can be related to the concentration of the scatterer in the target by:

$$H = \Omega\ Q\ \sigma\ N\ \delta\ x \qquad (2.9)$$

Substituting equation (1.8) into (1.9) we obtain

$$H = \Omega\ Q\ \sigma\ N\ \delta\ E/\ [S] \qquad (2.10)$$

The concentration of an impurity like Ni in silicon can be related to the height of the Ni signal by

$$H_{Ni} = \Omega\ Q\ \sigma_{Ni}\ \delta\ N_{Ni}\ SE/[S]^{Si}_{Ni} \qquad (2.11)$$

The height of the silicon signal is

34

$$H_{Si} = \Omega \; Q \; \sigma_{Si} \; \delta \; N_{Si} \; SE/[S]^{Si}_{Si} \qquad (2.12)$$

The concentration of Ni in silicon can then be determined by taking the ratio of equations (2.11) and (2.12) and solving for N_{Ni}

$$N_{Ni} = N_{Si} \; X \; \frac{H_{Ni}}{H_{Si}} \; X \; \frac{\sigma_{Si}}{\sigma_{Ni}} \; X \; \frac{(S)^{Si_{Ni}}}{(S)^{Si_{Si}}} \qquad (2.13)$$

2.2.1.4   Experimental setup for RBS

A schematic illustration of the experimental layout for Rutherford Backscattering measurement is shown in figure 2.4 .The samples were analyzed with a 2 MeV mono-energetic and collimated beam of alpha particles which were accelerated by the Van de Graaff accelerator.
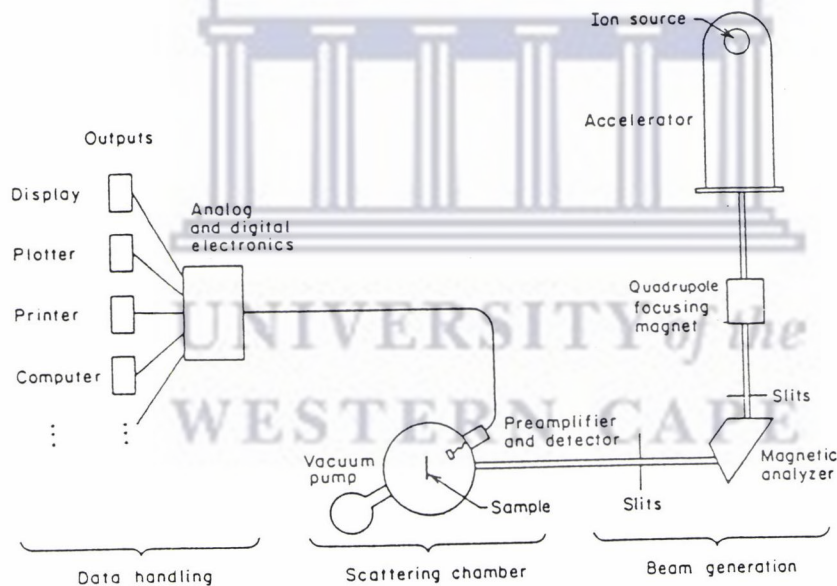
Figure 2.4 :   *A Schematic layout of the Rutherford Backscattering Spectrometry system.*

The beam was passed through a series of collimators, the last one defining the analysing beam to be incident on the sample. The diameter of the beam was reduced to 2mm before entering the scattering chamber. The backscattered particles were detected by a solid state silicon detector mounted in the plane of the beam at an angle of 165° with respect to the incident

35

beam direction. A vacuum of approximately 10^{-6} kPa was achieved and maintained in the backscattering chamber by using a fore pump and a turbo molecular pump. Up to ten samples were mounted on a holder and analyzed without breaking vacuum. The samples were subsequently shifted by remote control to be in the beam path in the vacuum chamber. The sample holder was kept at an angle of 10° with respect to the incident beam to minimize channelling effects. A permanent horse shoe magnet prevented secondary electrons from escaping from the sample for efficient current integration.

The backscattered particles which were detected by the solid state detector generates an electronic signal which was amplified and processed with analogue and digital electronics. They were then sorted according to pulse height (energy) and stored in a multichannel analyzer with a calibration factor determined at the start of the analysis. Si, Pt and Co standards were used for calibrations and an energy calibration of 4 keV per channel was maintained throughout an analysing run. The spectra were saved on a magnetic tape and then transferred to either a VAX computer or PC. A Rutherford backscattering simulation program, RUMP [Do-85] was used to further assist in the analysis of the spectra.

In addition to the above experimental setup, channelling could also be carried out. Crystal alignment was obtained with a goniometer which could vary the sample orientation in three dimensions. Up to 360° rotation in the vertical plane, up to 180° rotation in the horizontal plane and a maximum tilt of 30° either side of the vertical were possible. Before samples were changed all the axes were reset to zero to check for stepping motor malfunctioning. The goniometer was manipulated by remote electronic control and increments as small as 0.01° along any axis was possible. The aligned spectrum was normally compared with a spectrum obtained along a random crystal direction which was acquired by setting the y-axis to 2° and continuously rotating the z-axis.

2.2.2 TRANSMISSION ELECTRON MICROSCOPY

The electron microscope utilizes an electron beam which is focused by an assembly of electromagnetic lenses, with the beam only enclosed in an evacuated column. It is an

36

improvement on the light microscope especially as far as resolution is concerned since electrons have much shorter wavelengths (in the range of 10ths of pm depending on the accelerating voltage between the cathode and anode in the electron gun) than light which is of the order five times longer [d'B-24,Da-27]. Two electron microscopes, namely the Transmission Electron Microscope (TEM) and the Scanning Electron Microscope (SEM) will be discussed in this section and section 2.2.3 respectively.

The transmission electron microscope (TEM) basically consists of an electron gun which provides the illumination, a series of electromagnetic lenses, a viewing screen coated with a layer of electron-fluorescent material, and a camera which must work in the vacuum within the microscope. These components are assembled into a vertical 'microscope column' of which a typical example is shown in figure 2.5 .

The electron gun emits a diverging beam of electrons through the anode aperture. This beam can be deflected to be aligned parallel to the optical axis of the lens system. The deflector coils are controlled by the gun alignment controls, and the electron beam is focused down to a fairly small spot by the first condenser lens. The setting of this lens controls the ultimate spot size attainable by the condenser system which is generally less than 1 μm. The second condenser lens projects the beam at the specimen in such a way that the area illuminated and the convergence angle can be controlled. Below this lens is a moveable aperture which selects the primary beam and cut out any scattered beams, thus giving a clear diffraction image. The best resolution and image sharpness is obtained by working with the smallest condenser lens aperture ($\leq$300 μm) while exiciting the second condenser lens more strongly. However, this reduces the illumination level considerably.

The condenser stigmator, placed below the condenser aperture, compensates for astigmatism in the illumination system. In this same region are the 'wobbler' coils for aiding focusing and two sets of alignment coils in order to bring the beam exactly onto the optical axis in the crucial part of the microscope near the specimen. The specimen, objective aperture and objective stigmator coils are all placed inside the objective lens windings. The objective lens focuses on the specimen and forms an intermediate image at a magnification of about 50X. The objective aperture sits in the 'back focal plane' of the objective lens and enables the

37

operator to allow particular groups of electrons to contribute to the final image (see figure 2.7). In the plane of the first intermediate image is the 'selected area' aperture which allows
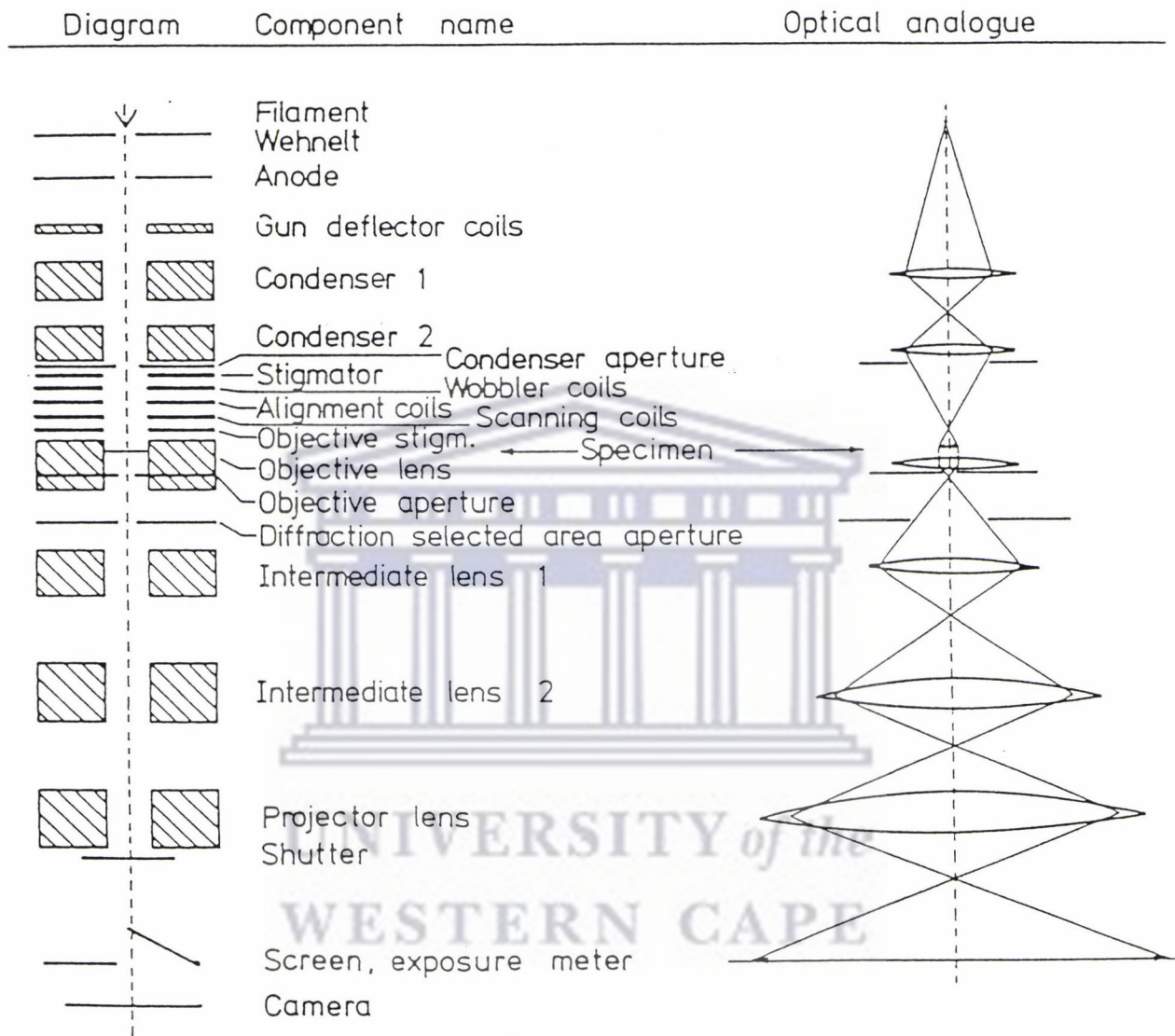
Diagram	Component name	Optical analogue
	Filament	
	Wehnelt	
	Anode	
	Gun deflector coils	
	Condenser 1	
	Condenser 2	
	—Stigmator ——Condenser aperture	
	—Alignment coils ——Wobbler coils	
	—Objective stigm. —Scanning coils	
	—Objective lens ——Specimen——	
	—Objective aperture	
	—Diffraction selected area aperture	
	Intermediate lens 1	
	Intermediate lens 2	
	Projector lens	
	Shutter	
	Screen, exposure meter	
	Camera	

Figure 2.5 : *A cross-section of the basic components of the TEM. The optical analogue is also provided.*

a particular part of the image to be selected for examination and diffraction analysis. Below this aperture are three or four lenses whose function is to magnify the image or diffraction

38

pattern (see section 2.2.2.2) and project it onto the fluorescent screen.

The electronics needed to control the electron gun, six or seven lenses and a vacuum system is quite complex. For this reason there is a tendency for modern electron microscopes to be controlled by a built-in computer which results in a reduction in the number of manual controls.

2.2.2.1   Electron beam-specimen interaction

When an electron beam is incident on a thin specimen, each electron passing through the specimen has a number of possible fates.

(1) The incident electron can pass straight through the specimen without interacting with it in any way.

(2) When electrons encounter, or pass very close to, an atomic nucleus of one of the atoms in the specimen, they can be deflected through relatively large angles without loss of energy, leading to elastic scattering. Since this results from a mass difference between nucleus and electron, the number of electrons so deflected will increase with specimen thickness and is proportional to the atomic number of the element. Upon inserting a physical stop of small angular aperture below the specimen, scattered electrons will be removed from the beam and the image will be less intense in regions corresponding to a greater mass in the specimen (compare figure 2.6 (a) and (b)). This correspondence of intensity with mass is known as amplitude contrast.

(3) When an electron in the beam encounters one of the orbital electrons in an atom of a thin specimen, there is interaction between two bodies of equal mass and charge. Energy is transferred to one of the orbital electrons at the expense of the electrons of the beam leading to inelastic scattering. In very thin specimens (in the order of 60 nm) there will generally only be one encounter. The beam electrons suffering such an energy loss will be deflected through very small angles and nearly all of them will pass through the objective aperture. The energy loss corresponds to a change in wavelength and the scattered electrons will be out of phase with the unscattered ones, thus leading to what is known as phase contrast.

(4) The remaining possibility is the most likely one which includes both elastic and inelastic

39

scattering. Each time the incident electron is scattered inelastically, an electron of an atom in the specimen is knocked out of its orbit, and the atom is left in an excited state. There are many ways in which the atom can de-excite and the energy released by an electron filling the gap in the orbital leads to a number of secondary effects which can give information about the composition and nature of the specimen. These effects, which are not used as a rule in conventional transmission electron microscopy, include secondary electrons, X-rays, Auger electrons and cathodoluminescence.

The image which is formed in a transmission electron microscope is a contrast image that is a combination of the amplitude contrast due to elastic scattering and phase contrast due to inelastic scattering. There two types of contrast arise whatever the nature or form of the specimen. A third type of contrast exists namely diffraction contrast, which occurs when the atoms in the specimen are arranged in some regular way such as in a crystal lattice.

Contrast in a TEM image can be explained with the help of figure 2.6 which schematically illustrates the fate of each 100 electrons falling on a model specimen. Region (a) consist of 10nm of amorphous carbon, which, because of its low atomic mass, scatters electrons very weakly, deflecting only 9 of the 100 electrons by about $0.5°$ or more. Region (b) is an area of twice the thickness resulting in slightly stronger scattering, deflecting 17 electrons significantly. Region (c) is the same thickness as (b) but consists of amorphous lead which is a relatively heavy element. Here the majority of electrons are deflected but still only through a small angle. Region (d) consists of the same thickness of crystalline lead. In this region diffraction can take place and the scattered electron beam will be reinforced in certain directions but cancelled in others, resulting in most of the scattered electrons travelling in specific directions at the Bragg angle Θ_B (see section 2.2.2.2) to the unscattered beam.
The number of electrons emerging from the specimen in the unscattered and diffracted beams depends critically on the specimen orientation and thickness and may be anything from almost zero to 100 in each case.

The image in the microscope will show no contrast between regions (a), (b), (c) and (d) should all the 100 electrons be allowed to travel down the microscope column. Contrast is obtained by inserting on aperture below the specimen as shown in figure 2.6 (e) thereby
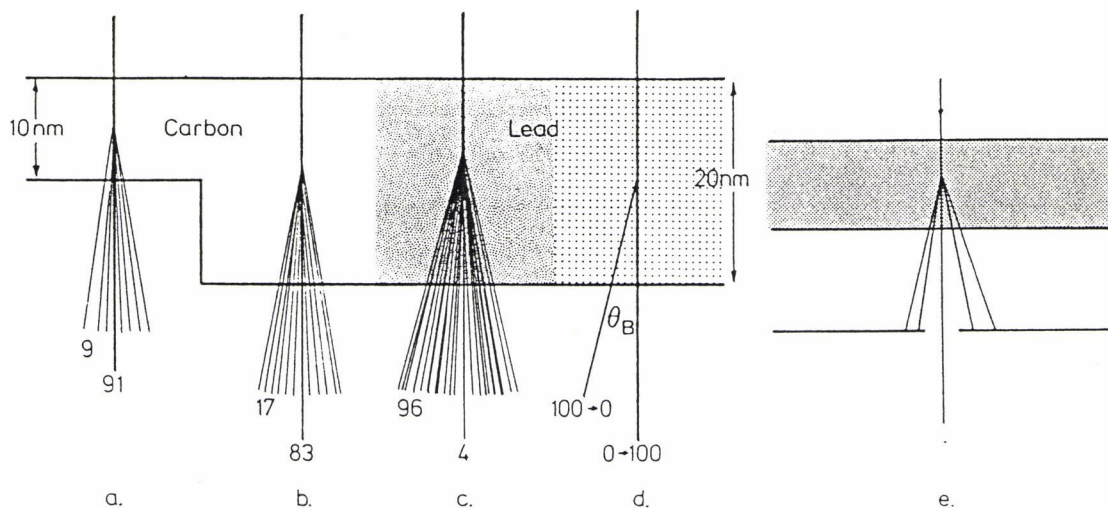
Figure 2.6 : *The fate of 100 electrons falling on four different regions of a hypothetical specimen. The numbers shown are those scattered through more than 0.5° and those unscattered. The regions are as follows: (a) 10 nm of amorphous carbon; (b) 20 nm of amorphous carbon; (c) 20 nm of amorphous lead; (d) 20 nm of crystalline lead; (e) the effect of inserting an objective aperture to stop all electrons unscattered through more than about 0.5°.*

stopping all those electrons which have been scattered through more than 0.5°. The brightness of the image of each region will then be proportional to the number of unscattered electrons which pass through the aperture, so regions (a), (b) and (c) will appear to have brightness in the ratio 91:83:4. The lead will thus be clearly visible as a dark region, whereas thickness variations in the carbon regions will only give faint contrast.

No detection device apart from a fluorescent screen is necessary for ordinary imaging.

2.2.2.2   Electron Diffraction

In all microscopes a diffraction pattern of crystalline specimens inevitably forms in the back focal plane of the objective lens (figure 2.7). In this plane all parallel 'rays' leaving the specimen in a specific direction pass through a point in the 'diffraction pattern'. Three examples of such sets of rays are shown in figure 2.7. During normal imaging the diffraction pattern is unseen because the first intermediate lens is focused on the first intermediate image

41

(bottom of figure 2.5) and this is what is finally projected onto the screen. In diffraction mode the first intermediate lens is de-excited so that it 'sees' the diffraction pattern in the back focal plane of the objective lens and projects magnified versions of this pattern instead to the projector system.
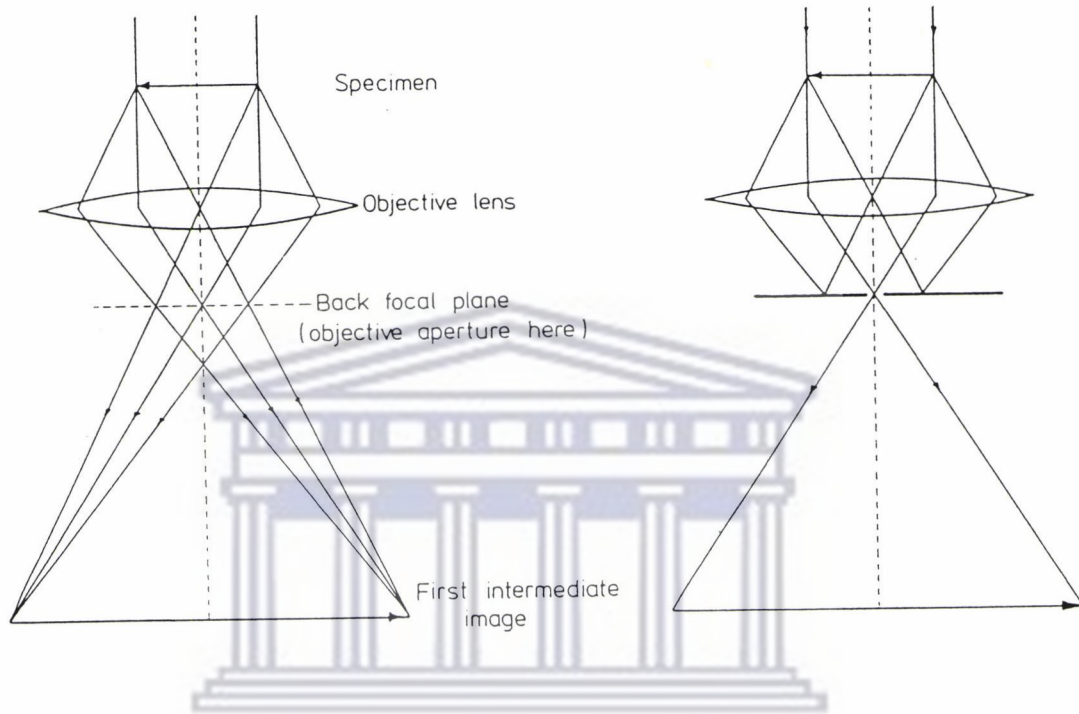

Figure 2.7 : *The objective lens. The main function of this lens is to form a magnified first intermediate image. In the back focal plane of the lens a diffraction pattern is formed. (a) All rays leaving the specimen in the same direction go through a single point in the diffraction pattern. (b) Insertion of an objective aperture in the back focal plane eliminates diffracted electrons from the image.*

There are two fundamentally different ways of examining the diffraction pattern from a selected area of the specimen. In the selected area diffraction technique an small area of the specimen is selected, although a larger area is being illuminated. In the alternative microdiffraction technique the beam is condensed into a small spot so that the diffraction pattern comes from the whole of the (small) illuminated area. In this case the diameter selected on the specimen is the same as the diameter of the beam at the specimen. This is the only way to obtain a diffraction pattern from a region smaller than $1 \mu m$ in diameter

42

(down to a few nanometres). A diffraction pattern is obtained when the electron beam encounters crystalline material, resulting in strong preferential scattering in certain well defined directions governed by the Bragg relation

$$n\lambda = 2d \sin\Theta \qquad\qquad 2.14$$

Here d is the crystal lattice spacing, Θ the angle that the incident beam makes with the particular lattice plane, λ the wavelength of the electrons and n an integer. The Bragg condition is said to be satisfied when a crystal is orientated in such a way that the incident electron-beam satisfy the diffraction angle for the specific plane. Since most of the diffracted electrons is concentrated in these Bragg directions, a crystal grain will appear bright if the diffracted beams pass through the objective aperture and dark if stopped by the objective aperture. Thus, in a polycrystalline material some grains will appear bright and some dark, depending on their orientation with respect to the electron beam (see for example figure 4.2(b)). Different types of diffraction pattern arise from different specimen microstructure as can be seen in figure 2.8 . Figure 2.8 (a) shows a single crystal specimen (i.e. a specimen consisting of a single repeating array of atoms) orientated in such a way that several sets of planes are parallel to the beam. This gives rise to a diffraction pattern consisting of a regular array of bright spots. The arrangement of these spots depends upon the orientation of the atomic planes in the electron microscope. If the specimen contains several crystals of different orientations as in figure 2.8 (b), then the diffraction pattern is the sum of the individual patterns. The spots are not randomly distributed, but tend to fall on rings of constant radii.

If the specimen consists of a large number of small crystallites (grains) of similar crystal structure, but at different orientations to one another (i.e a polycrystal as in figure 2.8(c)) the diffraction pattern will consist of a series of sharp concentric rings. It can easily be seen that this pattern evolves from a large number of single crystal diffraction patterns, each rotated by a small amount with respect to one another. In the case of an amorphous material, the constituent atoms are arranged entirely randomly and without any distinct repeating structure. For such materials the diffraction pattern will contain no discrete maxima. It
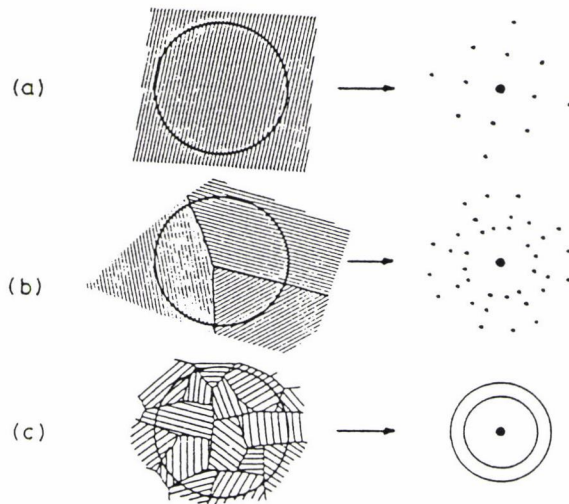
Figure 2.8 : *Types of diffraction pattern which arise from different specimen microstructure: (a) A single perfect crystal, (b) A small number of grains - notice that even with three grains the spots begin to form circles, (c) A large number of randomly orientated grains; the spots have now merged into rings.*

rather consists of diffuse diffraction rings around the bright central spot of unscattered electrons. Using the standard *Miller index notation* [Ha-90] to define plane and directions in the crystal, diffraction patterns can be interpreted. Using this notation for a cubic crystal for example the interplaner spacing of planes of the type (hkl) is given by

$$d_{hkl} = \frac{a}{\sqrt{h^2 + k^2 + l^2}}$$ (2.15)

where a is the lattice parameter of the unit cell and h,k and l the miller indices. For first order diffraction i.e. n=1, equation 2.14 becomes

$$\lambda = 2d \sin \theta$$ (2.16)

For small angles of θ, which is typical of electron diffraction, we can write $\sin \theta = \theta$, and equation 2.16 further reduces to

$$\lambda = 2d\theta$$ (2.17)

Consider now a beam of electrons impinging on a crystalline specimen as in figure 2.9 . Some of the electrons pass through the specimen without interaction and hit the screen or film

44

which is a distance L from the specimen, at O. Other electrons are diffracted through an angle θ by the crystal planes of spacing d, and these electrons hit the film at A, which is a distance r from 0. From simple geometry, it can be seen that for small angles of diffraction

$$\frac{r}{L} = 2\theta \qquad (2.18)$$

Combining equations 2.17 and 22.18, we find

$$\frac{r}{L} = \frac{\lambda}{d} \quad i.e. \quad rd = L\lambda \qquad (2.19)$$

λL is called the camera constant and is determined by analysing a known crystal. From equation 2.19 it can be seen that the distance of a diffraction spot from the undiffracted
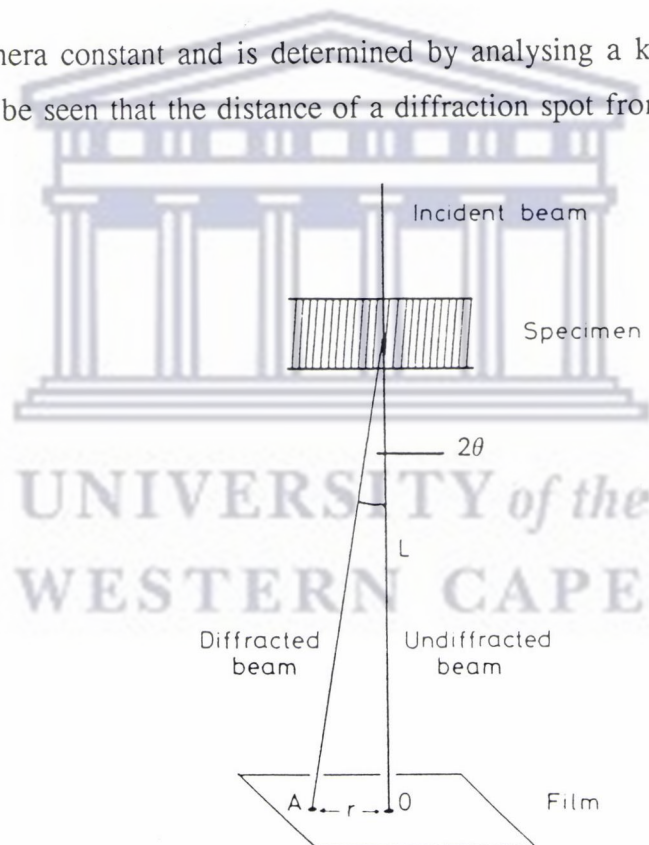

Figure 2.9 : *Schematic diagram showing the geometry of diffraction pattern formation.*

spot, r, is therefore inversely proportional to the d spacing of the diffracting planes.

45

A table of the $\lambda L/d_{hkl}$ - values for different (hkl) planes can be drawn up. By measuring r directly in the pattern on the photographic plate and comparing it with the values in the table, the pattern can be indexed, i.e. the respective h, k and l values can be determined.

An alternative method for indexing diffraction patterns involves determining the ratio between the magnitudes of two diffraction vectors as defined in the reciprocal lattice theory [Ha-90]. According to the theory for a face centred cubic (F.C.C.) crystal, the diffraction vector $\mathbf{g}_{hkl}$ is a reciprocal lattice vector such that d_{hkl} is given as in equation 2.15. The ratio between

$$|g_{hkl}| = r_{hkl} = \frac{1}{d_{hkl}} \tag{2.20}$$

the magnitude of two diffraction vectors on the photographic plate is therefore equivalent to the ratio between the magnitudes of the corresponding reciprocal lattice vectors, i.e

$$\frac{|g_{h_1 k_1 l_1}|}{|g_{h_2 k_2 l_2}|} = \frac{r_{h_1 k_1 l_1}}{r_{h_2 k_2 l_2}} = \frac{d_{h_2 k_2 l_2}}{d_{h_1 k_1 l_1}} = \frac{\sqrt{h_1^2 + k_1^2 + l_1^2}}{\sqrt{h_2^2 + k_2^2 + l_2^2}} \tag{2.21}$$

Tables can now be drawn up for the ratios between the $\sqrt{h^2 + k^2 + l^2}$ - values of all the

(hkl) planes in the crystal. In order to index the diffraction vectors $\mathbf{g}_{hkl}$, one only need to determine the distances of any two diffraction spots from the central undiffracted spot on the photographic plate. By comparing the calculated values with those in the table, the respective (hkl) indices can be assigned. Once two spots has been indexed the whole diffraction pattern can be indexed by superposition. The correct indexing can further be confirmed by calculating the angle between any two (hkl) planes and comparing it to the corresponding measured angle on the diffraction pattern. The angle, θ, between planes $(h_1 k_1 l_1)$ and $(h_2 k_2 l_2)$ in a F.C.C. crystal for instance can be calculated from

$$Cos\theta = \frac{h_1 h_2 + k_1 k_2 + l_1 l_2}{\sqrt{(h_1)^2 + (k_1)^2 + (l_1)^2} \sqrt{(h_2)^2 + (k_2)^2 + (l_2)^2}} \tag{2.22}$$

46

2.2.2.3 Experimental set-up in the TEM

Most of the TEM work was done on the Hitachi - 800 model which is a 200kV transmission electron microscope capable of obtaining a resolution of 0.204nm. The electron lens setup consists of a 2-stage illumination system and a 5-stage imaging system which enables observation of rotation-free transmitted electron images throughout the magnification range of 1000X to 600 000X. High vacuum is attained by a dual pumping system with a differential pumping design made up of two oil diffusion pumps of 570 litres per second and three oil rotary pumps of 160 litres per minute each. High performance and various functions are efficiently utilized by making use of a built-in computer which assumes overall control of the lens system, electron beam alignment system, evacuation system and the like.

An accelerating voltage of 200 kV and filament current of 20 μA was used during all observations. Throughout this investigation the first condenser lens was adjusted to a spot size of 1 μm. A condensor lens moveable aperture of 300 μm in diameter was used. An objective lens movable aperture of 70 μm in diameter was mainly used and during selected area diffraction a 30 μm diameter field limiting aperture, the smallest possible aperture on the machine, and a cameralength of 0.8 and 1.2 m were normally utilized. Photographs were normally taken in the 50 000X magnification range and twenty two 90X120 mm sheet film were mounted per cassette magazine.

All microdiffraction was performed on the Phillips EM430 Scanning Transmission Electron Microscope (STEM) which is a 300 kV machine equipped with a LaB_6 source thereby providing 10 times more brightness (than in the case of a tungsten source). This was useful since almost all diffraction was done using a nanoprobe. A cameralength of 0.7 m was almost exclusively used. For all imaging and diffraction the specimen was mounted on a 3.05 mm copper grid and then placed into a specimen holder for the eucentric side entry goniometer stage.

2.2.2.4 Specimen Preparation

Specimen preparation for Transmission Electron Microscopy was done with considerable

skill. Absolutely great care was taken to ensure that the specimen accurately reflects the nature of the bulk material, to ensure its stability in that it does not lead to either chemical change and to ensure that it is clean and smoothly thinned since artifacts may arise. Although it is preferable for a specimen to be flat and parallel-sided so as to eliminate thickness fringes and reduce the number of extinction contours in a crystalline specimen, this however, was difficult to obtain after atom milling. In spite of not working with a perfectly flat and parallel-sided specimen, a wealth of information was nevertheless extracted in the Transmission Electron Microscope. Since all the specimens used in this investigation were partially electrically and thermally conductive, it helped to avoid charge build-up and too great a rise in specimen temperature during examination.

In this investigation the following standard procedure was followed in preparing specimens for cross-sectional TEM examination. These included sample cleaning, gluing to form a sandwich, cutting, polishing and lapping and finally atom milling.

Two 5 mm X 10 mm samples were placed face upwards on a teflon block together with two dummies (of the same size) on both sides of the two samples as in figure 2.10 .The main advantage of two unreacted silicon dummies on both sides is the additional mechanical strength provided to the sample during the mechanical thinning process. A further advantage is that when one gets to the polishing and lapping stage in which the samples is sandwiched between the dummies, one can afford to apply polishing and lapping until a considerable portion of the outside dummies disappear, thereby giving an indication as to the thickness of the sample. In this way one also ensures that the final product will be able to cover a TEM grid completely as this improves observation in the atom mill. It is highly recommended that the dummy pieces be of different thickness to that of the actual samples as this would make identification of the different layers easier in the final product of the cross-sectional sample before mounting on a grid. Samples and dummies were cleaned with acetone followed by methanol using a small sable brush to remove possible debris from the surfaces. After making sure that the samples were dry, a small amount of M-Bond 610 glue were applied to the upper contacting surfaces of the two samples. The one piece was
flipped over on top of the other so that the two faces that contain the important surface layers face each other. The dummy pieces on either side of the two samples were glued in a similar

fashion with all polished (shiny) surfaces facing inward with the samples in the centre, sandwiched by the dummies (see figure 2.11). The sandwich was now carefully clamped between two pieces of cardboard in a press. The whole assembly was left at about 115°C for
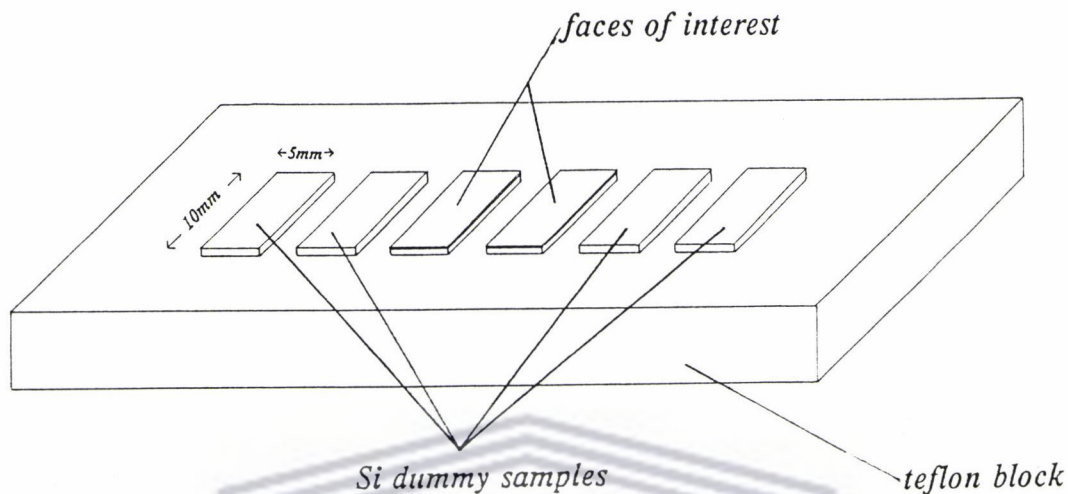

Figure 2.10 : *Getting samples and unreacted Si dummy samples ready for cleaning.*

3 hours for the glue to set. The sandwich was now mounted on a glass slide using crystal bond wax. The glass slide with the sandwich was then mounted onto a diamond saw which
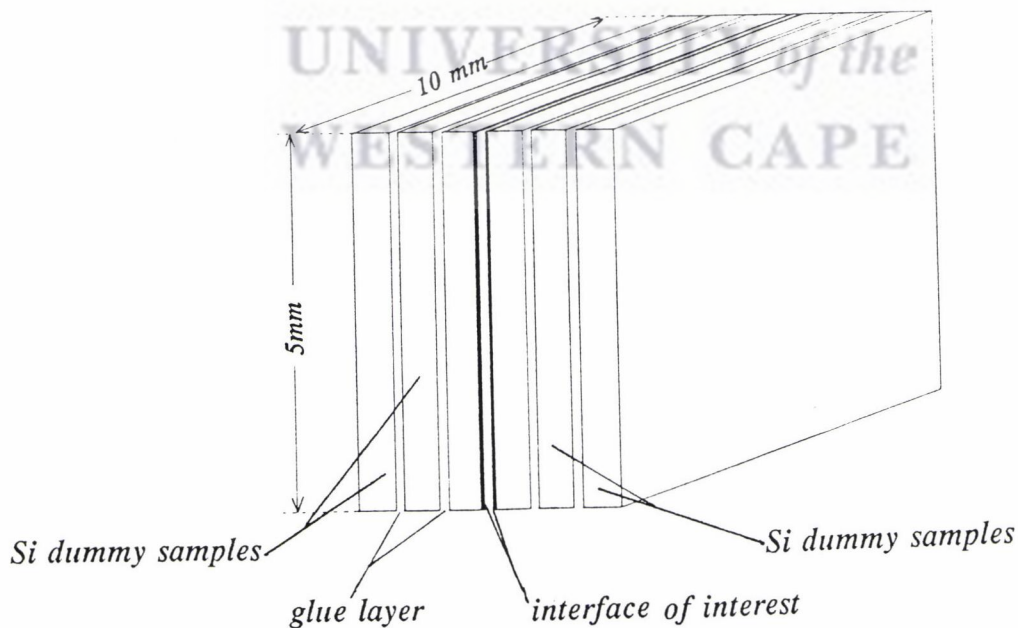

Figure 2.11 : *A sandwich with sample faces facing each other.*

had a 0.4 mm thick rotating blade. This circular saw blade which have been impregnated with small diamond particles was then used to cut thin slices (0.5 mm thickness) from the specimen at a relatively low cutting speed. A cutting fluid was continuously applied during cutting to serve as a lubricant to reduce specimen heating. The cut pieces which remained on the glass slide were remove by again melting the wax. These slices were cleaned ultrasonically with trichloroethane for about 5 to 10 minutes followed by acetone to remove all traces of cutting oil and remaining wax. Four to five samples were mounted on a round glass polishing block using crystal wax, making sure they were evenly spread over the surface and all surfaces of interest are placed parallel to each other (see figure 2.12). Mounted samples were firstly ground down using 240 grit, 400 grit and 600 grit emery paper in succession after which samples were lapped on a polishing cloth with 0.3 μm alumina powder. To ensure that grinding and polishing take place evenly, the glass block was rotated through 180° at regular intervals.
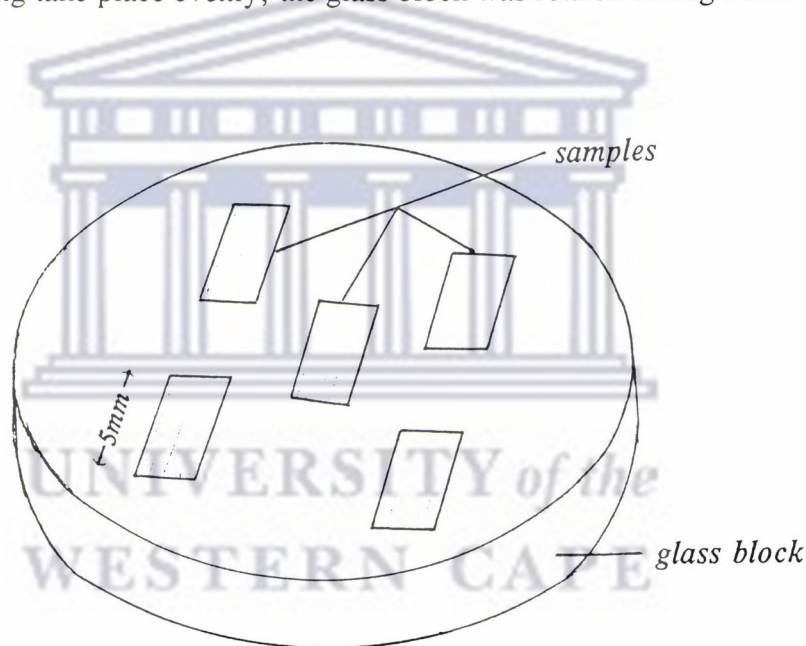

Figure 2.12 : *The positioning of samples on the glass block for polishing and lapping.*

Water was used as a lubricant. After polishing the one side of the samples to a mirror image free from any scratches, the wax was melted and samples turned over to the other side for similar treatment. The thickness of the samples were frequently measured using a Starrett micrometer until a thickness of about 15 μm was obtained. The glass block was then placed upside down in a watchglass filled with acetone for the wax to dissolve and the samples to drop from the block. At this stage the samples were extremely fragile and was therefore

https://etd.uwc.ac.za/

handled with great care. After the samples were removed from the watchglass with a small sable brush, they were placed onto a teflon block. A small amount of epoxy was applied to 3mm TEM copper slot grids (2 mm x 1 mm) which in turn was placed onto the samples using tweezers, making sure that the interface of interest is exposed through the slot. After waiting for about 30 minutes at room temperature for the epoxy to harden, the grid was cleared from excess overlapping sample material and then placed in the atom mill.

In the atom mill the specimen is clamped between two tantalum plates which have a small hole of 2mm diameter at their centres in a holder which is rotated in a horizontal plane. Argon ion beams from two ion guns impinge on the upper and lower surfaces of the specimen. During ion beam milling the energetic argon ions sputter atoms from the specimen till there are areas which are thin enough for electron beam transmission. The direction of incidence of the ions were initially set at 20°, the ion beam current at about 170 μA and the high voltage to the saddle field guns at 5 kV. Under these conditions about 3-4 μm per hour were removed from the target. During the last hour atom milling took place at an incident angle of 12.5°. The whole process took place at pressures of about 10^{-4} mbar.

2.2.3 Scanning Electron Microscopy (SEM)

In many respects the scanning electron microscope (SEM) is very similar to the TEM. A schematic representation of the scanning electron microscope column is given in figure 2.13. In the SEM the electron beam is also generated within an electron gun and accelerated by a high voltage and formed into a fine probe by electro-magnetic lenses. As in the TEM, the electron-optical column through which the beam passes, is held under a high vacuum to allow a free path for the electrons and to prevent high voltage discharge. The electron gun in the SEM operates exactly on the same principle as in the TEM. However, much lower accelerating voltages (between 5 to 40kV) are used in the SEM which make the gun smaller in size and less complex. The major difference between the SEM and the TEM lies in the image formation (see section 2.2.3.1). A ray diagram of a two lens SEM is given in figure 2.14. The first lens that influences the electron beam is the condenser lens which causes the electron beam to converge and pass through a focal point which is produced above a condenser aperture. The condenser lens, in conjunction with the chosen accelerating voltage

51

is primarily responsible for determining the intensity of the electron beam when it strikes a given specimen. The beam will diverge again below the condenser lens aperture.

A final lens (the objective lens) is used to bring the beam into focus at the specimen by demagnifying (converging) it to a focal point at the specimen surface. The final lens
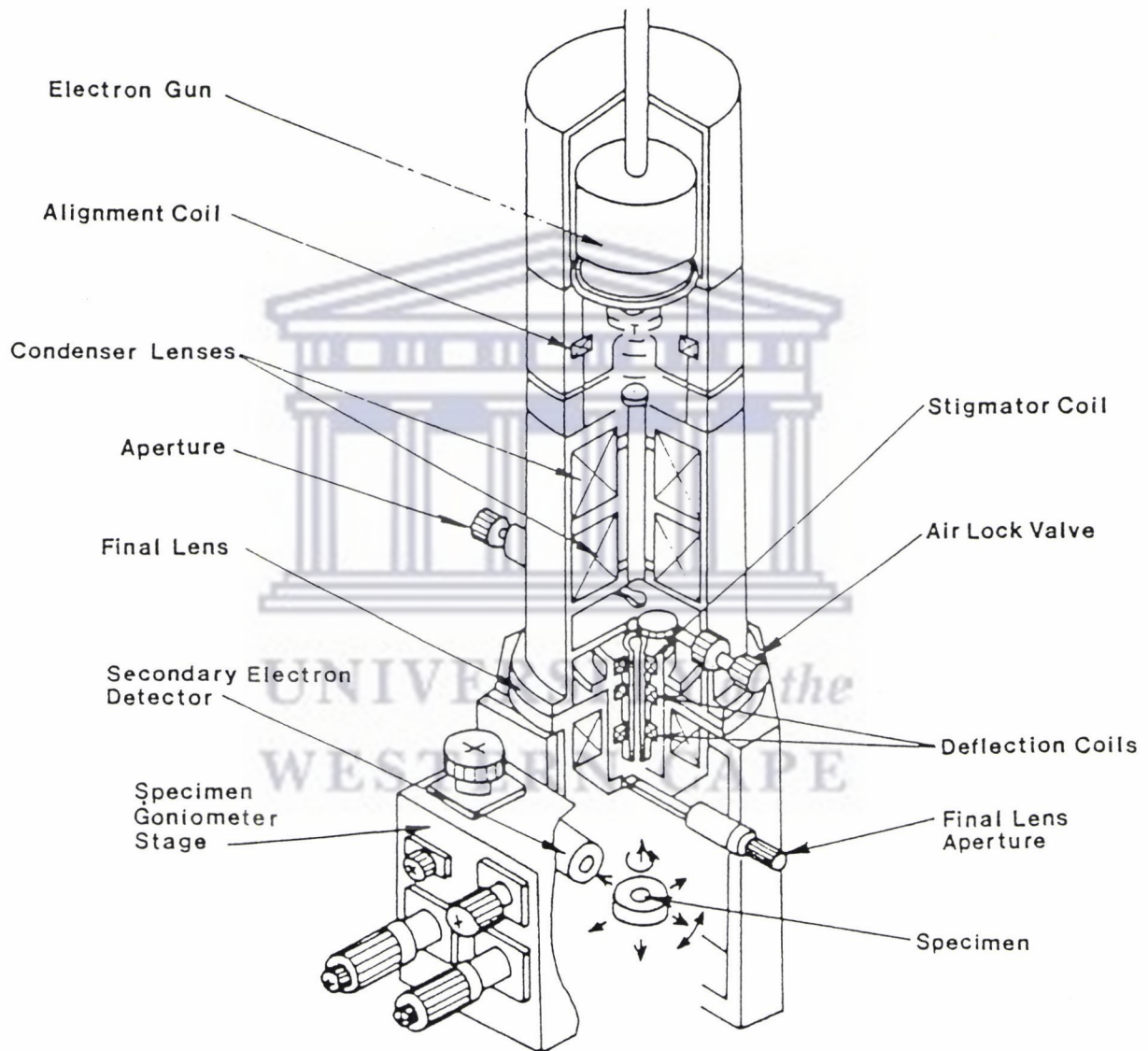

Figure 2.13 : *Schematic representation of a scanning electron microscope column (Courtesy of Hitachi, Ltd.).*
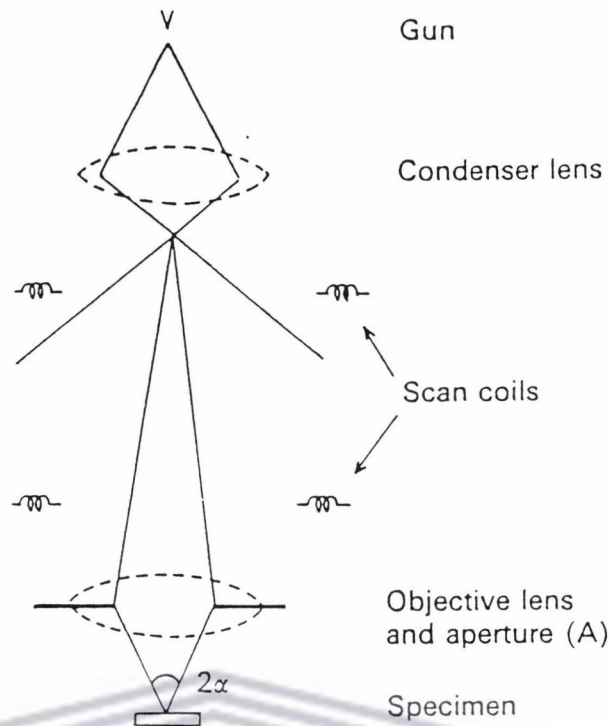
Figure 2.14 : *Ray diagram of a two lens SEM.*

demagnification determines the diameter or spot size of the electron beam at the specimen which in turn determines the specimen resolution (see section 2.2.3.2)[Go-75,Pe-65].

2.2.3.1 Imaging in the SEM

A schematic representation of the basic components of the imaging system in the SEM is shown in figure 2.15. For scanning electron microscopy, as its name implies, the specimen is traversed by a electron beam. The movement is achieved by scanning (raster) coils in the microscope column controlled by a scan generator. The raster pattern of the primary electron beam is synchronized with the scanning pattern of the cathode say tube (CRT) yielding a point-by-point translation. Thus by coupling the deflection coils of the CRT to the scanning coils of the microscope a one-to-one presentation of the area scanned is produced (figure 2.15). The signals produced, as a result of the beam being rastered across the specimen surface, are collected by an appropriate detector, amplified and displayed on the CRT. The magnification of the image is the relationship between the length of the scan line on the specimen and that on the CRT.
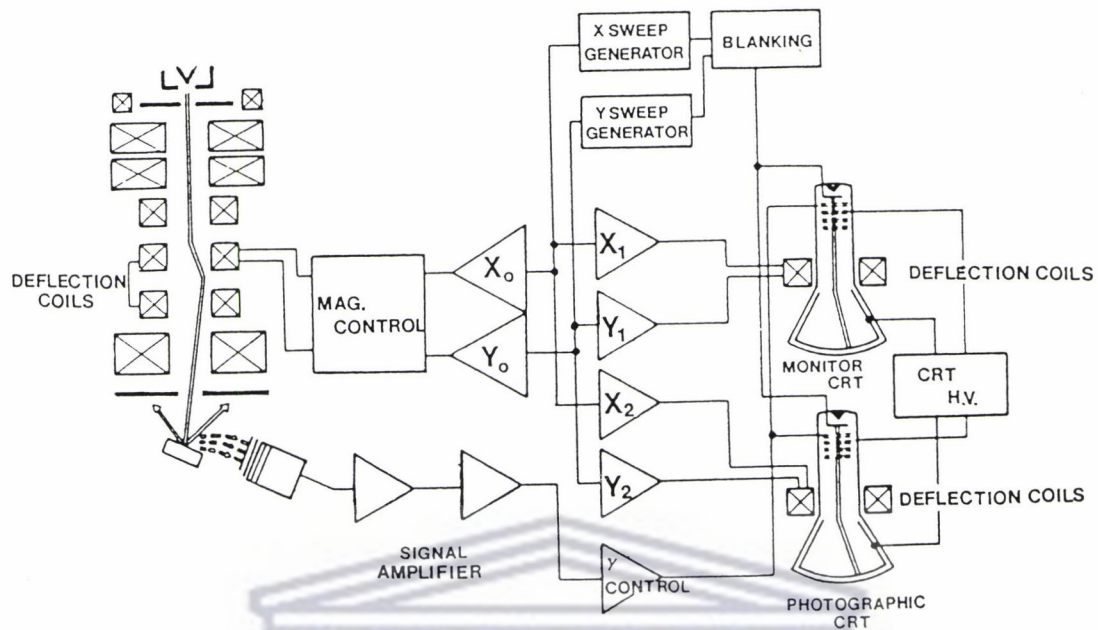
https://etd.uwc.ac.za/

Figure 2.15 : *Schematic representation of selected electronic components of the SEM showing the coupling of the deflection coils found in the column with those found in the cathode ray tube.*

2.2.3.2   Resolution

The ability of the instrument to resolve fine structure is limited by the diameter of the probe, and the number of electrons contained within the probe. The picture is effectively made up of lines of image points, each point being the size of the beam probe. If a structure is smaller than the probe it is not resolved. If, however, the probe is too small in relation to the area being imaged, it misses out on several smaller regions on the specimen thereby forming a poor quality image. There is a finite relationship between magnification and the optimum probe size to obtain the derived signal level, and it does vary from specimen to specimen. The ability of any microscope to see a fine structure is known as its resolution limit. In the modern scanning electron microscope resolution levels down to 4 nanometres are typical. The relationship between resolution and wavelength is given by Abbe's equation, namely

54

$$d = \frac{0,612\lambda}{nSin\alpha} \qquad\qquad (2.23)$$

where d is the resolution (d should be small), λ the wavelength of the energy source, n the index of refraction of the medium through which the energy source travels and $\propto$ the aperture angle as illustrated in figure 2.16. The overall significance of this equation is that it mathematically expresses the limit of resolution for an optical system [We-74].

2.2.3.3   Depth of field and working distance

Depth of field is the extent of the zone on a specimen which appears acceptably in focus at any one time (see figure 2.16). A main feature of the scanning electron microscope is its
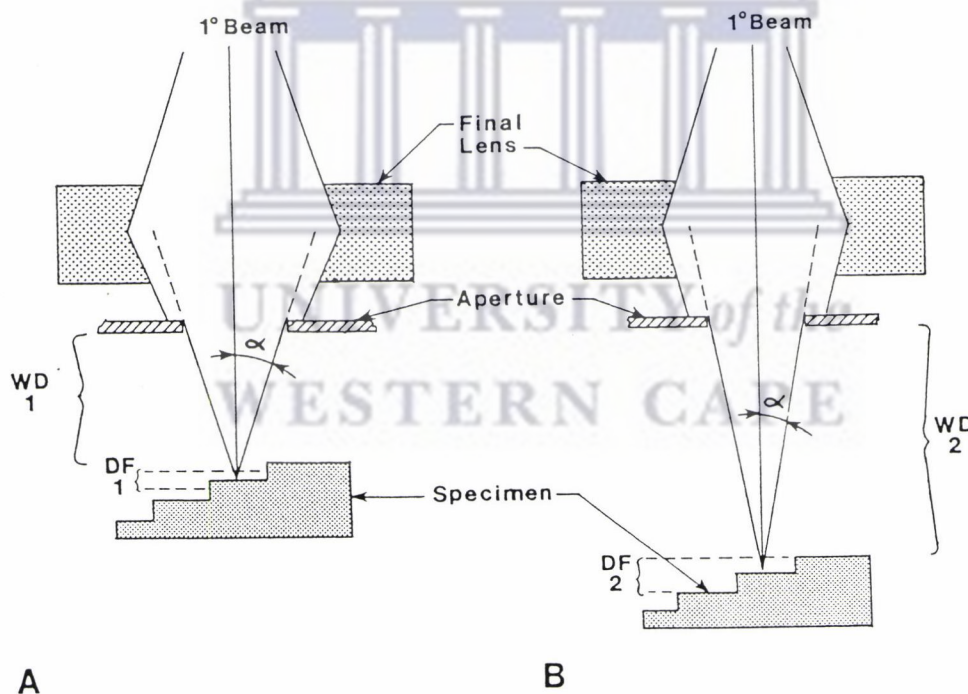

Figure 2.16 : *Enhancement of depth of field by increase in the working distance thereby decreasing the aperture angle. (A) Short working distance (WD), (B) Longer working distance showing increased depth of field (DF).*

55

ability to provide what looks like three dimensional images, due to its ability to operate with a very large depth of field. An aperture placed in the final lens is not only used for reducing spherical aberration in the lens but also affects the depth of field directly by determining the angle aperture $\propto$ (see figure 2.16). Typical final lens apertures varies from about 100 to 400 μm in diameter.

One method for enhancing the depth of field in the SEM is to lower the specimen from the final lens, thus increasing the working distance which is defined as the distance between the final lens pole piece to the uppermost portion of the specimen, thus effectively decreasing the aperture angle (see figure 2.16). Shorter working distances are used for high resolution or low kV operation, under which circumstances the final lens is operated at a high current, providing focus with the minimum of aberration. Longer working distances allow a lower magnification to be achieved, but the weaker objective lens currents required increase the effect of spherical and chromatic abberations.

2.2.3.4 Electron beam-specimen interaction

Solid specimens subjected to electron beam excitation in a scanning electron microscope exhibit complex interactions with primary beam electrons. These interactions result in a variety of signals that may be detected in the scanning electron microscope (see figure 2.17). These signals include secondary electrons, backscattered electrons, transmitted electrons or specimen current. Information regarding specimen composition can also be determined by making use of the X-ray and Auger electron signals or even by measuring cathodoluminescence. With the appropriate detection device for a specific signal a wealth of information can be extracted. In this investigation both the reflected primary electrons and the secondary electrons was utilized. Much better contrast can be obtained by using the more energetic reflected electrons (in the order of kilovolt). The lower energy ($<$50 eV) secondary electrons can be eliminated by applying a voltage (~200 V) to the detector. Use was also made of Energy Dispersive X-ray analysis (EDX).

In order to study surface morphology in the SEM, the surface of the sample must be electrically conductive for effective viewing. This necessity arises from the statistics of

56

electron yield when a material is bombarded with electrons. During normal operation the ratio of the number of electrons emitted from the surface per unit time to the number of
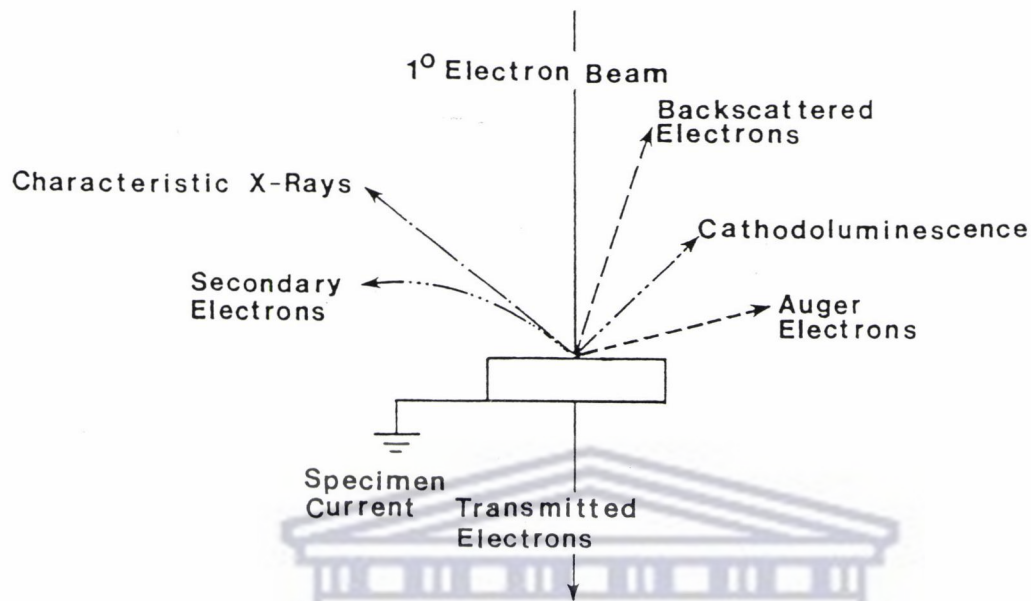
Figure 2.17 : *Illustration of seven of the possible signals generated by the* primary electron beam-specimen interaction in the scanning electron microscope.

primary electrons incident on the surface per unit time is less than unity, resulting in a surplus of electrons building up at the surface. If no conduction to earth is possible, the sample becomes negatively charged until the incident electrons are repelled and a distorted image results. Coating specimens with a thin layer of a conductive material helps to overcome there problems. An additional advantage of coating may be an improvement in the strength of the secondary electron signal from the specimen surface.

2.2.3.5   Experimental set-up in the SEM

Scanning electron microscopy was carried out on the Hitachi X-650 SEM which is a 40 kV machine offering resolution of up to 6nm. This machine is highly advanced as almost all functions or modes and allignment settings can be done either electronically or electromagnetically. The machine is equipped with a secondary electron detector and a

backscattered electron detector for normal imaging, and a solid state detector for elemental analysis as well as electron beam induced current imaging. The machine utilizes a 3-stage electromagnetic lens system and the only moveable aperture is the objective aperture which was normally set at 400 μm. A working distance of 5 mm was generally used to further boost the resolving power of the machine except in cases where a backscattered electron image was collected in which case the working distance was adjusted to 15 mm due to a positioning constraint. Accelerating voltages of 10 kV and 30 kV were used interchangeably to bring out certain features on the specimen surface or from slightly below the surface. Filament currents between 70 and 80 μA was generally used. X-ray analysis (EDAX) was used as a qualitative tool to identify elements within the sample.

2.3.4 Auger Emission Spectroscopy (AES)

2.2.4.1 General

During inner shell electron vacancy formation by photon irradiation or energetic electron and proton irradiation, the excited atoms can release their energy in radiative transitions with the emission of X-rays or in nonradiative transitions with the emission of electrons. The latter process forms the basis for Auger Electron Spectroscopy (AES) in which one determines composition by measuring the energy distribution of electrons emitted during irradiation with a beam of energetic electrons. As with other electron spectroscopies, the observation depth is about 1-3 nm and is determined by the escape depth. The identification of atoms by core level spectroscopies is based upon the values of the binding energies of the electrons. With AES the energy of the emerging electron is determined by the differences in binding energies associated with the de-excitation of an atom as it rearranges its electron in the shells and emits electrons (Auger electrons, named after its discoverer, Pierre Auger) with characteristic energies. Figure 2.18 shows the Auger radiationless de-excitation processes, in which the atom is left in the final state with two vacancies (or holes). If one of the final state vacancies lies in the same shell as the primary vacancy (although not in the same subshell), the radiationless transition is referred to as a Coster-Kronig transition. This transition is significant because the Coster-Kronig transition rate are much higher than the normal Auger transitions and influence the relative intensities of the Auger lines. For example in figure

2.18 if an L_1 has a vacancy, the L_2 to L_1 transition will be rapid (Coster-Kronig), therefore reducing M electron to L_1 vacancy transitions. For K shell transitions, the
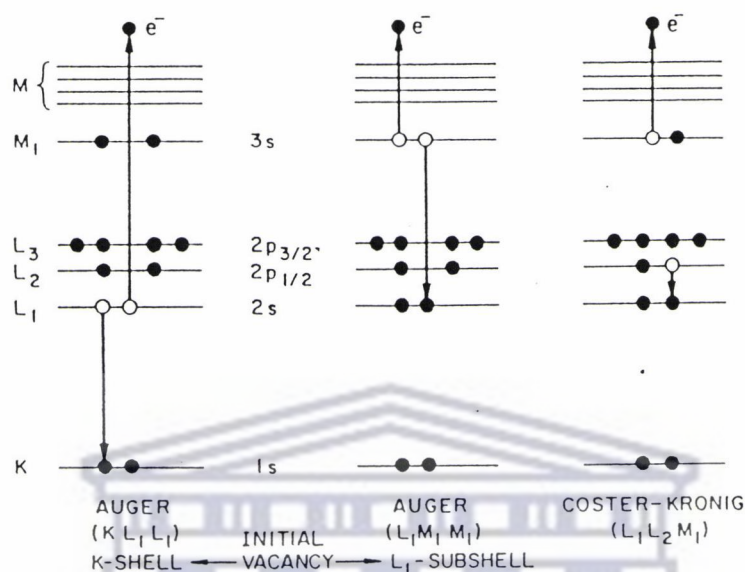

Figure 2.18 : *Schematic diagram of various two-electron de-excitation processes. The KL_1L_1 Auger transition corresponds to an initial K hole which is filled with an L_1 electron and simultaneously the other L_1 electron is ejected to the vacuum. The LM_1M_1 Auger transition is the corresponding process with an initial 2s vacancy. The Coster-Kronig $L_1L_2M_1$ transition contains an initial L_1 hole which is filled with an electron from the same shell (but different subshell, L_2).*

fluorescence yield is less than 0.1 for binding energies less than 2KeV, and the total Auger yield is larger than 90% for low Z elements (Z<15). This is so since X-ray transition becomes the preferred method of de-excitation only when the initial core hole is deeper than about 10KeV as in elements with higher Z-values. Auger electron spectroscopy is a surface sensitive technique. In general, small amounts of typical contaminants like C, N and O are easily detected. Hydrogen cannot be detected in Auger measurements since 3 electrons are needed in an Auger transition.

2.2.4.2   Experimental set-up for AES

As with the other electron spectroscopies, Auger analysis is carried out under high vacuum conditions. Figure 2.19 shows schematically an experimental apparatus.
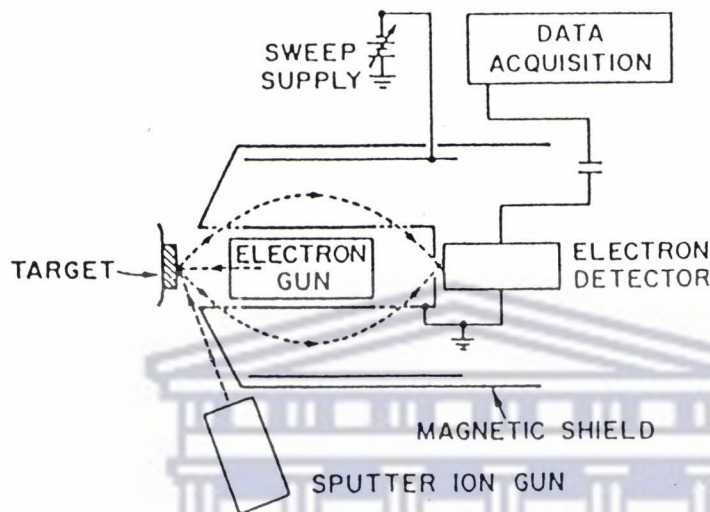

Figure 2.19 : *Experimental apparatus used in Auger spectroscopy. [After Palmberg in Czanderna et al., 1975.]*

The cylindrical mirror analyzer (CMA) has an internal electron gun, whose beam is focused to a point on the specimen sample at the source point of the CMA. Electrons ejected from the sample pass through an aperture and are then directed through the exit aperture on the CMA to the electron multiplier. The pass energy E is proportional to the potential applied to the outer cylinder, and the range ΔE of transmitted electrons is determined by the resolution R $= \Delta E/E$, where R is typically 0.2-0.5% .

For this investigation the following parameter-settings were used during Auger analysis. The accelerating voltage across the anode and cathode in the electron gun was set at 3000V while an electron gun emission current of 1mA was maintained. The same voltage was applied to the sputter gun but a sputter gun emission current of 15mA was used. The voltage applied to the electron multiplier was 1V and a signal modulation voltage of 3eV was maintained.

60

The lock-in amplifier assumed a magnification of 10 and a sensitivity of 0.001 seconds. Under the above conditions the sputtering rate was 3.5 nm per minute.

In a spectrum Auger electron transitions generally appear as small features superimposed on the large background of secondary electrons. The unsual practice is to use derivative techniques and generate a dN(E)/dE function so as to minimize the contribution from the slowly varying background. The "differentiation" is conveniently done electronically by superimposing a small ac voltage on the outer cylinder voltage and synchronously detecting the in-phase signal from the electron multiplier with a lock-in amplifier. The y-axis of the recorder is then proportional to dN(E)/dE, and the x axis to the kinetic energy E of the electrons. A typical spectrum is given in figure. 2.20 below. The total backscattered background current with energy greater than 50KeV is typically 30% of the primary beam current. The noise level due to this current and the ratio of the analyzer ΔE to Auger line width generally establishes the signal to noise ratio and hence the detection limit for impurities in the sample. A typical value for the detection limit is 1000 ppm, ~0.1 atom %.
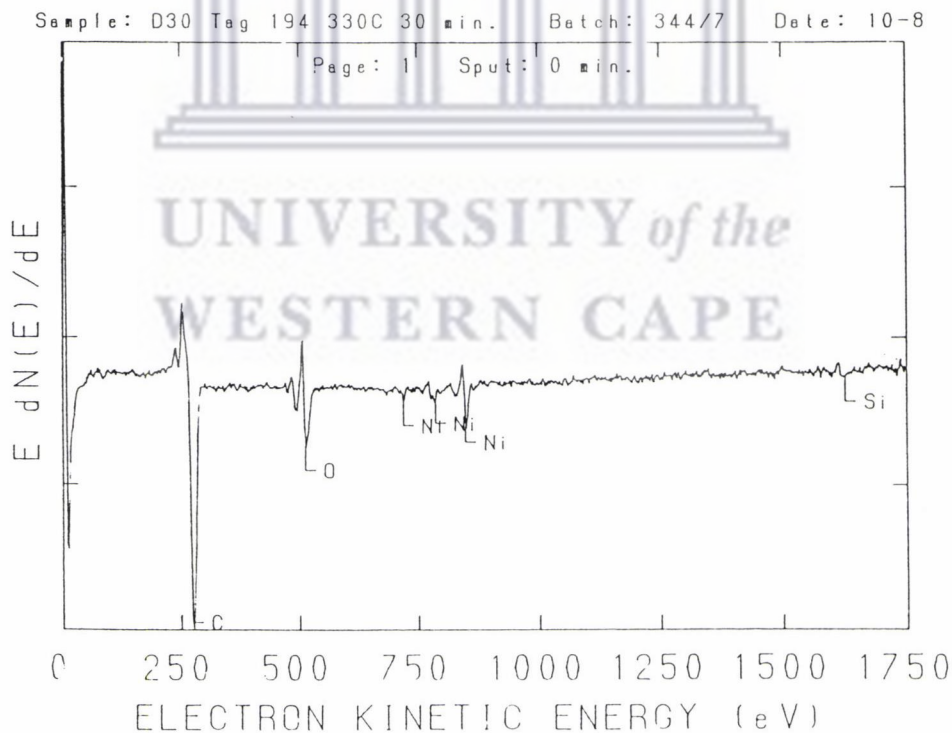

Figure 2.20 : *A typical Auger spectrum.*

61

2.2.4.3   Auger depth profiles

A major use of Auger electron spectroscopy is determining the composition as a function of depth in thin films and layered structures. The conventional apparatus is illustrated in figure 2.19, which consists of an electron gun and CMA assembly as well as a sputter ion gun. The Auger signal is generated in the near surface region of the sample (~3 nm) and ion sputtering provides the layer sectioning technique required for depth analysis. In routine laboratory use, the depth profiles are shown as Auger signal height profiles versus sputter time. Further calibrations are required to convert sputter time to depth and signal height to atomic concentration. The combination with RBS is quite useful in such depth profile analysis because RBS gives quantitative information on depths and heavy mass constituents without the complications introduced by the intermixing due to sputtering. Ion sputtering causes a change in the composition of the surface layers due to surface segregation and preferential sputtering. As compared to RBS, Auger depth profiling provides better depth resolution and is sensitive to both heavy and light elements.

One of the advantages of Auger electron spectroscopy is its sensitivity to low mass impurities, such as carbon and oxygen, which are common contaminants at surfaces and interfaces. The presence of these interfacial contaminants plays a disruptive role in thin film reactions by retarding interdiffusion. The degradation of the planarity of thin film structures following thermal processing is often directly correlated with these contaminants. When confronted with a layered or thin film sample containing unknown impurities or contaminants, sputter depth profiling with Auger analysis often represents the starting point for initial analyses.

2.2.5 X-ray Diffraction

2.2.5.1   General

The analysis of the elemental composition of thin films is often aided through the use of diffraction techniques which can uniquely identify crystalline phases near a solid surface. X-ray diffraction is most suited to films thicker than a few tenths of nm. To limit the penetration of the beam and enhance the diffraction pattern of the film with respect to the

62

substrate, glancing angle geometries are used. Individual crystalline phases were identified by their characteristic diffraction patterns. Such X-ray patterns also reveal information on the orientation and size distribution of the crystallites.

X-ray techniques provide superior angular resolution and more accurate structural data than available from electron diffraction but over a large volume area of the sample. On the other hand, diffracted intensities can be much smaller for X-ray than for electrons necessitating long exposures. A major advantage of X-ray diffraction is in conjunction with electron microscopes which permit diffraction analysis within a very small region of the sample. The basis of X-ray diffraction is the Bragg equation which describes the conditions for constructive interference for X-rays scattering from atomic planes of a crystal. The condition for constructive interference is

$$2d\sin\Theta = n\lambda$$

where λ is the wavelength of the incident radiation.

The Bragg law requires that Θ and λ be matched for diffraction. The condition may be satisfied by varying Θ, in other words varying the orientation of a single crystal. In thin films the distribution of crystalline orientations is nearly continuous. Diffraction occurs from crystallites which happens to be orientated at the angle to satisfy the Bragg condition.

2.2.5.2   Experimental setup for XRD

A Schematic illustration of the x-ray diffraction set-up is given in figure 2.21. X-ray diffraction spectra were obtained by means of a Phillips vertical diffractometer, with the Bragg - Brentano geometry. With this configuration, both the sample and the detector tilt during the accumulation of the spectra, with the sample moving through an angle Θ while the detector moves through 2Θ. X-rays were obtained from a monochromatic X-ray beam impinging on the sample. Specimen and detector movements were controlled by a computer which permits digitized data acquisition with variable time and step-size parameters. The spectra in this work were obtained using a step size of 0.2° and an accumulation time of 2 seconds per step. The X-ray diffraction intensity and angle to which it refers were stored on a magnetic disk, so that data, manipulation and processing could be carried out later. The

63

(hkl) values as a function of 2Θ were calculated by a computer program which was based on the atomic scattering factors and positions of the atoms in a unit cell. By entering the experimentally observed angle at which a peak was detected into a separate file, a quick
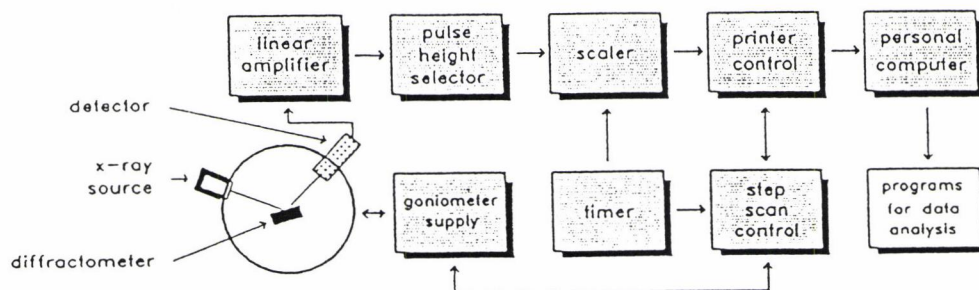

Figure 2.21 : *Schematic diagram showing the instrumental X-ray diffraction set-up.*

search could be done to give the corresponding compounds with allowed reflections at this angle. In this way, actual phases present in the specimen were identified.

CHAPTER 3

NICKEL SILICIDE FORMATION

3.1 RESULTS AND DISCUSSION

3.1.1 Ni_2Si FORMATION

Nickel silicide formation was analysed for comparison with results reported in the literature (see section 1.7). In figure 3.1 RBS-spectra for first phase formation at 290°C is shown. Figure 3.1(a) shows an RBS-spectrum of the virgin sample and figure 3.1(b) the spectrum of a sample annealed for 5 minutes. Notice the sharp shoulders on the original silicon and nickel peaks. This suggests that Ni_2Si grows in layers of uniform thickness as is evident in the cross-sectional TEM micrograph of the same sample (figure 3.2(a)). The interfaces between the silicide layer and the unreacted nickel and between the silicide and underlying silicon substrate are relatively sharp. Ni_2Si can be seen from the micrograph to be polycrystalline. After 20 minutes of annealing it can be gathered from the RBS spectrum (figure 3.1(c)) and corresponding cross-sectional micrograph in figure 3.2(b), that all the nickel has been transformed to a uniform polycrystalline layer of Ni_2Si. The full thickness of the Ni_2Si layer was found to be about twice as large as the initial deposited Ni layer. This is more or less consistent with the results reported in literature. The full thickness is however not portrayed throughout the silicide layer in figure 3.2(b). Note that the contrast on the glue side is purely a diffraction effect resulting from slight folding at the edge. It is speculated that this damage has been done during atom milling. The grains seem to traverse the thickness of the silicide layer and are elongated. One would expect these grains to grow even larger until the next phase is initiated. In fact it was found in this investigation that if Ni_2Si is formed at a higher temperature (for shorter times) the grains are much larger and well formed. Ni_2Si was found to be stable at 290°C for up to about 30 minutes after which some diffusion of Ni in Ni_2Si has already taken place to make way for second phase formation (i.e NiSi). It can be seen in the RBS spectrum in figure 3.1(d) that after 30 minutes of annealing some Ni diffusion in Ni_2Si has taken place. This is the initial stage of NiSi

65

AUGER analysis was performed on the virgin (unannealed) and the annealed samples at 290°C for 5 minutes. The respective spectra which were collected on the surface of the samples (i.e. for a sputter time of zero minutes) are given in figure 3.3. It is apparent from
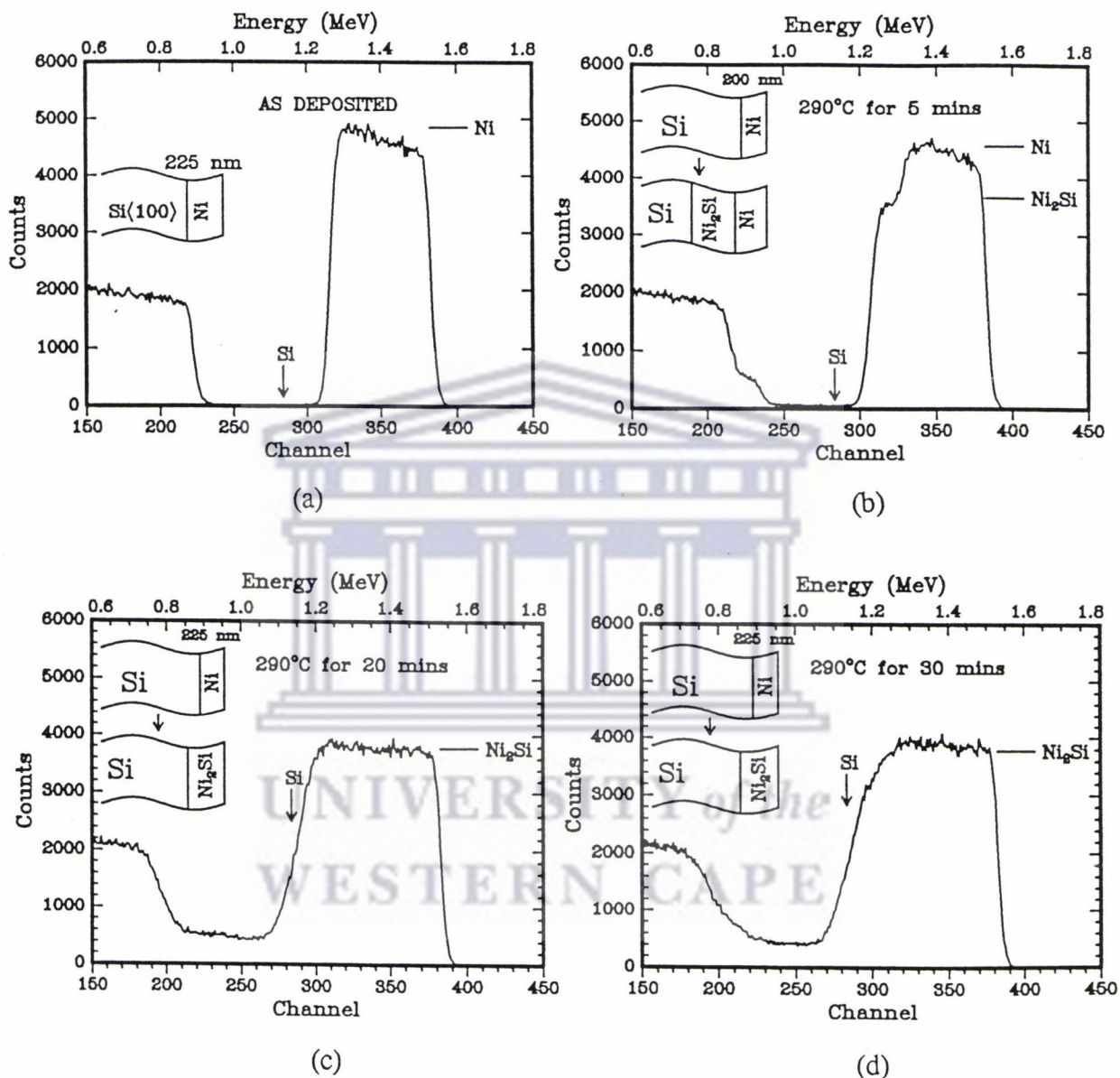

Figure 3.1 : *RBS-spectra showing the formation of the first phase, namely Ni$_2$Si. In (a) the as-deposited sample is shown. After annealing at 290°C for 5 minutes, Ni$_2$Si had started to grow (b). After 20 minutes of annealing at the same temperature (c), Ni$_2$Si has been fully formed. After 30 minutes of annealing (d), some diffusion of Ni in Ni$_2$Si has already taken place to make way for second phase formation (i.e. NiSi). (b) and (c) suggest that Ni$_2$Si and NiSi does not co-exist with unreacted Ni-metal.*
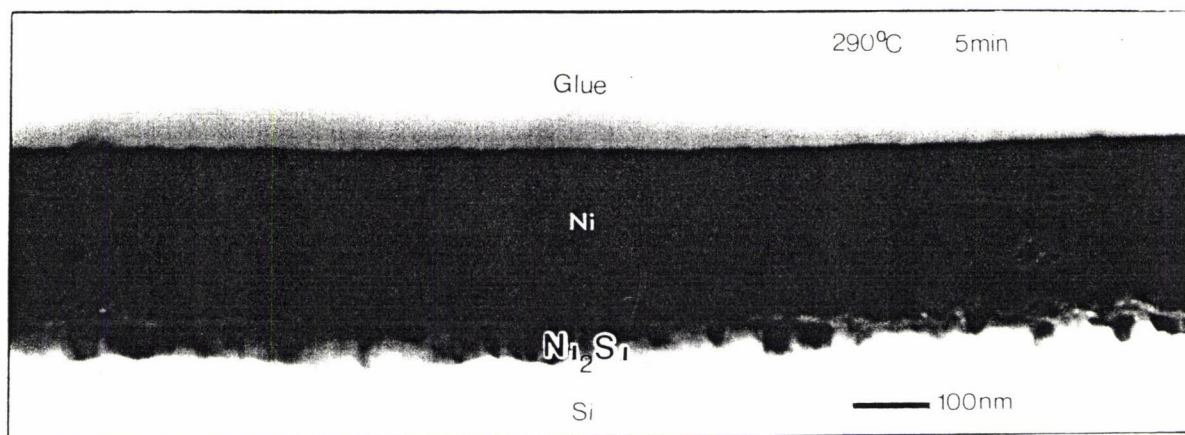
(a)
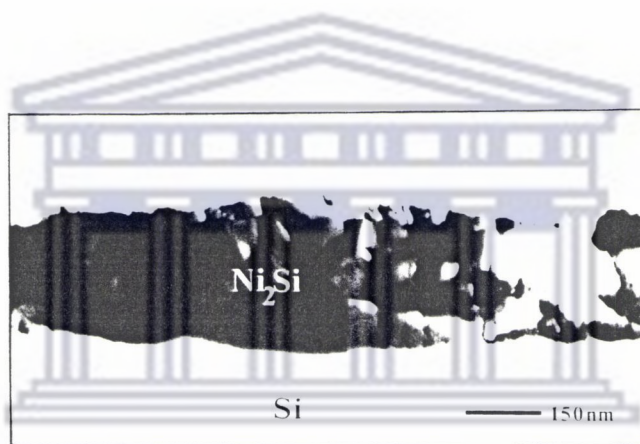
(b)

Figure 3.2 : *Bright field TEM micrographs showing Ni₂Si formation (a) after annealing at 290°C for 5 minutes and (b) after annealing at 290°C for 20 minutes.*

the spectra that oxidation has taken place in both samples but is more severe in the annealed sample. Carbon contamination is also more severe in the annealed sample. According to the AUGER analysis the carbon contamination layer extends for about a 7nm below the surface in both samples. Although the oxide layer was also about 7nm thick in the case of the unannealed sample, this layer extended much deeper below the surface in the case of the annealed sample. A summary of the AUGER results for both samples is reflected in the peak to peak height data in table 3.1 and table 3.2 respectively.
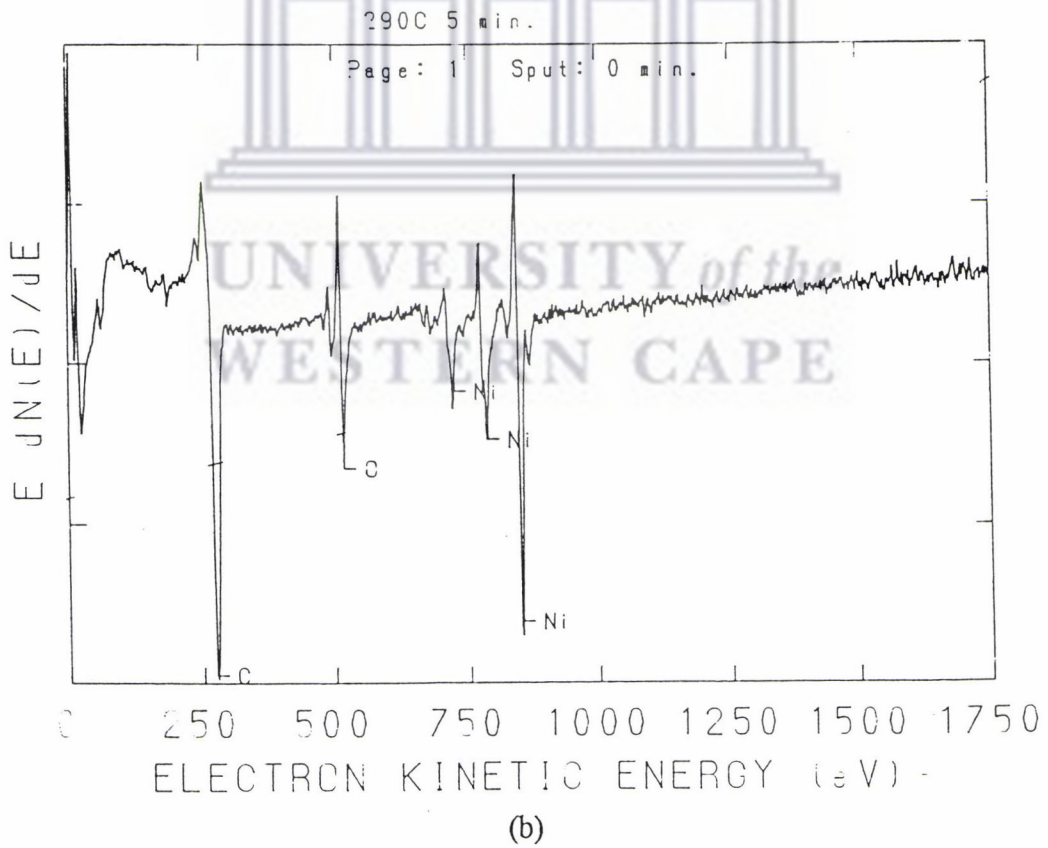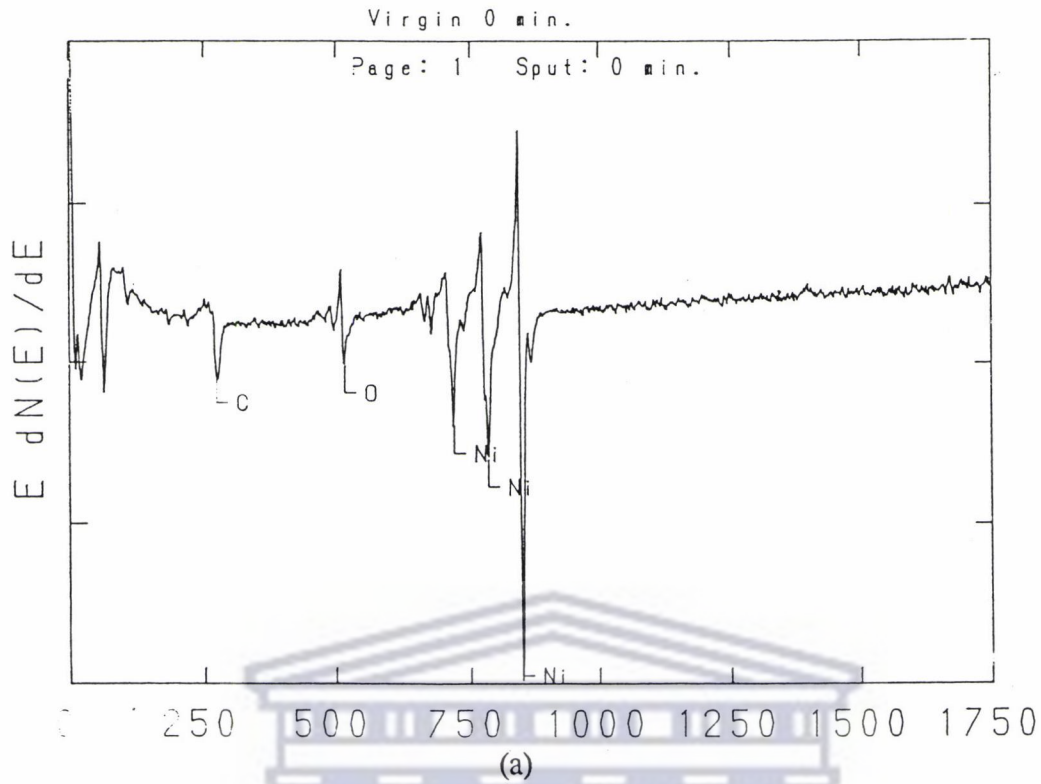
67

Figure 3.3 : *Auger spectra taken on the surface of (a) an unannealed sample, and (b) a sample annealed at 290°C for 5 minutes.*

Table 3.1(a) : *Peak to peak height data as a function of sputter time of an unannealed sample. The electron kinectic energy (eV) at which the various peaks are found as well as the respective sensitivities are indicated at the top of each column.*

Sputter Time (min)	Nickel Ni (848,.27)	Silicon Si (92,.36)	Silicon Si (1619,02)	Oxygen O (512,.51)	Carbon C (272,.19)
0.0	14054	0	0	2251	1597
1.0	16811	0	0	335	229
2.0	16841	0	0	133	20
3.0	15180	0	0	0	0
4.0	15895	0	0	0	0
5.0	15510	0	0	0	0
7.0	15144	0	0	34	0
10.0	14195	0	0	0	0
15.0	12788	0	0	0	0
20.0	11881	0	0	0	0
25.0	10682	0	0	0	0
30.0	9966	0	0	0	0
35.0	8926	0	0	0	0
40.0	7472	1161	0	0	0
45.0	4576	5547	951	0	0
50.0	1965	7431	1340	0	0
55.0	547	7969	1557	0	0
60.0	115	7720	1509	0	0

Table 3.1(b) : *Peak to peak height data as a function of sputter time of a 5 minute 290°C annealed sample.*

Sputter Time (min)	Nickel Ni (848,.27)	Silicon Si (92,.36)	Silicon Si (1619,02)	Oxygen O (512,.51)	Carbon C (272,.19)
0.0	7841	0	0	3998	8395
1.0	18736	0	0	0	596
3.0	18358	0	0	195	100
4.0	17920	20	0	206	0
5.0	17632	0	0	162	0
7.0	17230	8	0	261	0
10.0	16316	0	0	225	0
15.0	15921	0	0	42	0
20.0	15580	0	0	0	0
25.0	15143	0	0	97	0
30.0	14752	1735	43	58	0
35.0	13723	5509	680	0	0
40.0	13632	6582	914	0	0
45.0	13219	6709	935	0	0
50.0	12149	7294	1033	0	0
55.0	8268	10564	1453	0	0
60.0	4088	14503	1924	0	0

69

Table 3.2 : *Atomic percentage of Ni and Si in a virgin sample and 5 minute 290°C annealed sample expressed as a function of sputter time.*

UNANEALEAD SAMPLE			SAMPLE ANNEALED AT 290°C FOR 5 MINUTES		
Sputter Time (min)	Nickel Ni (848,.27)	Silicon Si (1619,.02)	Sputter Time (min)	Nickel Ni (848,.27)	Silicon Si (1619.,02)
0.0	100.0	0.0	0.0	100.0	0.0
1.0	100.0	0.0	1.0	100.0	0.0
2.0	100.0	0.0	2.0	100.0	0.0
3.0	100.0	0.0	3.0	100.0	0.0
4.0	100.0	0.0	4.0	100.0	0.0
5.0	100.0	0.0	5.0	100.0	0.0
7.0	100.0	0.0	7.0	100.0	0.0
10.0	100.0	0.0	10.0	100.0	0.0
15.0	100.0	0.0	15.0	100.0	0.0
20.0	100.0	0.0	20.0	100.0	0.0
25.0	100.0	0.0	25.0	100.0	0.0
30.0	100.0	0.0	30.0	96.2	3.8
35.0	100.0	0.0	35.0	59.9	40.1
40.0	100.0	0.0	40.0	52.5	47.5
45.0	26.3	73.7	45.0	51.2	48.8
50.0	9.8	90.2	50.0	46.6	53.4
55.0	2.5	97.5	55.0	29.7	70.3
60.0	0.6	99.4	60.0	13.6	86.4

It can be seen from table 3.1 that the deposited nickel layer in the virgin sample was about 210nm thick (since the sputtering rate was 3.5 nm per minute). This is consistent with the RBS measurement. After annealing at 290°C for 5 minutes about 20 nm of the original deposited nickel layer was consumed to form Ni_2Si. This also is consistent with the RBS results.

3.1.2 NiSi FORMATION

NiSi formation was studied at 330°C and 350°C. After 20 minutes of annealing at 330°C, all the Ni-metal has been consumed (as portrayed in figure 3.4(b)) to form both Ni_2Si and NiSi. RBS shows these two layers to be more or less of the same thickness. After 30 minutes of annealing it can be seen in figure 3.4(c) that more $NiSi_2$ has been consumed by the NiSi leaving only a thin layer of $NiSi_2$ on the surface. The RBS spectrum for a sample annealed at 350°C for 10 minutes (figure 3.4(d)) suggests that even a thinner layer of $NiSi_2$ is left on the surface with the bulk of the silicide being NiSi. Layered growth for NiSi formation is confirmed by the cross-sectional TEM micrograph in figure 3.5(b) .
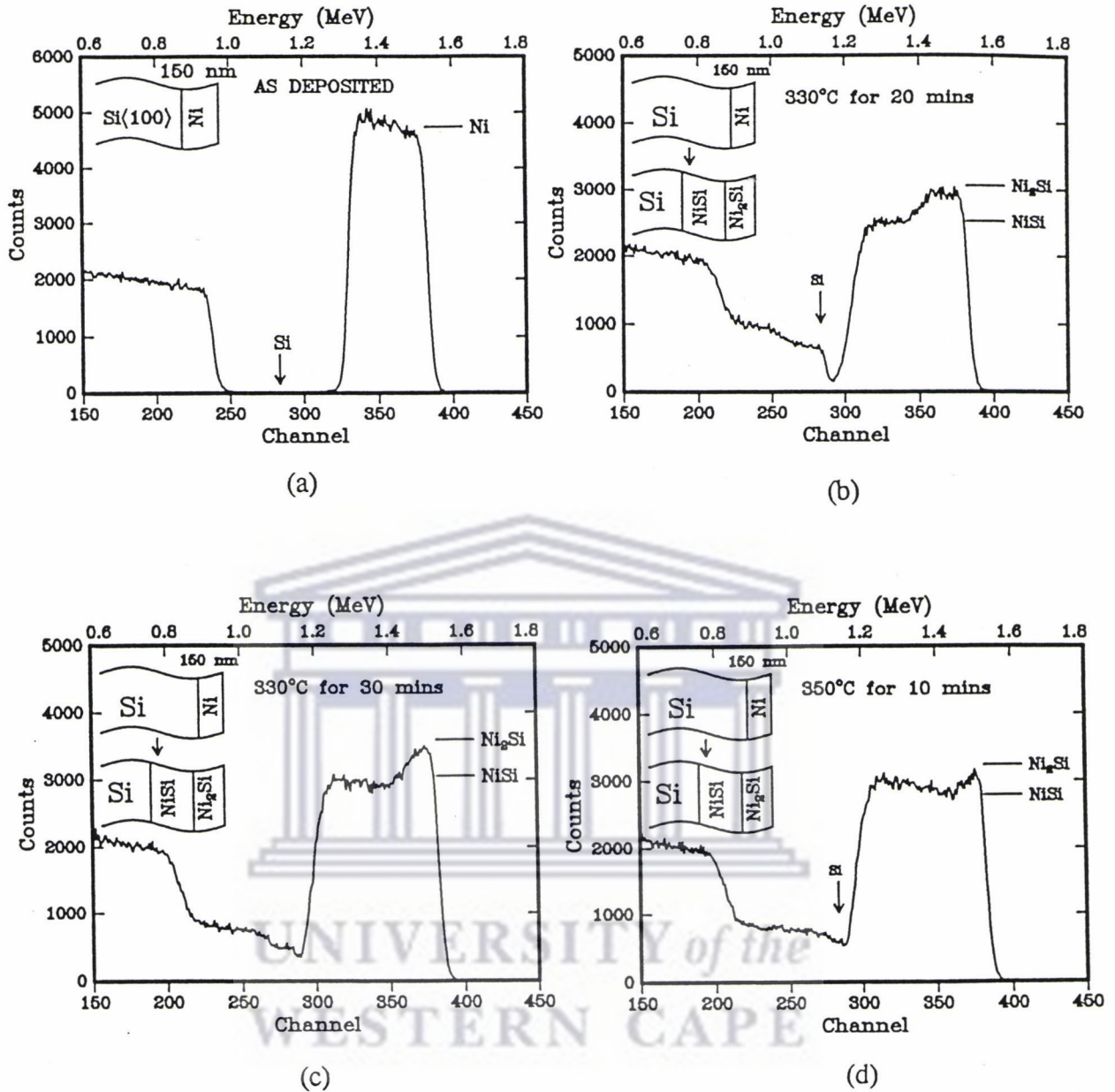
70

Figure 3.4 : *RBS spectra showing NiSi formation (a) is a spectrum of the as-deposited layer, (b) a spectrum of a sample annealed at 330°C for 20 minutes, (c) a spectrum of a sample annealed at 330°C for 30 minutes and (d) a spectrum of a sample annealed at 350°C for 10 minutes.*

It can be seen, however, that NiSi has started to grow on the Si-silicide interface resulting in grains of varying sizes. These NiSi grains have been reported to assume an orthorhombic crystal structure [d'H-84]. It is apparent in figure 3.5(a) that the interface between the Ni_2Si

71

and NiSi layers is rather irregular with the Ni$_2$Si layer having a thickness variation. Note the difference in grain size as well as the polycrystalline nature of this phase. Owing to the lack of uniformity and regularity of the Ni$_2$Si-NiSi interface as portrayed in figure 3.5 (and in contrast to figure 3.2(a)), RBS shows a gradual drop in the Ni signal Ni$_2$Si (figures 33.4(b),(c) and (d)), in contrast to figure 3.1(b) where a sudden drop in the Ni signal has been encountered. Owing to the non-uniformity in thickness of the two phases present

(a)

(b)
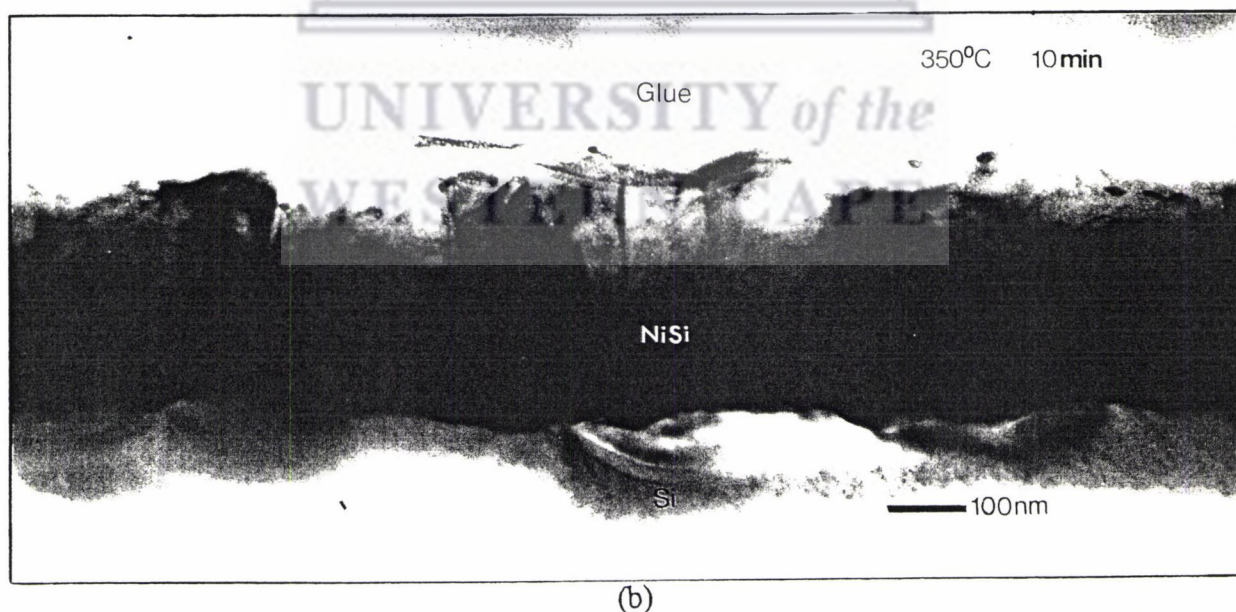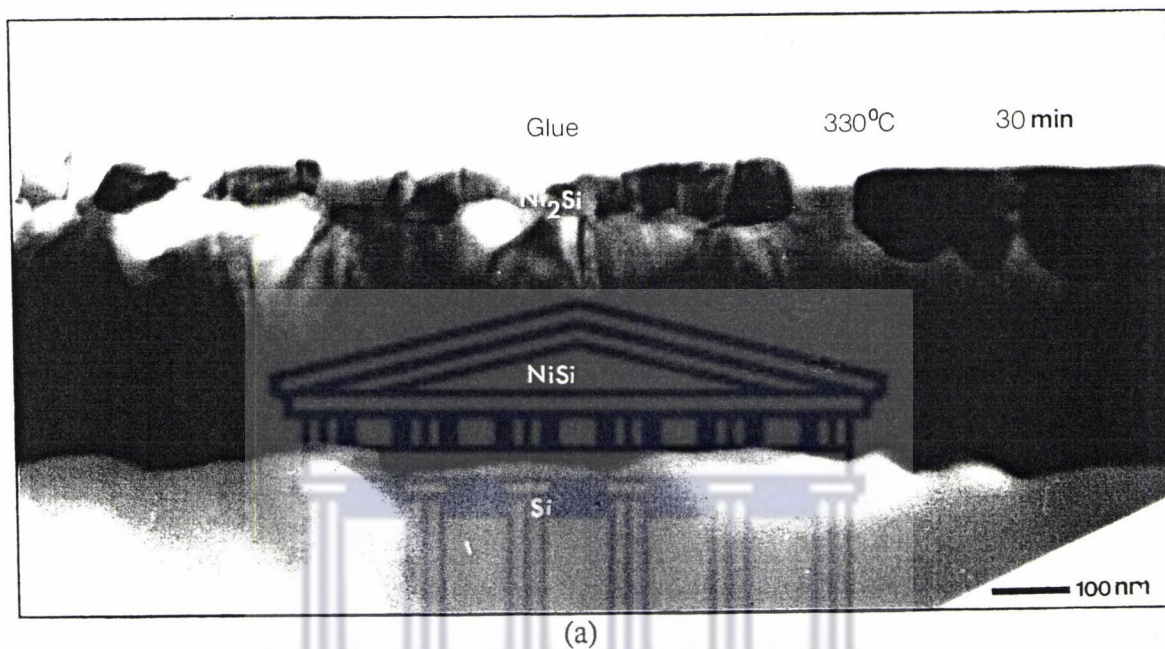
Figure 3.5 : *Bright field cross-sectional TEM image of a sample annealed at (a) 330°C, for 30 minutes and (b) 350°C for 10 minutes.*

72

in the 330°C annealed samples, depth profiling using AUGER only gives a reflection of the average thickness of the different silicide layers due to the size of the electron probe relative to that of the specimen. AUGER is however, useful in detecting especially light element impurities and indeed oxygen and carbon has once again been detected. The specimen contamination most probably occurred in the evaporation system and in the vacuum furnace. The Si-NiSi interface however, is less irregular (figure 3.5) than the Ni_2Si-NiSi interface. This is also reflected in the RBS spectra (figure 3.4). Figure 3.4(d) and the corresponding micrograph in figure 3.5(b) is the RBS spectrum and corresponding TEM bright field image respectively of a sample annealed at 350°C for 10 minutes. RBS shows a trace of Ni_2Si still present with the bulk of the silicide being transformed into NiSi. It can actually be seen in the micrograph (figure 3.5(b)) that some of the well formed orthorhombic NiSi grains have not completely grown through the full silicide thickness yet. Once all the Ni_2Si has been consumed to give way for the NiSi grains to grow through the entire silicide thickness, lateral growth takes place, some grains growing at the expense of others. Many smaller NiSi crystallites of random orientation are found close to the Si-silicide interface. These are all scattered between the larger crystals. This phenomenum is reflected in the microdiffraction pattern in figure 3.6 . In this diffraction pattern the regular array of spots suggest that one


Figure 3.6 : *Microdiffraction pattern of a sample annealed at 350°C for 10 minutes showing strong diffraction by a large crystal with one of its zone axes aligned parallel to the electron beam and showing the simultaneous presence of smaller crystallites which are randomly orientated.*

of the large crystals has been tilted so that the electron beam was virtually aligned with a particular zone axis thereby causing strong diffraction as reflected in the intensity of the spots. The ring structure in the pattern reflects the polycrystalline nature of the smaller crystallites.

73

Since larger crystals grow at the expense of the smaller crystallites, a stage is reached when they also grow at the expense of other large crystals. An example of a fully fledged NiSi layer with large grains of different orientations and with well formed grain boundaries is given in figure 3.7. The corresponding RBS spectrum of this sample which has been annealed at 550°C for 30 minutes is also provided (figure 3.7(b)).
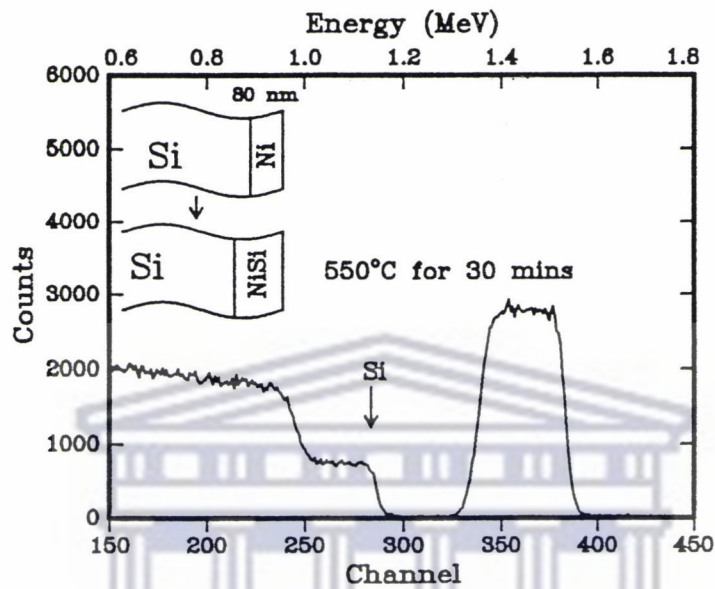
(a)
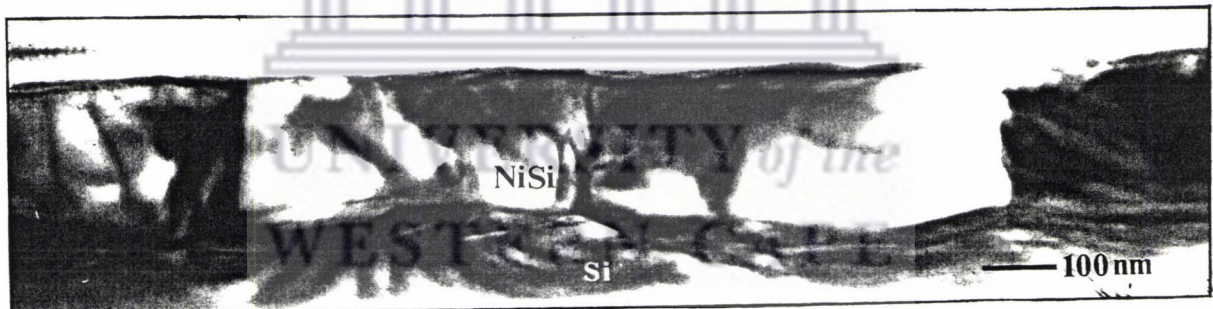
(b)

Figure 3.7 : (a) RBS spectrum and (b) corresponding TEM micrograph of a sample annealed at 550°C for 30 minutes showing large, well formed polycrystalline NiSi grains.

3.1.3 NiSi$_2$ formation

Up to now it was interesting to see how a fully fledged NiSi layer envolved from initial Si and Ni interaction. In contrast to the layered growth observed for both Ni$_2$Si and NiSi

74

formation, a completely different growth mechanism has been observed for NiSi$_2$ formation.

The NiSi phase was found to be stable up to about 700°C. At about 750°C, NiSi react with the silicon substrate to form NiSi$_2$. As mentioned in chapter 1, NiSi$_2$ has a cubic CaF$_2$ structure with a$_o$ equal to 0.5406 nm which is a good match for epitaxy with the diamond cubic structure of silicon with a$_o$ equal to 0.5428 nm. Initial NiSi$_2$ formation was investigated at an annealing temperature of 750°C at different annealing times. The backscattering results in figure 3.8 obtained for samples treated at this temperature for increasing annealing times is of much interest. It can be seen (by measuring height ratios) that the monosilicide
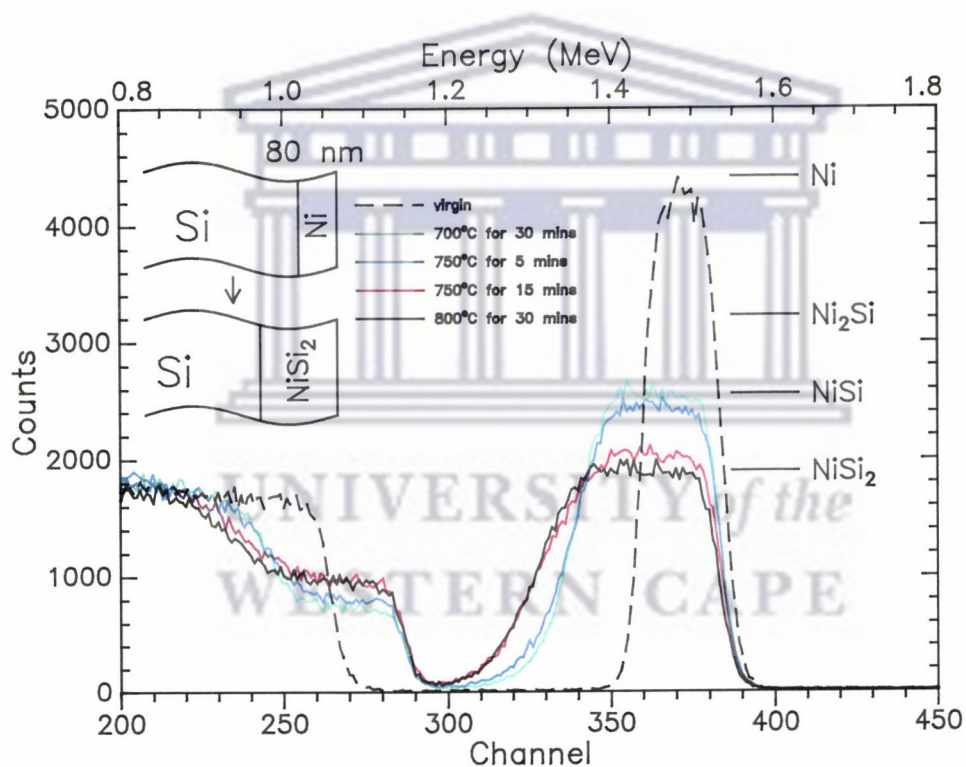

Figure 3.8 : *Backscattering spectra for Ni films on Si showing the virgin unannealed sample, the formation of NiSi at 700°C and the formation of NiSi$_2$ at 750°C and 800°C. All heat treatments were carried out for 30 minutes except at 750°C where annealing times were for 5 minutes and 15 minutes respectively.*

75

which was formed completely after a 30 minute anneal at 700°C is very similar to that obtained in figure 3.7(a). However, a 30 minute anneal at 800°C produces the disilicide, $NiSi_2$. After an anneal at the intermediate temperature of 750°C and different annealing times, one does not find the expected layered transition from NiSi at the free surface, to $NiSi_2$ at the Si interface. Instead the film appears to have transformed through its whole thickness to an intermediate composition thereby forming a phase which does not exist in the phase diagram (see section 1.7.4). The illusion is caused by the relatively large area of the probing beam of He ions which averages simultaneous composition profiles from an area (or areas) of pure NiSi and also from an adjoining area (or areas) of pure $NiSi_2$, resulting in the misleading appearance of the spectrum. The backscattering results in Figure 3.8 require that there should be no significant concentration gradients in either the NiSi phase or in the $NiSi_2$ phase through the thickness of the silicide film, in a direction normal to the surface. This investigation shows an irregularity at the silicide-Si interface. The $NiSi_2$ layer formed after annealing at 800°C for 30 minutes is characterized by a non-uniform thickness caused by faceting as demonstrated in figure 3.9. These facets can extend for several tens of nanometers into the Si substrate as seen in figure 3.9(c). However, areas of uniform thickness which extend over several micrometers does exist (figure 3.9(b)). This observation is consistent with that by Foel [Fo-79] who also used cross-sectional transmission electron microscopy to study the $NiSi_2$-Si interface. He found that the epitaxial layers grown on Si (100) substrates were growing in steps of flat terrains. The steps of these terrains were found to be defined by the (111) and (100) planes of the $NiSi_2$ epitaxial layer as illustrated in figure 3.10 . This type of growth morphology is consistent with Lau and Cheung's [La-80] view of a corrugated interface in which they speculate that the corrugation could be a result of nucleation -controlled formation of $NiSi_2$. Phase formation by a nucleation controlled mechanism takes place in a sudden way over a very narrow temperature range once nucleation starts. According to Lau and Cheung [La-80] the formation of $NiSi_2$ appears to follow such characteristics. They suggest that grains of $NiSi_2$ are initially nucleated at different sites at the NiSi-Si interface which is observed to be flat. Once nucleated, the grains grow normal to the interface, penetrating into the NiSi layer and the silicon substrate. The $NiSi_2$ grains initially grow as islands in a NiSi layer and grow into the silicon substrate. Since growth of these grains is a fast process these grains then grow laterally into the NiSi layer, with nickel as the dominant diffusing species.

76

If the lateral growth rate is much faster than the nucleation rate at the remaining unreacted NiSi-Si interface, the grains will grow until impingement, thus leading to a relatively flat NiSi$_2$-Si interface between the initial nucleation sites where the grains protrude into the silicon
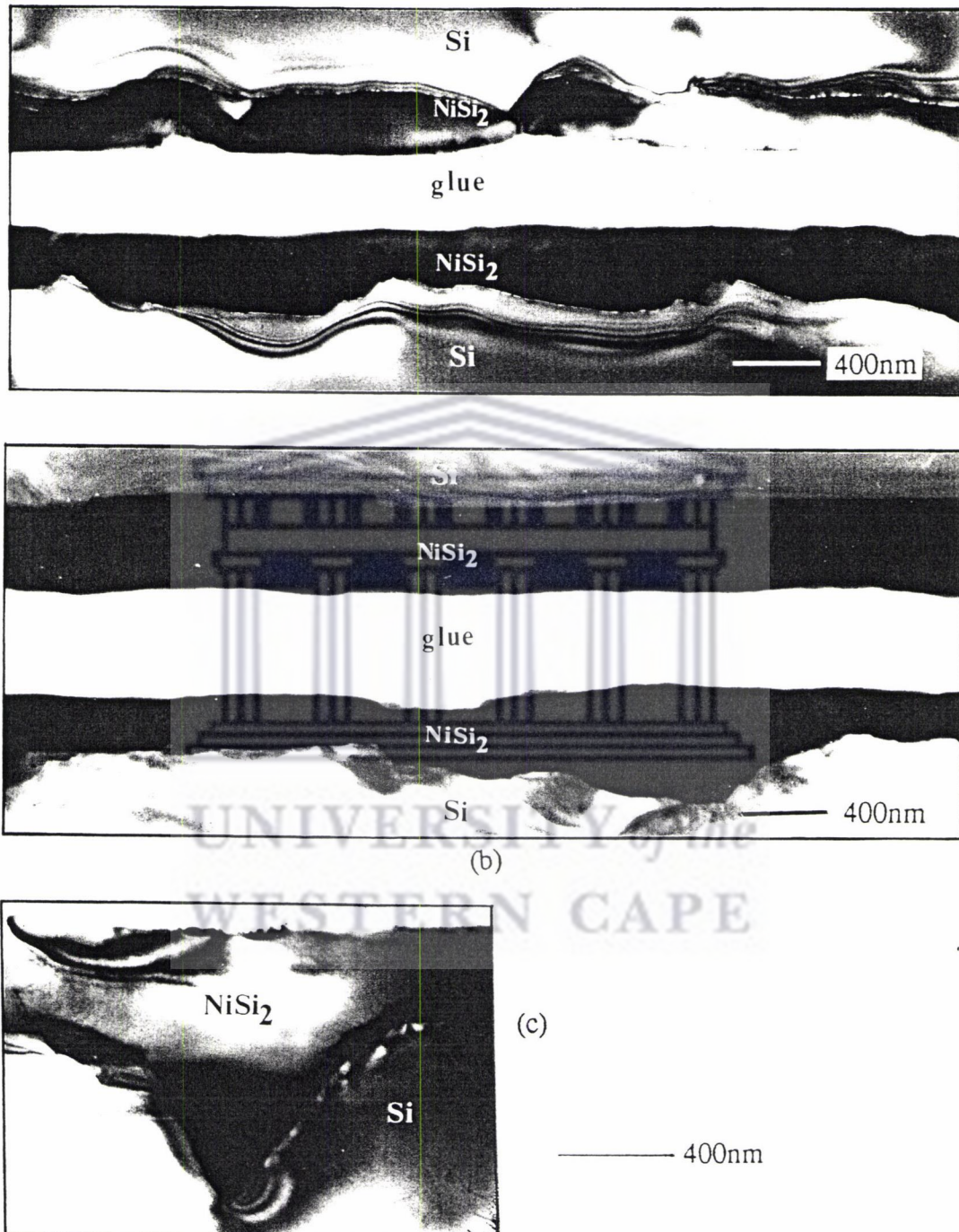

Figure 3.9 : Cross-sectional TEM bright field image of a sample annealed at 800°C for 30 minutes showing various kinds of silicide morphology. (a) irregular and non-uniform layers, (b) an uniform and non uniform layer and (c) severe faceting.
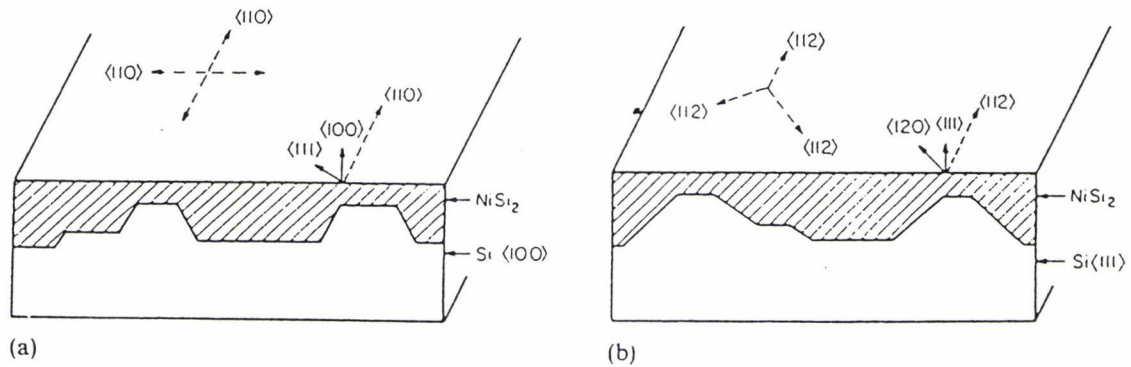
Figure 3.10 : *Schematic diagrams showing the step-like morphology of epitaxial NiSi₂ on (a)Si(100) and (b) Si (111) surfaces.*

substrate. This type of silicide formation process usually leads to a jagged interface, as shown schematically in figure 3.11.
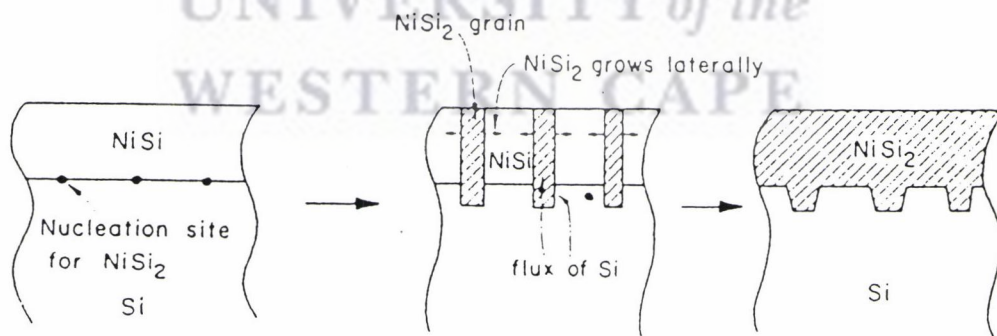

Figure 3.11 : *Schematic diagrams showing the NiSi₂ formation process leading to a jagged interface.*

They further suggest that during the epitaxial alignment of the NiSi₂ grains the jagged

interface takes the form of steps of flat terrains to minimize the surface energy. The corrugated interface (figure 3.10(a) and 3.10(b)) therefore is a consequence of local initiation of the NiSi$_2$ phase and surface energy minimization of the epitaxial layer.

Since NiSi$_2$ is known to grow epitaxially onto the Si substrate to form a single crystal layer, one can easily distinguish this phase from the NiSi phase. By tilting the specimen so that a set of crystal planes of the silicide layer of interest makes an angle, Θ, with the electron beam which satisfies the Bragg relation,

$$\lambda = 2dSin\Theta,$$

the single crystal nature of that particular layer (or part of that layer) is exposed by visually observing the diffraction contours running continuously across it. An example of this phenomenom is illustrated in figure 3.12 in which a bright field cross-sectional TEM image of a sample annealed at 750°C for 20 minutes in given. The bottom layer in figure 3.12(a) is clearly a single crystal. The same effect can be obtained for the top layer by tilting the specimen slightly. This is demonstrated in figure 3.12(b). In fact what one generally finds is reflected in figure 3.12(c) in which a low magnification micrograph of a relatively large area is given. Grains of different orientations (probably polycrystalline NiSi) and a film of a single crystal nature are observed. Grain boundaries are well defined and faceting seem to occur at random (probably influenced by certain levels of contamination on the Si-silicide interface). More bright field cross-sectional TEM micrographs of a sample annealed at 800°C for 30 minutes, are presented in figure 3.13. A homogeneous NiSi$_2$ layer is expected for this treatment. The layer in figure 3.13(a) is clearly single crystal in spite of a corrugated NiSi$_2$ - Si interface. The diffraction contours actually follow the profile of the interface. Figure 3.13(b) shows immense stress in the vicinity of the interface. This is probably caused by lattice mismatching. The lattice constants for NiSi$_2$ and silicon at room temperature are 0.5406 nm and 0.5428 nm respectively. Thus the NiSi$_2$ layer will be under compressive stress at 800°C with lattice constants for NiSi$_2$ and silicon of 0.548 nm and 0.544 nm respectively. When cooled to room temperature the NiSi$_2$ layer will therefore be under a state of tension. These stresses which result from the differences in lattice constants can probably cause fracture in the NiSi$_2$ layer. It is speculated that these stresses could have caused the fracture and folding seen in the NiSi$_2$ layer in figures 3.13(c) and (d) respectively.
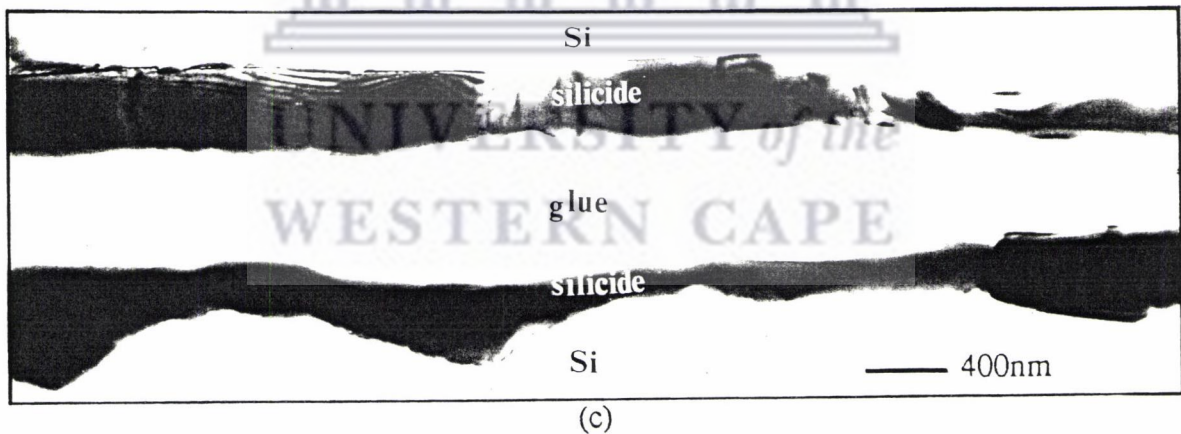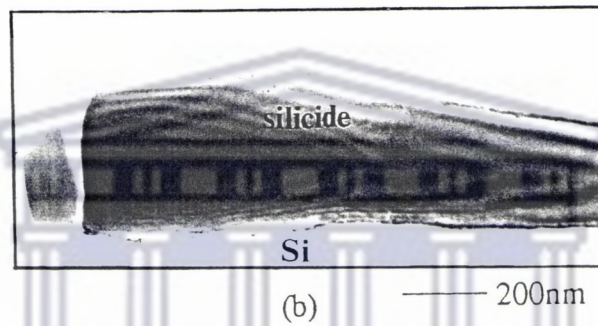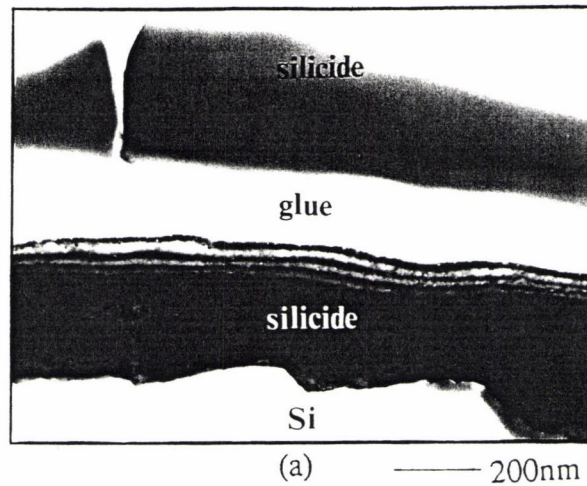
79

(a) ———— 200nm

(b) ———— 200nm

(c)

Figure 3.12 : *Bright field cross-sectional TEM images of a sample annealed at 750°C for 20 minutes. (a) Micrograph showing both silicide layers separated by a layer of glue. The diffraction contours in the bottom layer reflect its single crystal nature. (b) The effect of tilt on the top layer in (a) is demonstrated. (c) A more global view at low magnification.*
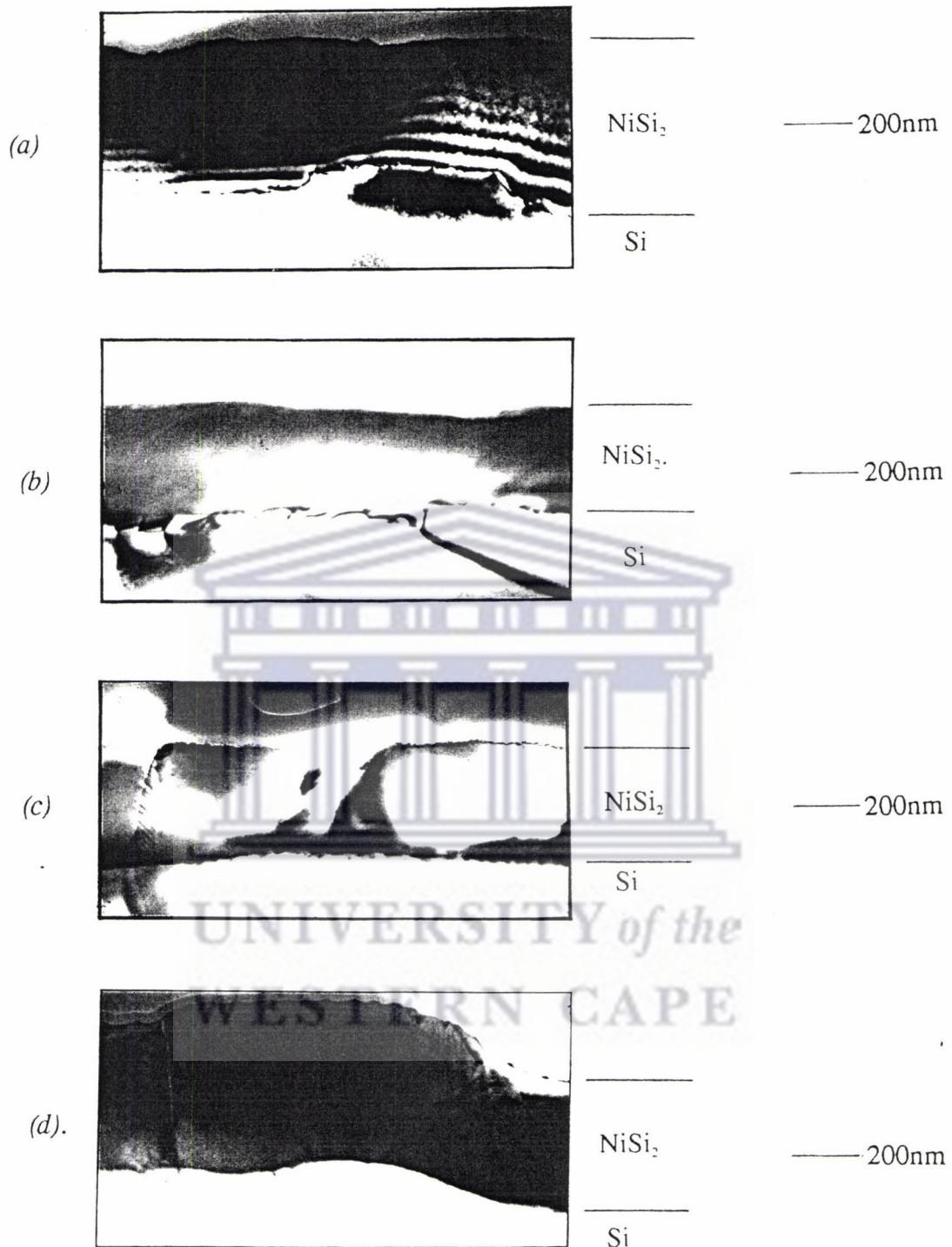
Figure 3.13 : Brightfield cross-sectional TEM images of a sample annealed at 800°C for 30 minutes to form NiSi₂. (a) Some epitaxy in spite of a corrugated Si-NiSi₂ interface is shown. (b) The presence of stress probably resulting from lattice mismatch is shown. Fracture speculated to be caused by stress is demonstrated in (c) and (d).

81

3.2 SUMMARY

Ni_2Si was formed at 290°C after 5 minutes of annealing. Only a small proportion of the Ni-metal was consumed. The Ni_2Si phase grew in layers and was of uniform thickness and both the Si-silicide and silicide-Ni interfaces were sharp. This phase is polycrystalline and lateral grain growth takes place until all the Ni-metal has been consumed.

NiSi formation was initially studied at 330°C. NiSi only forms once all the Ni-metal has been consumed i.e. when the Ni_2Si grows to its full thickness. This phase also forms via layered growth and is polycrystalline. Once all the Ni_2Si has been consumed some NiSi grains grow at the expence of others resulting in lateral growth.

$NiSi_2$ formation was studied at 750°C which is the transition temperature at which NiSi transform to the end phase. Layered growth is absent during $NiSi_2$ growth. $NiSi_2$ seem to grow as islands in a NiSi matrix. This phase grows epitaxially onto the Si(100) substrate but is characterised by faceting, folding and fracturing.

The transition from NiSi to $NiSi_2$ is dealt with in greater detail in Chapter 4.

CHAPTER 4

THE TRANSITION FROM NiSi TO NiSi$_2$

4.1 EXPERIMENTAL RESULTS

In this chapter a step by step investigation of the growth mechanism of the interesting transition process in which NiSi is transformed to NiSi$_2$, is pursued, with the use of RBS and an in depth TEM and SEM study together with AUGER and XRD.

4.1.1 A RBS study and channeling

In chapter 3 we have already commented on the misleading appearance of the spectra of intermediate temperatures and times during the transition process from NiSi to NiSi$_2$ (figure 3.8). It was suggested that the illusion is caused by the relatively large area of the probing beam of He ions which averages simultaneous composition profiles from an area (or areas) of pure NiSi and also from an adjoining area (or areas) of pure NiSi$_2$. The spectrum of a sample annealed at 750°C for 5 minute very closely represents that of a sample annealed at 700°C for 30 minutes which consist of a homogeneous layer of NiSi. This means that in a 5-minute 750°C annealed sample, some of the silicide is NiSi$_2$ with the rest still NiSi. Slightly longer annealing times will result in more and more conversion from NiSi to NiSi$_2$. The spectrum for a sample annealed at 750°C for 15 minutes (Figure 3.8) shows that most of the NiSi has already been transformed to NiSi$_2$. This is confirmed by XRD (see section 4.1.5). One would therefore expect some degree of epitaxy since NiSi$_2$ is known to grow epitaxially on Si (100) substrates. Channelling results for various vacuum furnace annealed structures formed by electron gun evaporation is given in figure 4.1. The spectra of the samples obtained along a random direction are denoted with a solid line. When these samples were aligned along a crystal plane, an appreciable decrease in the yields throughout the sample was encountered, indicating that a fair amount of crystal growth has taken place. These results further prove the existence of some degree of epitaxy as expected. The channelling results of a sample annealed at 750°C .
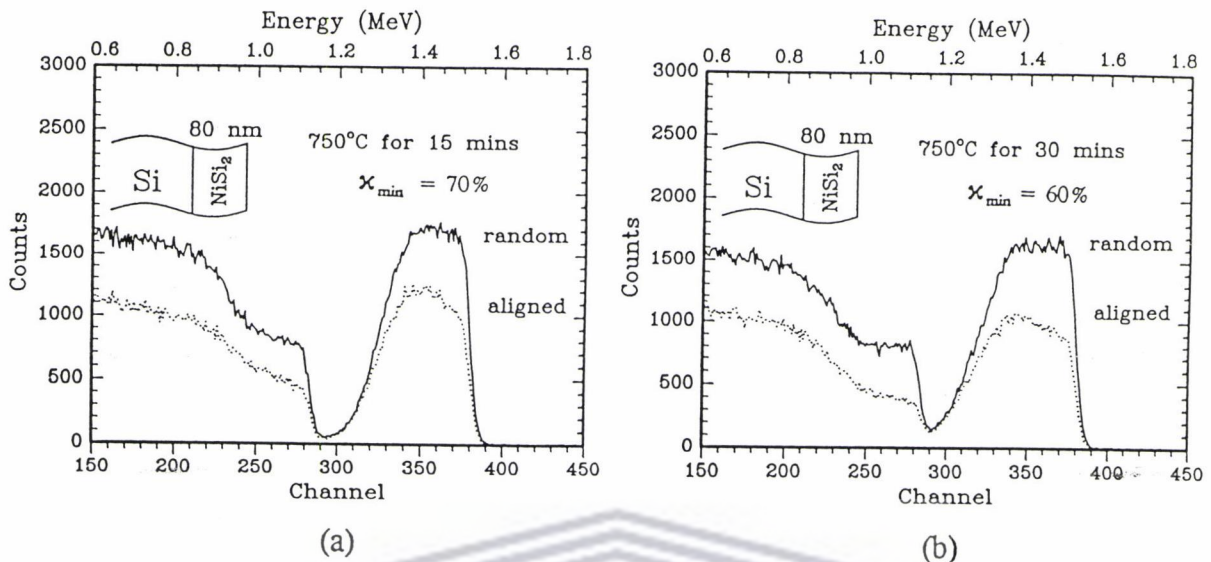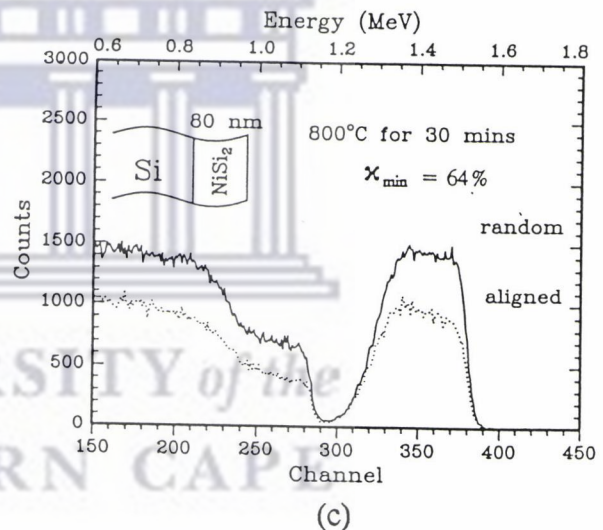
83

Figure 4.1 : *Channelling results for samples annealed at (a) 750°C for 15 minutes, (b) 750°C for 30 minutes, (c) 800°C for 30 minutes. The RBS spectra obtained along a random crystal orientation are drawn with a solid line. The decrease in the yields of Si and Ni in the aligned spectra compared to that in the random spectra, indicate a significant amount of epitaxial growth.*

for 15 minutes is given in figure 4.1(a). The channelling minimum yield χ_{min} (which is equivalent to the aligned yield divided by the random yield) in this case is 70%. After 30 minutes of annealing at the same temperature the value of χ_{min} is approximately 60%. The channelling results of this sample is provided in figure 4.1(b). This result is consistent with our expectations since more NiSi to $NiSi_2$ conversion has taken place. The value of χ_{min} would therefore decrease, a smaller χ_{min} value reflecting better crystalline perfection. However, when observing the channelling results of a sample which has been annealed at 800°C for 30 minutes (figure 4.1(c)), we obtain a χ_{min} value of 64%. This result is unexpected when taking the single crystal nature of $NiSi_2$ as described in Section 3.3, into

84

consideration. After all, RBS does show this sample to be a virtually homogeneous layer.

An explanation for the above contradicting result could lie in the immense faceting which occur for $NiSi_2$ growth on Si (100) as we have come across in section 3.3 (see figure 3.8). Faceting is a phenomenon whereby crystal structure alignment between the growing silicide and underlying Si takes place along common crystallographic planes resulting in a sharing of atoms along these planes. These faceting occurrences on the Si-silicide interface are reflected in the tailed off edge of the Ni signal (in the silicide) into the silicon substrate as reflected in the RBS spectra in figure 4.1. Another reason for the (relatively high) χ_{min} value for the 30 minute-800°C annealed sample is the difference in lattice constants between $NiSi_2$ and Si which cause stresses which in turn cause fracture in the $NiSi_2$ layer as well as some degree of damage in the underlying silicon. For thin $NiSi_2$ layers lattice mismatch can be accommodated by elastic straining within the $NiSi_2$ layer but the strain is not expected to have a uniform distribution across the layer. This leads to increased χ_{min} values because of dechanneling by the strained lattice. For thicker $NiSi_2$ layers (300nm or more) the strain energy can no longer be taken up by elastic strain alone. Misfit dislocations are therefore generated at a critical thickness. Fracture can also take place to relax the misfit strain (see figure 3.13(c) & (d)). In fact from this study it appears that fracturing is a more energetically favourable mode of relaxation. The fact that the silicide is virtually a single crystal makes it particularly difficult to relax its stress through mechanisms such as grain boundary sliding. In a well developed network such as a thin film single crystal $NiSi_2$, fracture does tend to result readily. A further explanation for the bad channeling results could lie in the occurrence of differently oriented $NiSi_2$ grains with respect to the rest of the $NiSi_2$ layer (which happens to be single crystal). This phenomenon can be observed in figure 4.8 in section 4.1.2.

4.1.2 A TEM study

As starting point we use figure 3.7 in which the RBS spectrum and corresponding TEM bright field image of a sample annealed at 550°C for 30 minutes is given (see also figures 4.3 and 4.20). In this sample lateral grain growth of NiSi up to 300 nm in diameter has been encountered. A silicide thickness of not more than 200 nm has been measured.

In a sample (with approximately the same Ni deposition thickness) annealed at 750°C for only 5 minutes the situation is slightly different. The RBS spectrum of this sample and three cross-sectional TEM bright field images of different areas in this sample are given in figure 4.2. However, to appreciate these micrographs and for the sake of possible artifacts which may arise, one needs to look at a virgin sample first. The virgin sample on which approximately 100 nm of Ni has been deposited onto a silicon substrate, together with its corresponding RBS spectrum is therefore also provided. In figure 4.2(b) the polycrystalline nature of the deposited Ni layer is clearly observed. The interface between the Ni layer and silicon substrate is sharp and the layer is uniform in thickness. It is not always possible to obtain a specimen in which a pure metal layer is electron transparent while still having silicon present in the immediate vicinity since the Ni-metal offers more resistance to atom milling than what Si and glue (which normally consists of light elements) offers. This evenly eroded specimen can only result from an optimal angle of ion bombardment coupled with the right high voltage and current in the guns of the atom mill.

Figures 4.2(c) and (d) in which different areas of the 5 minute 750°C annealed sample are portrayed, are of much interest. Note that an illusion is created in Figure 4.2 (c) of the presence of another layer on the top half of the silicide adjacent to the glue. This is caused by the glue layer which has curled over onto the silicide. If one compares this sample with that in figure 3.7, one observes a definite increase in grain size to a maximum of 500 nm and silicide thickness to a maximum of about 300 nm. Further grain growth has taken place at the expense of other grains resulting in grains which are twice as large than others. This is especially seen in Figure 4.2(d). The grain boundaries in all three these micrographs are clearly very well defined. Note also the regular undulating silicide-silicon interface. This creates the impression of the grain boundaries being pinned for a relatively long time allowing each grain to bulge outward into the underlying silicon. This effect is probably caused by lattice diffusion of Ni via a vacancy and/or intertitial mechanism into the open diamond structure of the silicon substrate. The volume of Ni during vacancy and interstitial diffusion exceed that of grain boundary diffusion by far, hence the bulging effect. The different orientations of the grains in this layer make the entire layer polycrystalline. Note the hard, resistant nature of the silicide being formed as reflected in the persistence of this layer under heavy ion bombardment (in the milling process) with the glue and silicon being eroded away

86

completely. By the looks of it, it seems as if this specimen is just a replica of the 30 minute 550°C annealed specimen in figure 3.7 in which a homogeneous NiSi layer is portrayed, the only major difference being the increase in grain size. However, microdiffraction proves this layer not to be homogeneous.
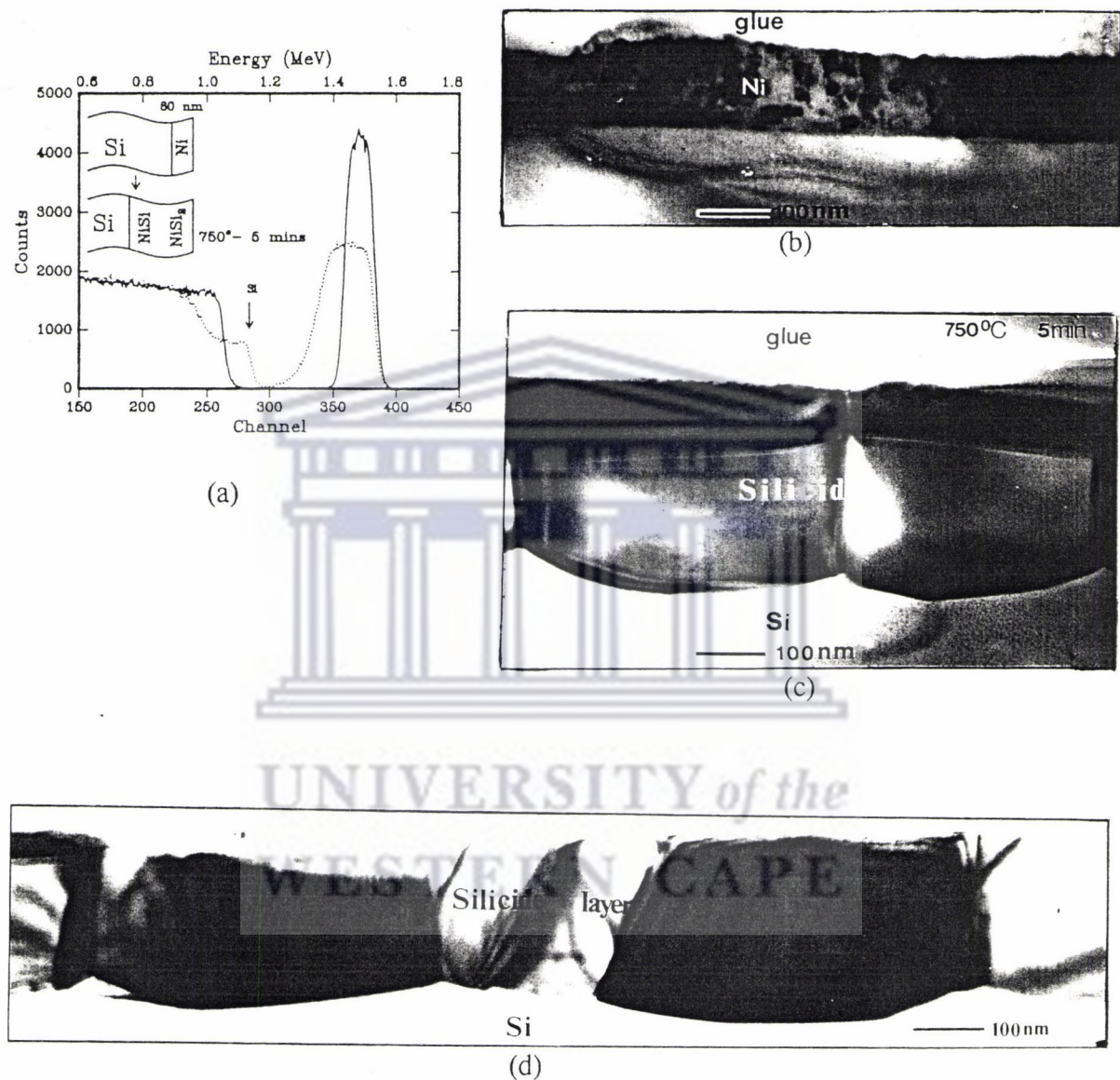

Figure 4.2 : *(a) RBS spectra of virgin and sample annealed at 750°C for 5 minutes and (b) Cross-sectional bright field TEM image of the virgin sample, (c) and (d) are bright field TEM images of different areas in the sample annealed at 750°C for 5 minutes.*

A microdiffraction analysis was done on a single grain in the cross-section of a sample

annealed at 550°C for 30 minutes which undoubtedly consists of a homogeneous NiSi layer. A micrograph of a sample annealed at 550°C for 30 minutes and corresponding microdiffraction pattern of a grain as indicated in figure 4.3 is provided.
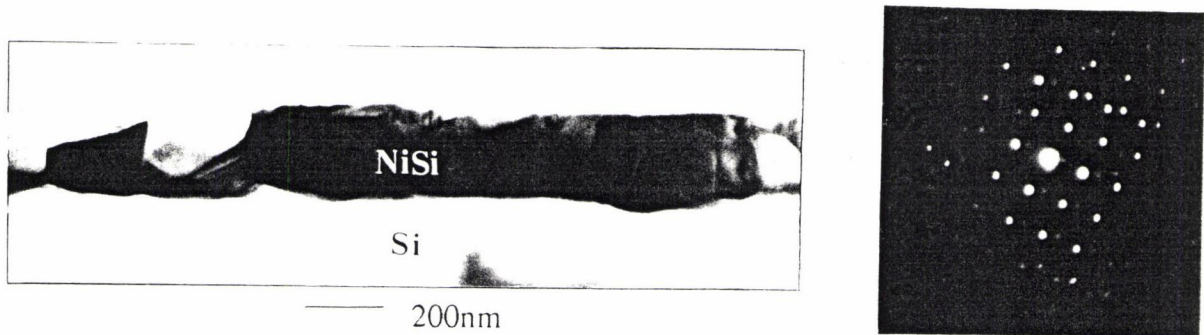

Figure 4.3 : *TEM micrograph and corresponding microdiffraction pattern of a grain in a sample annealed at 550°C for 30 minutes. The silicide is a homogeneous polycrystalline NiSi layer.*
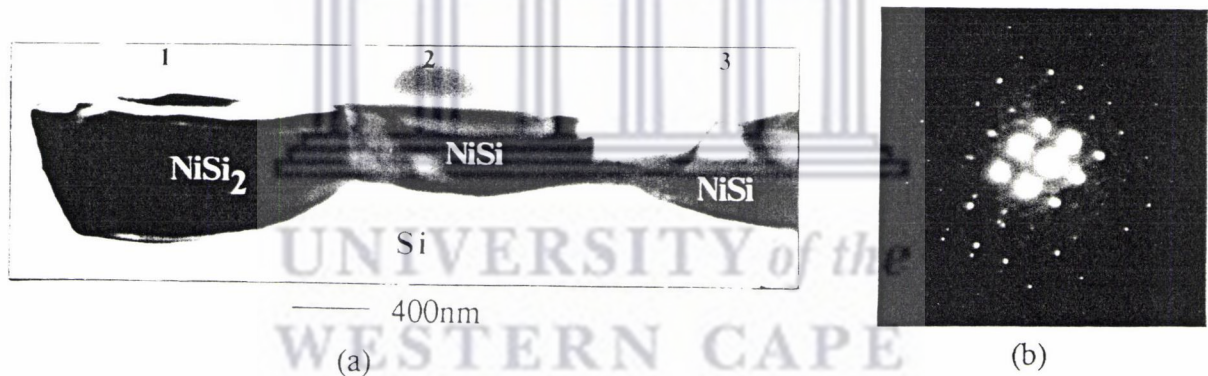

Figure 4.4 : *(a) TEM micrograph of a sample annealed at 750°C for 5 minute. The corresponding microdiffraction pattern of grain 3 is given in (b).*

Analysis of this diffraction pattern showed that the allowable reflections and corresponding d-values best suit those given for NiSi assuming the cubic FeSi crystal structure (see table 1.4 and figure 1.5). It was out of pure coincidence that for a sample annealed at 750°C for 5 minutes (figure 4.4) a similar diffraction pattern (figure 4.4(b)) was obtained for grain 3. An analysis confirmed this to be NiSi with a cubic FeSi structure.

88

Interesting enough, grain 2 in figure 4.4(a) was analysed to be NiSi assuming an orthorhombic crystal structure (see table 1.4 and figure 1.5). The microdiffraction pattern of grain 2 (of figure 4.4(a)) is given in figure 4.5. The extra bright spots are from a higher order lane zone from the underlying Si. A computer program showed this crystal to be orientated with the [001] zone axis parallel to the electron beam when the diffraction pattern was taken. This crystal structure for NiSi is known to exist at low temperatures (about $450°C$ and lower). After anealing for

Figure 4.5 *Microdiffraction pattern of grain 2 in figure 4.4 (a).*

such a short time (5 minutes) at $750°C$ it is reasonable to expect this crystal structure to exist since it is thought that NiSi initially crystallizes into an orthorhombic crystal structure before undergoing an allotropic transformation to a FeSi cubic structure.
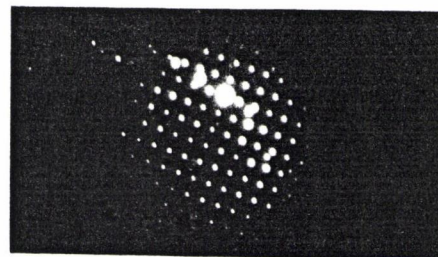
Microdiffraction proved grain 1 in figure 4.4(a) to be $NiSi_2$ assuming a rhombohedral crystal structure. The diffraction pattern of grain 1 (of figure 4.4(a)) is given in figure 4.6. This is a most interesting finding since it proves the co-existence of both NiSi and $NiSi_2$ in a sample annealed at $750°C$ for 5 minutes as expected. An EDAX analysis of the three grains in figure 4.4(a) also pointed toward the corresponding compositions (in atomic
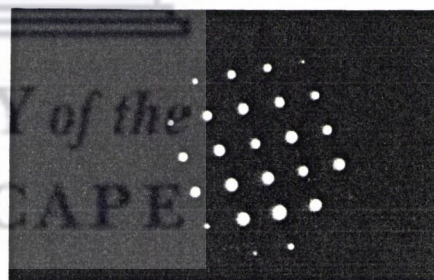

Figure 4.6 *Microdiffraction pattern of grain 1 in figure 4.4 (a).*

percent). In each case however an excess Si was detected. We speculate that this is due to lateral scattering into the Si substrate thereby causing fluorescent effects. The TEM micrograph of the sample in figure 4.4(a) shows that the crystal boundaries between the three grains remain well intact, creating the impression that individual grains as a whole undergo transformation to the next phase before disintegration of the original grain boundaries.

89

Figure 4.7 is a bright field cross-sectional TEM micrograph of a sample which was annealed at 750°C for 15 minutes (see figure 3.8 for RBS spectrum). Four different areas are marked on which microdiffraction analysis was done. The region marked A is single crystal Si. Figure 4.7 (b) is a [110] zone axis diffraction pattern of the silicon substrate. This [110] zone axis is expected since the cross-section of the sample (in which Si(100) was used) is under investigation. The region marked B was found by microdiffraction (figure 4.7 (c)) to be NiSi assuming a cubic FeSi structure (see table 1.4 and figure 1.5). Region C, of which a [110] zone axis diffraction pattern is given in figure 4.7 (d), was analysed to be $NiSi_2$. This is a classic example showing the nucleation of a $NiSi_2$ grain clearly differently orientated with resepct to the $NiSi_2$ in region D.
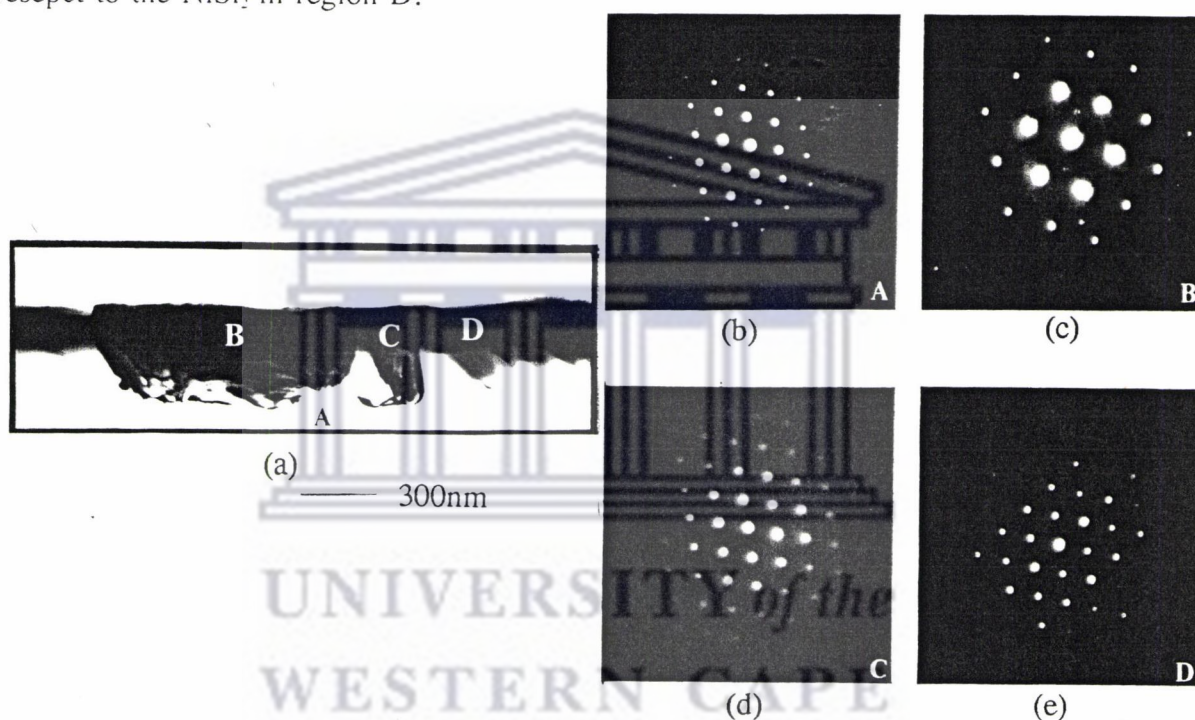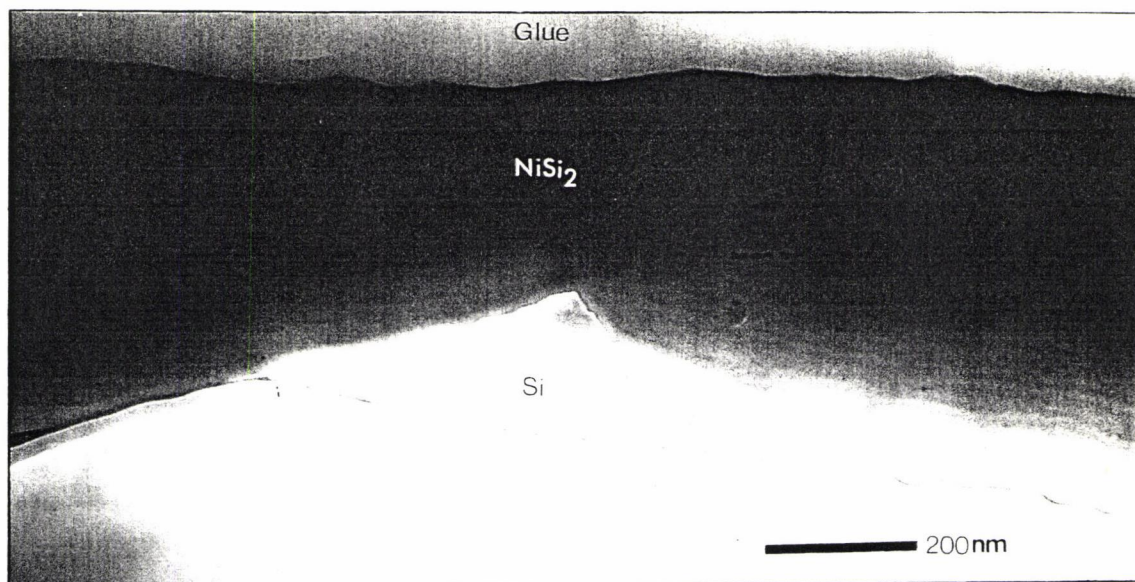

Figure 4.7 : *(a) Cross-sectional TEM Bright-field image of a silicide layer formed after annealing at 750°C for 15 minutes (b) A diffraction pattern of area A (Si). (c) A diffraction pattern of area B (NiSi). (d) A diffraction pattern of area C ($NiSi_2$). (e) A diffraction pattern of area D ($NiSi_2$).*

The RBS spectrum (see figure 4.1 (b)) of a sample which has been annealed at 750°C for 30 minutes shows that (by measuring height ratios) virtually all the NiSi has been transformed to $NiSi_2$. Different kinds of interesting morphologies of this $NiSi_2$ layer are presented in Figure 4.8 . Figure 4.8(a) seem to be a replica (on a larger scale) of figures 4.2 (c) and (d)

(a)

(b)

Figure 4.8 : *Cross-sectional TEM Bright-field images of a sample annealed at 750°C for 30 minutes. (a) An undulating morphology indicating that the grain boundary at the indent must have persisted for a relatively long time before disintegrating; (b) shows NiSi$_2$ grains of different orientation to the rest of the NiSi$_2$ layer. Note the persistent faceting on the silicon - silicide interface (bottom).*

Figure 4.9 : (a) *A Cross-sectional TEM bright field image of a sample annealed at 800°C for 30 minutes showing a uniform NiSi$_2$ layer on Si(100); (b) a [110] zone axis diffraction pattern of the Si substrate, (c) a [110] zone axis diffraction pattern of the NiSi$_2$ layer and (d) a [110] zone axis diffraction pattern taken across the Si-NiSi$_2$ interface, reflecting the epitaxial nature of NiSi$_2$ w.r.t. Si.*

91
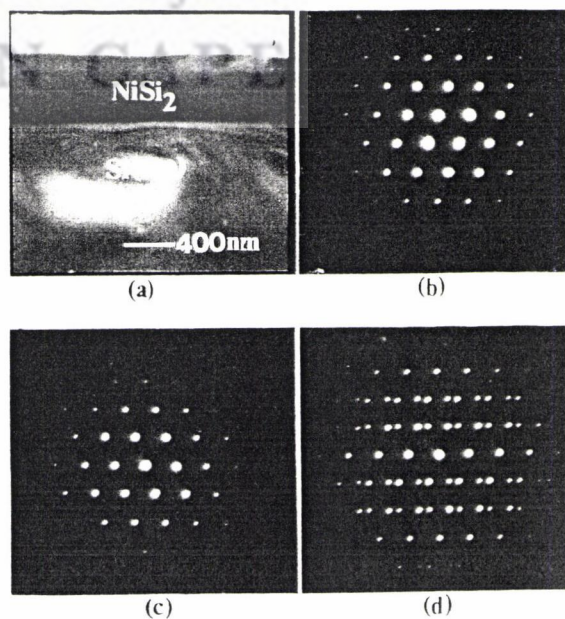
in which a wave-like undulating Si-silicide interface is presented. What has probably happened is that some grain boundaries in figure 4.2 (c) and (d) has disintegrated to form larger grains, some grain boundaries therefore remaining for a longer time than others. The indent in the silicide layer in figure 4.8 (a) shows that this must have been a location of a previously existing grain boundary; other grain boundaries has disintegrated prior to this one giving rise to much larger grains as reflected in the large undulation in silicide thickness. Figure 4.8 (b) show that some $NiSi_2$ grains are orientated differently to the other matrix $NiSi_2$ which has been found to be epitaxial w.r.t. Si. These differently orientated grains inhibit the single crystallinity of the $NiSi_2$ layer and cause dechanneling leading to higher χ_{min} values than expected (see figure 4.1 (b)).

An analysis of a sample which has been prepared by annealing at 800°C for 30 minutes shows it all to be $NiSi_2$. We have already commented on its single crystal nature in section 3.3. In spite of the corrugated Si-silicide interface which normally exist in this sample (see figures 3.9, 3.12 (a) and 3.12 (a)), areas of uniform $NiSi_2$ thickness does exist. An example of such an area is presented in figure 4.9 (a). Little contrast exist between the $NiSi_2$ layer and silicon substrate since epitaxial growth of the silicide (and therefore its similar crystal structure to that of Si) cause the electrons to be diffracted in the same way by both silicide and substrate. Figure 4.9 (b) is a [110] zone axis diffraction pattern of the silicon substrate and is expected to be single crystal as reflected in the regular array of spots. the single crystal nature of the $NiSi_2$ layer is reflected in figure 4.9(c) in which a [110] zone axis diffraction pattern is given. Figure 4.9(d) is also a [110] diffraction pattern of an area taken across the Si-$NiSi_2$ interface. The similar crystal orientation of Si and silicide is ultimately reflected in figure 4.9(d) in which some spots are common to both layers while others are slightly displaced relative to each other due to a small difference in orientation about the C-axis and difference in lattice constants.

The results in Figure 4.9 are what we normally strive for; a $NiSi_2$ layer of uniform thickness grown epitaxially onto the silicon substrate.

4.1.3 A SEM study

There exists enough evidence up to now (from sections 3.3, 4.1 and 4.2) that $NiSi_2$ already starts to form after annealing a sample at 750°C for 5 minutes. Figure 4.10 shows a secondary electron image of an as-deposited sample, a sample annealed at 550°C for 30 minutes, a sample annealed at 750°C for 5 minutes and its corresponding backscattered electron image.
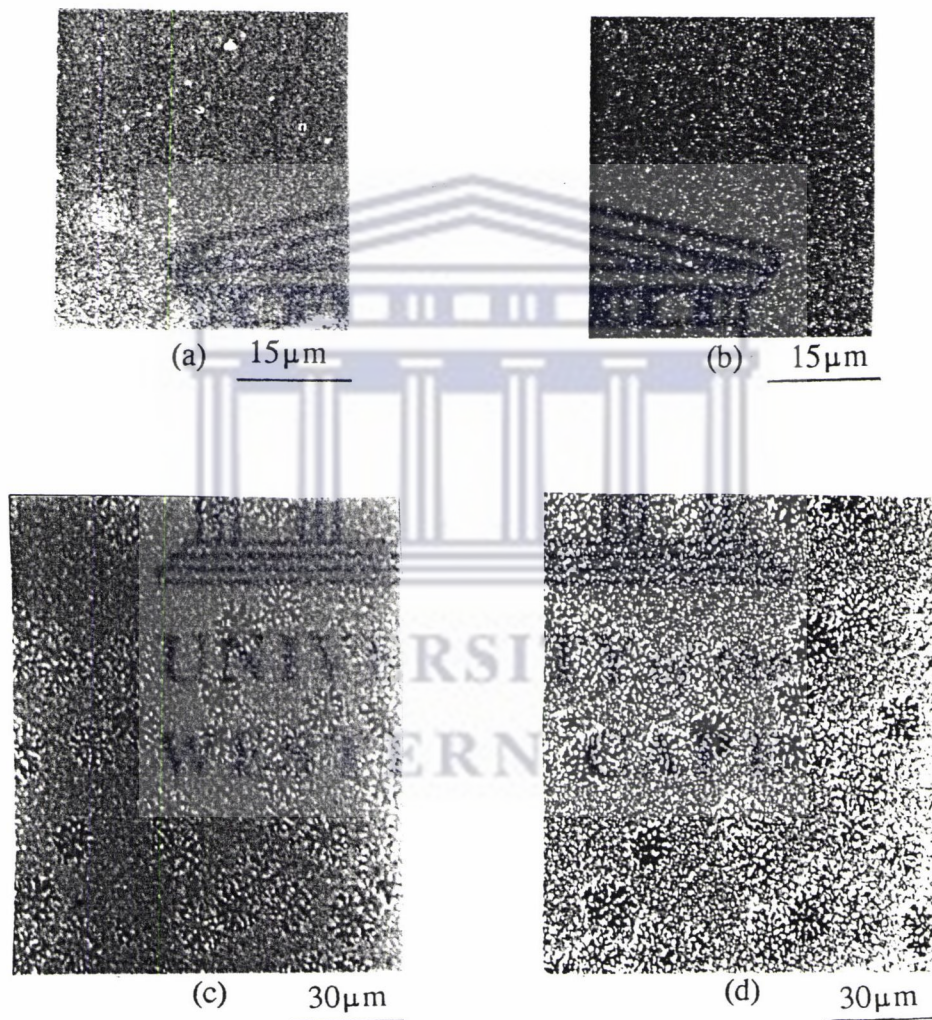

Figure 4.10 : *A secondary electron image of (a) an as-deposited sample (Ni on Si (100) (b) a sample annealed at 550°C for 30 minutes and (c) a sample annealed at 750°C for 5 minutes (NiSi and NiSi₂), (d) is a backscattered electron image of the same area on the sample in (c). All images were taken at 30 kV.*

Figure 4.10 (a) shows very little contrast because of the fine grained Ni-layer. Figure 4.10 (b) also does not show contrast because of the smoothness of the NiSi layer on the surface. In figure 4.10 (c) the initial formation of $NiSi_2$ (the lighter concentric areas) can clearly be seen. The contrast between these two phases depend critically on the angle of tilt towards or away from the backscattered electron detector. This effect can clearly be seen in figure 4.11 in which a backscattered electron image of the same sample is given. The "hole" in the centre of the micrograph was used as a reference to ensure the same field of view for both recordings. Figure 4.11(a) and (b) shows the effect on the $NiSi_2$ crystals when tilted towards and away from the backscattered electron detector respectively. The concentric fashion in which the $NiSi_2$ initially form creates the impression of dendritic growth in which favourably oriented dendrites develop into columnar grains. One such conglomeration of columnar grains which has grown through the entire thickness of the silicide layer is shown in figure 4.12. The columnar structure is clearly seen with good contrast existing between the tip, which generates excessive secondary electron emission due to its geometry, and the length which extends below the surface into the silicon substrate.
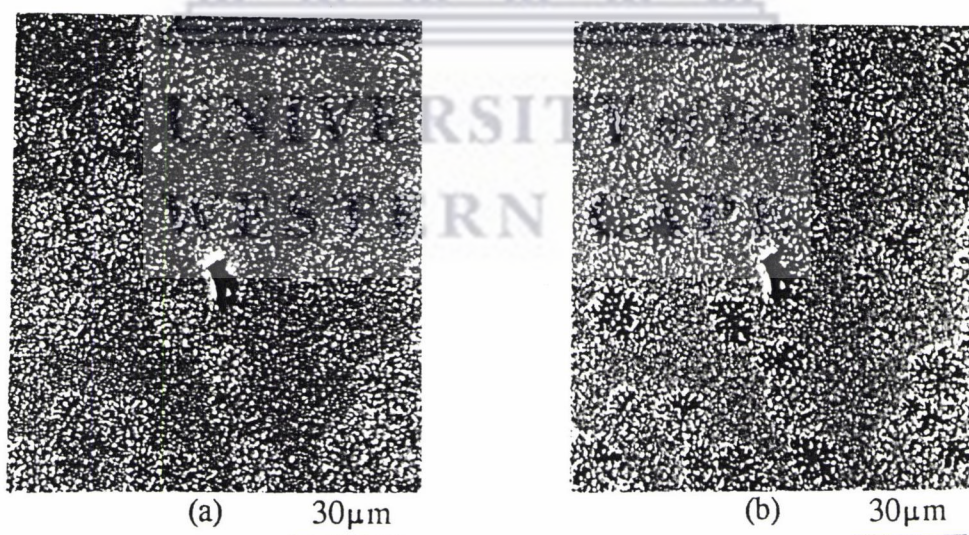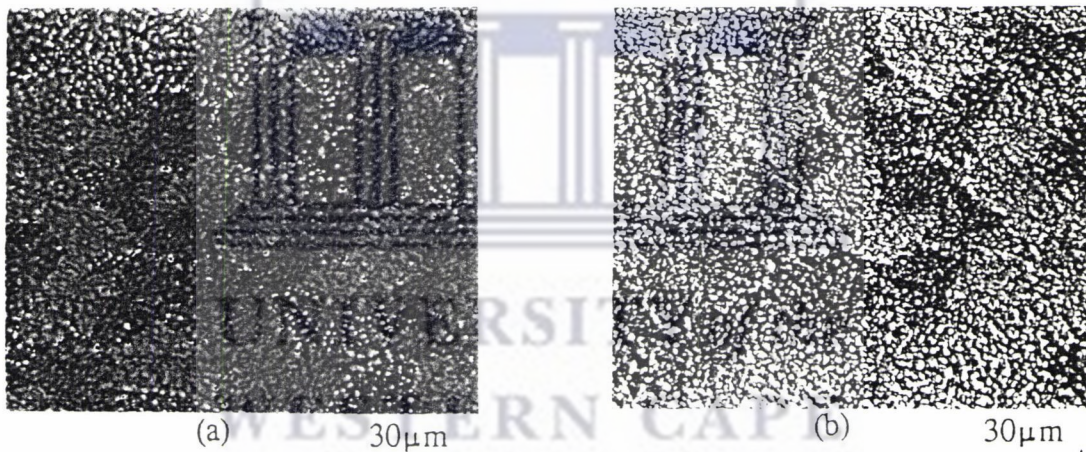

(a) 30μm   (b) 30μm

Figure 4.11 : *The effect of tilt on a backscattered electron image (a) towards the backscattered electron detector and (b) away from the detector.*

94

Figure 4.12 : *A secondary electron image of a sample annealed at 750°C for 5 minutes showing the formation of columnar NiSi₂ grains. The tips of these columnar grains generate many secondary electrons in comparison to the rest of the length below the surface, thus leading to good contrast. This image was taken at 25 kV.*
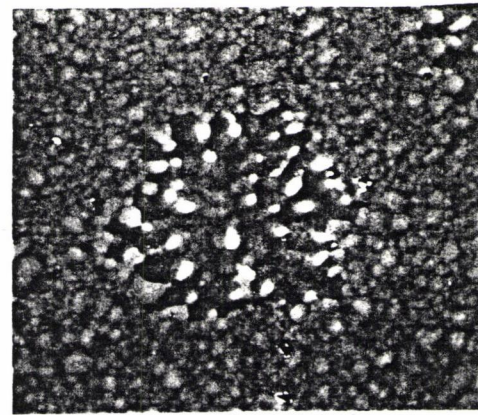
6μm

After 15 minutes of annealing at the same temperature, more and more concentric structures would have appeared after which intergrowth (lateral growth) takes place, giving rise to much larger grains. An example of this phenomena is shown in figure 4.13 in which a secondary electron image as well as the backscattered electron image of the same area is given. The

(a)   30μm   (b)   30μm

Figure 4.13 : *(a) A secondary electron image and (b) a backscattered electron image of the same area of a sample annealed at 750°C for 15 minutes. Both images were taken at 30kV.*

large grains are separated from one another by well defined grain boundaries. These grain boundaries are characterized by "holes". Energy Dispersive X-ray analysis (EDAX) showed that these holes extend from the surface of the sample to the silicon substrate since no Ni was detected inside these vacancies. With longer annealing times and at higher temperatures these holes become more apparent as we will see later. In fact, if one observes figure 4.13(a) at

95

much lower accelerating voltage so as to obtain more surface information and less information from deeper within the sample, the demonstration of grains by these holes can clearly be shown. An example of such an image is shown in 4.14 in which a secondary electron image was recorded using an accelerating voltage of 10kV.

Figure 4.14 : *A secondary electron image of a sample annealed at 750°C for 15 minutes. The image has been recorded using an accelerating voltage of 10kV. Note the demarcation of grains by grain boundaries characterized by holes.*

30µm
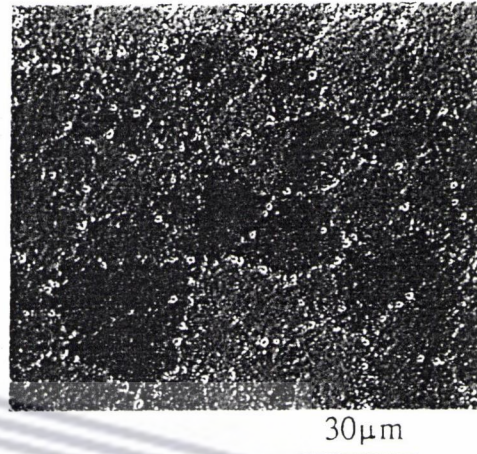
After 30 minutes of annealing at 750°C the grains in figure 4.14 have grown even larger after joining up with adjacent grains. This can be seen in figure 4.15. These large grains seem to be composed of many smaller columnar grains fused together, all orientated in the same direction.

(a) 60µm

(b) 30µm

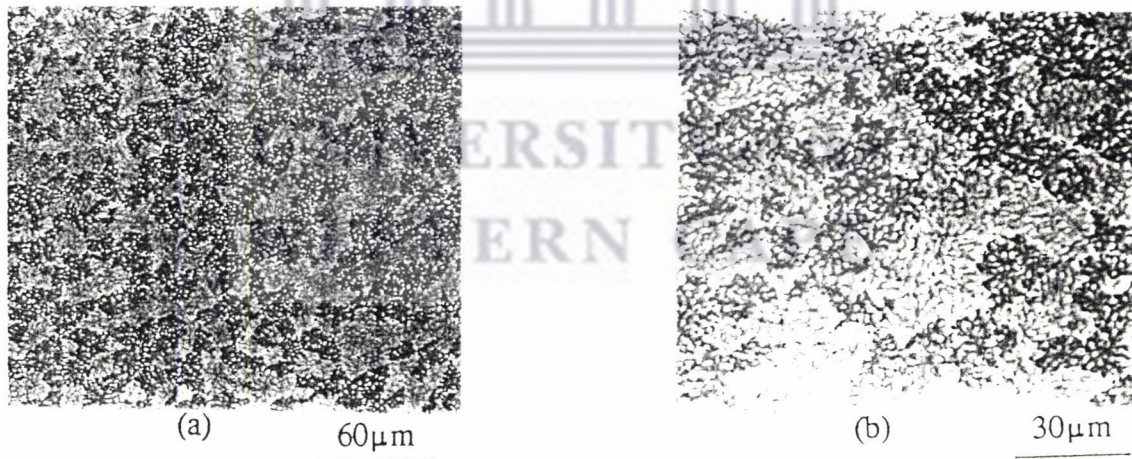Figure 4.15 : *A secondary electron image of a sample annealed at 750°C for 30 minutes (a) Low magnification (b) high magnification.*

A carpet-like appearance is observed at low magnification (figure 4.15(a)) and the vacancies on the grain boundaries has grown larger. RBS has shown this sample to consist of $NiSi_2$ grains only. Clearly, these large grains are differently orientated w.r.t. one another. This

partly explains why the channelling results in figure 4.1 (b) are so poor.

In figure 4.16 a secondary electron image of a sample annealed at 800°C for 30 minutes is given.

Figure 4.16 : *A secondary electron image of a 30 minute-800°C annealed sample. Note that the grains have grown even larger, most of them orientated in a similar way.*
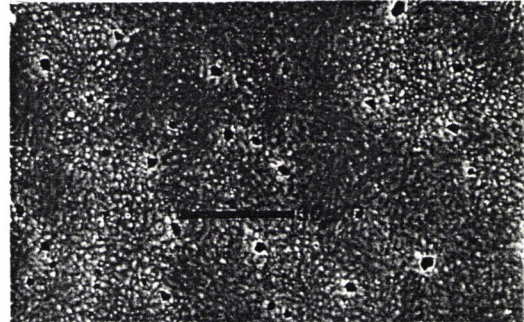
It seems as if most of the grains, which have now grown even larger, aligned themselves in a similar direction; all of them being $NiSi_2$. What is also noticeable is that the holes on the grain boundary have grown in size as well. They seem to assume a cubic shape and are normally termed "negative crystals", formed by crystal planes of surrounding grains requiring a low energy of formation. After annealing at 850°C for 30 minutes these holes become much more regular as can be seen in figure 4.17.

Figure 4.17 : *A secondary electron image of a sample annealed at 850°C for 30 minutes showing the regular shape of the vacancies.*
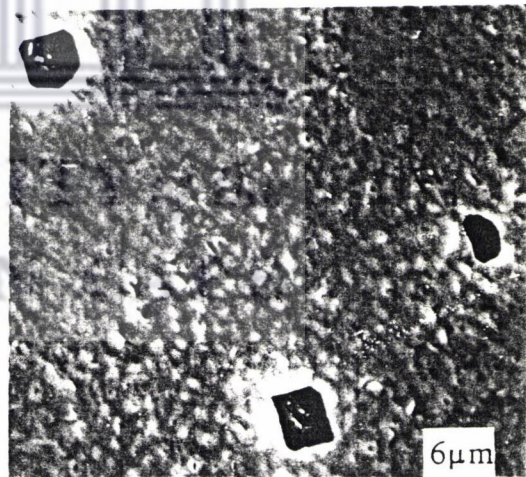
4.1.4 An AES investigation

The outcome of the AES investigation is no doubt consistent with the results from RBS. As in the case of RBS, the probe used in AES averages over a surface area of about 2 mm². Owing to the mechanism by which $NiSi_2$ formation occurs, that is in which columns of $NiSi_2$ grow in a NiSi matrix, the analysing electron beam in effect averages over pure areas of NiSi as well as over pure areas of $NiSi_2$. As in the case of RBS, the illusion is once again created that compounds of intermediate compositions are observed. Figure 4.18 shows two graphs

97

in which atomic percent has been plotted against sputter time for a sample annealed at 750°C for 5 minutes and 15 minutes respectively.
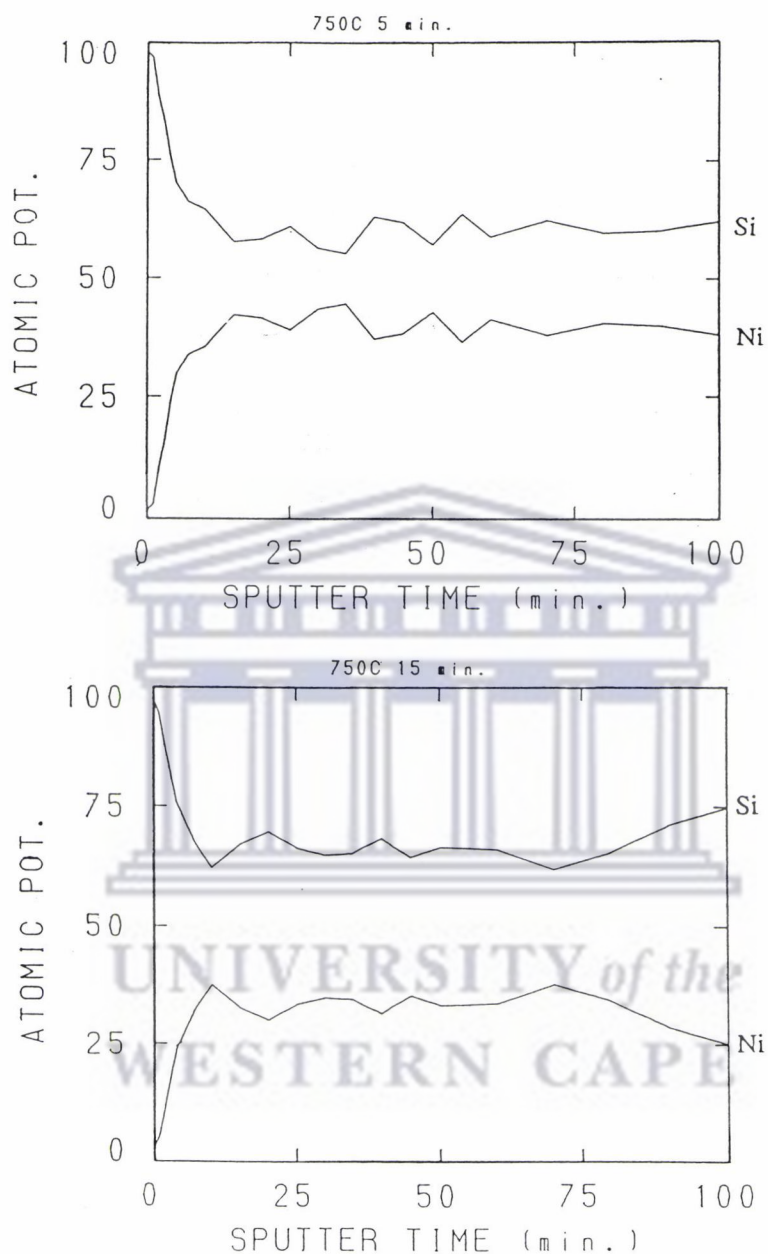

Figure 4.18 : *An AES plot of atomic percent versus sputter time for 5 minute and 15 minute annealed samples at 750°C.*

If one chooses a sputter time interval in which the atomic percent values are more or less constant (for instance between 25 and 75 minutes) for both graphs in figure 4(a) and (b), an average atomic percent value of 59.9 and 65.8 for Si are attained for the 5 minute and 15

minute annealed samples respectively. Similar plots were obtained for samples annealed for 30 minutes at 750°C and 800°C respectively. The above mentioned results are summarized in table 4.1.

Table 4.1 : *A summary of AES for various samples.*

SAMPLE		ATOMIC %	ATOMIC %	CALCULATED COMPOSITION
TEMPERATURE °C	TIME min	Si	Ni	
750	5	61.1	38.9	$NiSi_{1.5}$
750	15	65.9	34.1	$NiSi_{1.9}$
750	30	67.0	33.0	$NiSi_{2.0}$
800	30	69.7	30.3	$NiSi_{2.3}$

In the table above, the Si content in each suggested composition seems to be higher than expected. In the sample which was annealed at 800°C for 30 minutes one would generally expect $NiSi_2$. However, as reflected in the table above, the Si to Ni ratio is 2.3 to 1. This could be attributed to (1) an excess Si which is exposed from the substrate as a result of the vacancies or 'holes' in the silicide film as described in the proposed model and discussed in Section 4.2 ; or (2) the difference in sputtering rate for Ni and Si which can influence the surface composition.

4.1.5 A XRD STUDY

An XRD analysis was done on samples annealed at 750°C for 5 minutes and and 15 minutes respectively. The results are shown in figure 4.19. The Si, NiSi and $NiSi_2$ reflections are indicated at the respective peaks. The co-existence of NiSi and $NiSi_2$ is evident from these two measurements. Much more NiSi is present in the 5-minute case than in the 15-minute case as reflected in the number of counts for NiSi reflections. However a corresponding

99

increase in number of counts are observed for $NiSi_2$. This result is consistent with those obtained from other techniques. The polycrystalline nature of the NiSi phase results in many reflections (figure 4.19) while only one reflection is observed to indicate the presence of $NiSi_2$. This however, is expected due to the single crystal nature of the $NiSi_2$ phase grown on single crystal Si of almost any orientation.
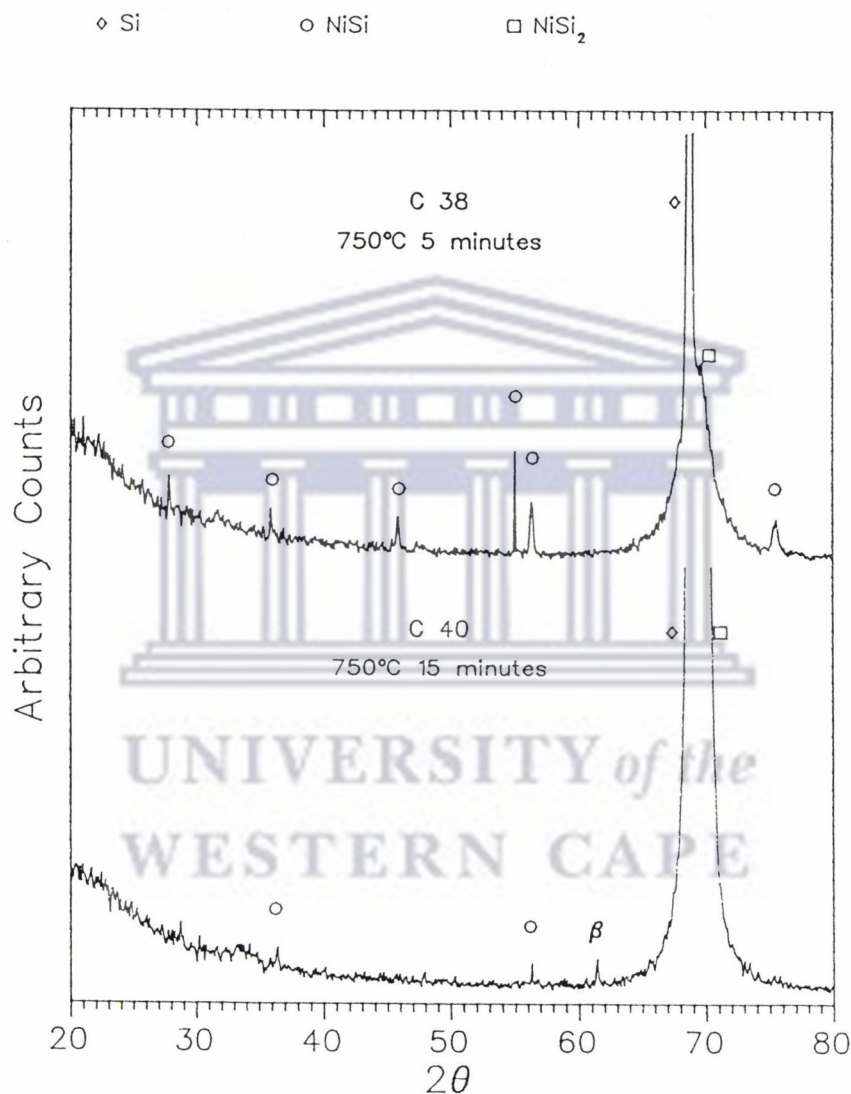

Figure 4.19 : *XRD results showing a plot of Arbitrary Counts against 2θ values for samples annealed at 750°C for 5 minutes and 15 minutes respectively. The co-existence of NiSi and NiSi₂ are shown in both cases with much less NiSi (and therefore more NiSi₂) present after 15 minutes of annealing.*

100

4.2   PROPOSED MODEL

Consider a homogeneous fully fledged polycrystalline NiSi layer, formed at 550 C for 30 minutes, as in figure 4.20 (see also figures 3.7 and 4.3). Large grains of different orientations, built up of units cells adopting the complex cubic FeSi structure, are observed.
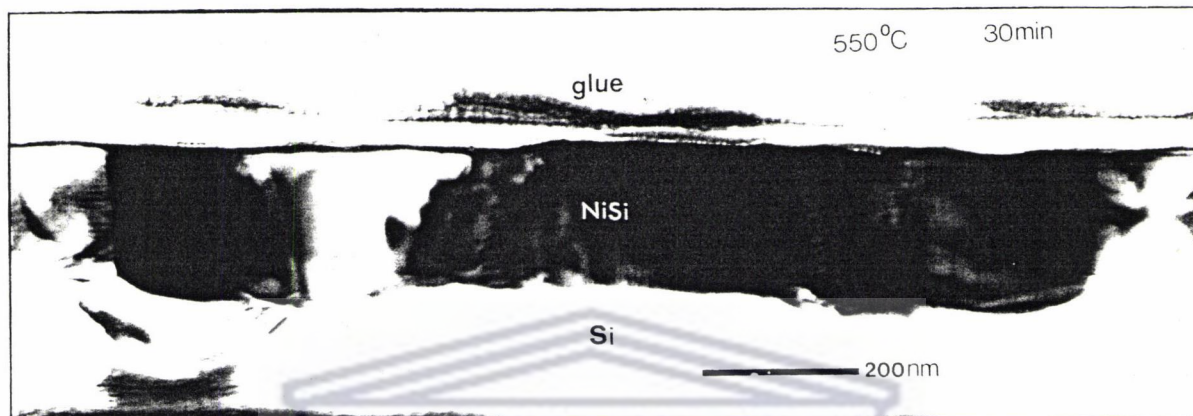
Figure 4.20 : *A cross-sectional bright field image of a fully fledged polycrystalline NiSi layer formed after 30 minutes of annealing at 550°C.*

In general, NiSi can assume one of two crystal structures; an orthorhombic MnP or a cubic FeSi crystal structure. It is understood that an orthorhombic crystal structure is only found at low temperatures (below about 450°C) after which NiSi undergoes an allotropic transformation to the complex cubic FeSi structure. In this investigation however, it was found that for short annealing times at a higher temperature (even as high as 750°C); it is possible to find orthorhombic NiSi grains (normally found at low temperatures). This is shown to be the case in figure 4.21(a) in which a cross-sectional TEM image of a sample, which has been annealed at 750°C for 5 minutes, is shown. The grain in the centre of this micrograph was found to be orthorhombic NiSi with rhombohedral $NiSi_2$ on the left and cubic NiSi on the right of this grain. The glue on top of the orthorhombic NiSi grain was used as a reference to ensure that the desired area was chosen for a diffraction analysis. The presence of this amorphous glue layer is reflected in the diffused ring structure around the central bright spot in the corresponding diffraction pattern in figure 4.21(b). This is a [001] zone axis diffraction pattern of NiSi proving its orthorhombic nature.

101
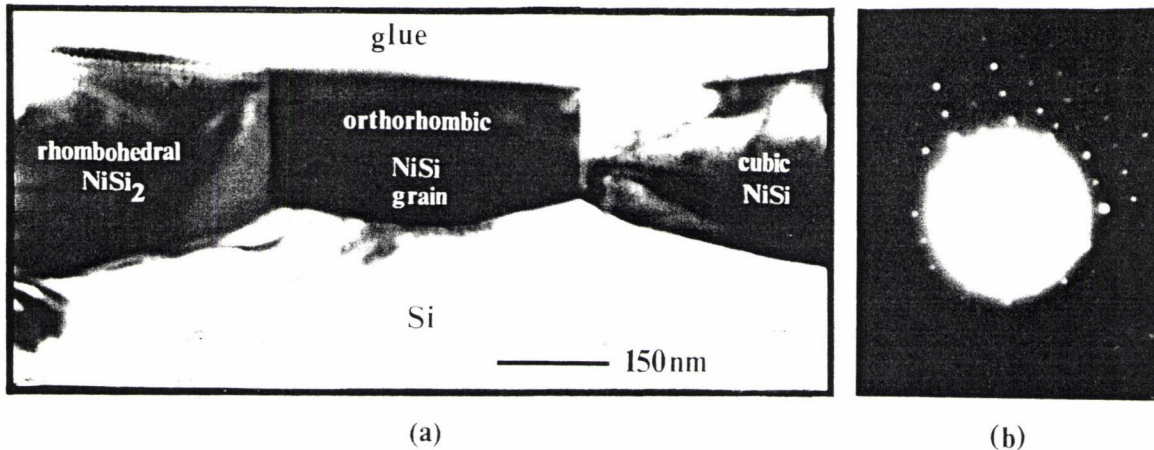
Figure 4.21 : *(a) A cross-sectional TEM bright field image of a sample annealed at 750°C for 5 minutes showing the presence of an orthorhombic NiSi grain (in the centre). The corresponding diffraction pattern from this grain is shown in (b).*

We now consider the formation of NiSi at 750°C for extremely short times; for 1 minute, say. Based on the findings as demonstrated in figures 4.20 and 4.21 respectively, one would therefore expect grains of different orientations as well as different crystal structures. Figure 4.22 is an illustration of what one would expect. Some adjacent grains are only slightly misaligned with respect to each other; maybe only slightly rotated in one direction with

Figure 4.22 : *An illustration showing a uniform layer of polycystalline NiSi. Grains B_1 and B_2, D_1 and D_2 as well as E_1 and E_2 are pairs of adjacent grains with only a slight difference in orientation with respect to each other. Grain A is assumed to be completely misaligned with respect to grain B_1, grain C completely misaligned with respect to grains B_2 and D_1, grain E_1 to D_2, and finally grain F differently oriented with respect to grains E_2 and G.*

102

respect to each other. Suppose that grains B_1 and B_2, D_2 and D_2 as well as E_1 and E_2 are such pairs of adjacent grains with only a slight difference in orientation with respect to each other. If these pairs of grains were exactly aligned with each other they would form a single crystal. Suppose furthermore that grain A was completely misaligned (maybe in more than one direction) with respect to grains B_1, grain C completely misaligned with respect to grains B_2 and D_1, grain E_1 assuming a completely different orientation (maybe in all directions) w.r.t grain D_2 and grain F different to grains E_2 and G. Some grains might be twice (or even three or more times) as large as others, resulting from adjacent grains of similar orientation joining up with each other to form a single crystal.

At 750°C after annealing for 5 minutes a bulging effect of each grain into the Si substrate is observed giving an undulating Si-silicide interface as demonstrated in figure 4.23. This effect is a direct result of lattice diffusion of Ni in NiSi into the Si substrate during $NiSi_2$ formation. This diffusion process takes place via a vacancy mechanism. A much greater volume of Ni transport from the silicide to the underlying Si is involved in lattice diffusion than in grain boundary diffusion; hence the bulging effect. This diffusion takes place via a vacancy mechanism by way of substitutional diffusion and appears to take place at a much faster rate than grain boundary diffusion. The same effect can be seen in figures 4.2(c) and (d).

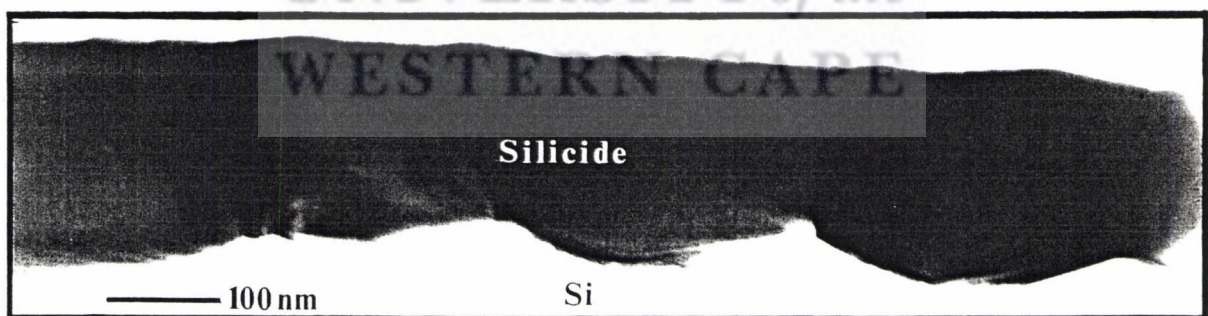**Figure 4.23** : *A cross-sectional bright field image of a sample annealed at 750 C for 5 minutes showing the bulging effect of each grain as a result of lattice diffusion of Ni in NiSi into the silicon substrate.*

https://etd.uwc.ac.za/

Figures 4.20 and 4.21 also reflect this phenomenum, although in the former case this effect has been caused by lattice diffusion of Ni into the substrate in the formation of NiSi. The extent to which each grain reflect this bulging effect depends on the crystal structure as well as its orientation with respect to the underlying silicon. It can for instance be seen in figure 4.21 that, compared to $NiSi_2$ and cubic NiSi grains, lattice diffusion of Ni in the orthorhombic NiSi grain occurs at a slower rate. Hence for this grain the bulging process occurs at a lower rate. Such grains normally remain NiSi for a longer time before converting to $NiSi_2$. The situation now is schematically illustrated in figure 4.24. During the lattice diffusion process, grain boundary diffusion, though a minor contribution in terms of the amount of Ni diffusing, also takes place and contributes to an increase in the thickness of the layer. The diffusion of

undulating Si-silicide interface caused by lattice

diffusion of Ni in NiSi into the Si substrate
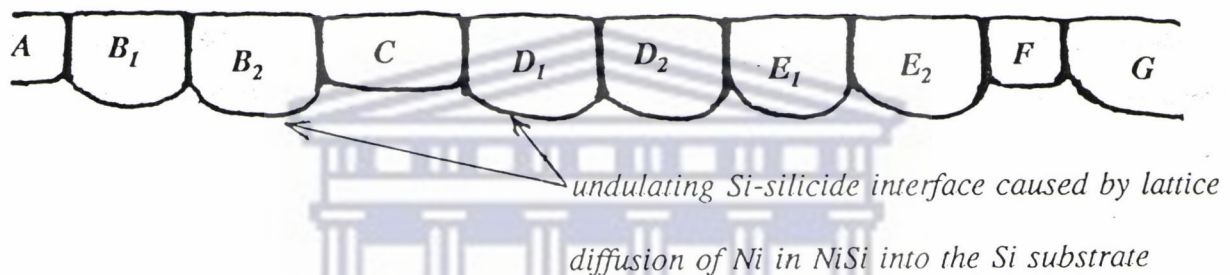
Figure 4.24 : *A schematic illustration showing a bulging effect of individual grains into the underlying Si as a result of lattice diffusion of Ni in NiSi into the Si substrate.*

Ni along grain boundaries into the silicon substrate leaves vacancies behind on the grain boundaries. Due to lattice diffusion vacancies are also caused in the lattice, but these are almost immediately filled by other available Ni within the lattice. The situation at this stage is illustrated in figure 4.25. It must be noted that during this diffusion process the NiSi lattice will initially accommodate less Ni atoms (by having vacant Ni sites in the lattice) while still maintaining its original complex cubic FeSi crystal structure. The FeSi crystal lattice will now be in an unstable state. At some stage however, when the Ni to Si ratio reaches a critical minimum, a change to a more stable crystal lattice have to occur. This happens to be $NiSi_2$ with a cubic CaF_2 type crystal structure. Unless each grain is analysed by a technique such as microdiffration in the TEM, one cannot say which grain is NiSi and which $NiSi_2$.

104

Suppose B_1 has converted to $NiSi_2$. Grain B_1 will now start to grow at the expence of grain B_2 (still NiSi at this stage) since B_1 is the thermodynamically favourable phase at this temperature. The excess Ni moves via grain boundary diffusion into the silicon matrix to form $NiSi_2$ as indicated by the hatched area in figure 4.26.

Vacancies caused by grain boundary diffusion of
Ni into the Si substrate
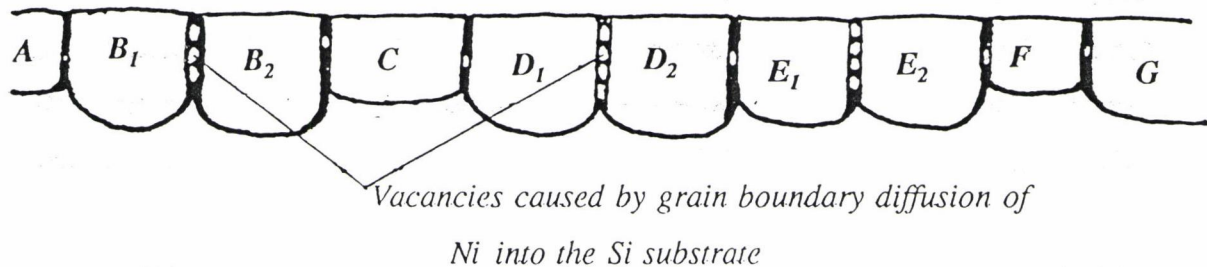
Figure 4.25 : *Lattice and grain boundary diffusion of Ni into the underlying Si cause an increase in the silicide thickness. Vacancies are caused on grain boundaries as a result of grain boundary diffusion (indicated by holes on the grain boundary in the sketch).*

The number of holes indicated on each grain boundary in figure 4.25 gives an indication of the extent to which Ni diffusion occurs across or along that particular grain boundary, keeping in mind that diffusion is most likely to take place across grain boundaries of almost similar orientated grains (i.e. tilt boundaries or rotation boundaries). Thus there exist a much greater chance for diffusion across the the grain boundary between grains B_1 and B_2 (similar to grains D_1 and D_2 as well as E_1 and E_2). This is so because the type of dislocations (edge and screw) occurring in slightly misaligned grains allow readily for Ni diffusion.
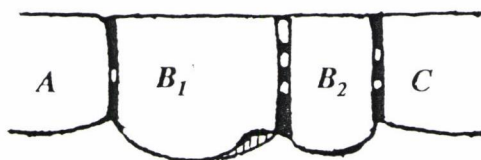
B_1 grows at the expence of B_2 therby causing the grain boundary to move into grain B_2 .

Figure 4.26 : *An illustration showing a moving grain boundary.*

105

The B_1-B_2 grain boundary will continue to move till impingement with grain C. However, if grain B_2 convert to $NiSi_2$ before this happens, the grain boundary movement will stop. If C at this stage is still NiSi, B_2 will now grow at the expence of grain C. Suppose however C has also converted to $NiSi_2$, then the grain boundary between the larger B_1 and C will remain unmoved. The excess vacancies initially present in B_2 will be absorbed into the moving grain boundary.
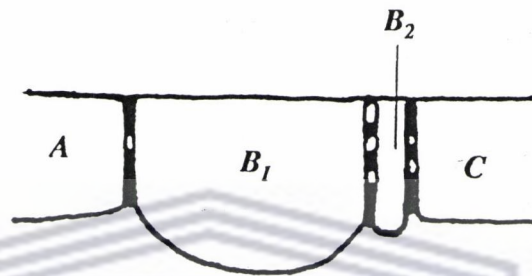
Figure 4.27 : *An illustration showing further shrinkage of grain B_2.*

larger vacancies due to fusion of grains
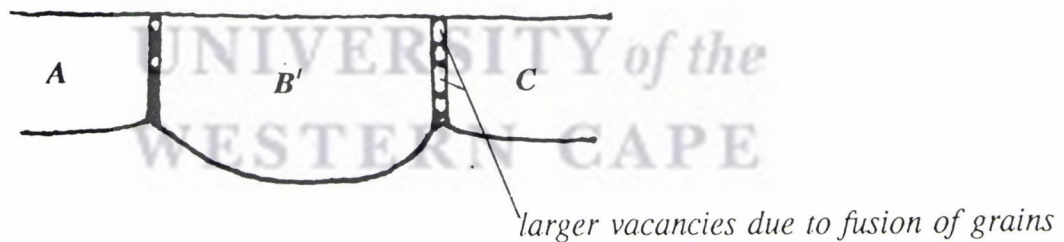
Figure 4.28 : *An illustration showing the creation of a new grain, grain B'.*

With the fusion of more grains in the fashion described above, these vacancies on the grain boundaries of these new larger grains will also grow in size until a continuous "hole" exist from the top of the silicide layer to the silicon substrate. These are the "holes" which are seen when making a SEM topographic investigation into $NiSi_2$ formation (see figures 4.14 - 4.16).

grow even larger, and since they are formed by surrounding cubic $NiSi_2$ grains, tend to take on a cubic appearence. This explains the regular shape of the "holes" seen in figure 4.17. The same type of growth mechanism as described above will occur between grains D_1 and D_2 as well as between E_1 and E_2, to form grains D^1 and E^1 respectively (figure 4.29). In some grains, maybe adopting a different crystal structure or orientation, lattice diffusion takes place to a greater or lesser extent than others so that the entire picture could look like that illustrated in figure 4.29. This type of interface morphology has been found to persist in samples which were annealed at 750°C and 800°C respectively for 30 minutes. An example
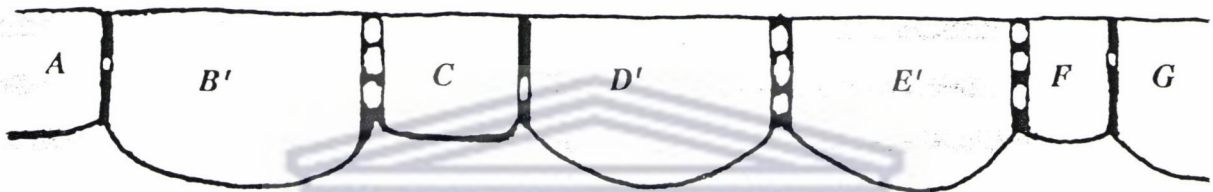
Figure 4.29 : *A silicide layer showing some fusion of grains to form larger ones. In some grains the rate of Ni diffusion into the substrate is slower than in others, depending on crystal structure and orientation.*

of a combination of grains like D^1 and E^2 as illustrated in figure 4.29 can be seen to have existed in the cross-sectional TEM micrographs in figures 4.8(a) and 4.30 in which a brightfield cross-sectional TEM image of a sample annealed at 750°C and 800°C respectively for 30 minutes is given. The picture given in figure 4.29 is clearly not indicative of the whole silicide layer. One can accept the fact that nucleation can take place at any time and at any place on the undulating Si-silicide interface. Nucleation in general depends to a large extent on the available supply of both Ni and Si at the growth interface. This availability in turn depends amongst other things on the cleanliness of the interface and thickness of the silicide film. A large increase in volume exists in the transformation from NiSi to $NiSi_2$ in which Ni diffusion can easily take place. Since not all NiSi grains transform to $NiSi_2$ simultaneously, and since not all grains have the same size, orientation or the same degree of interface

107
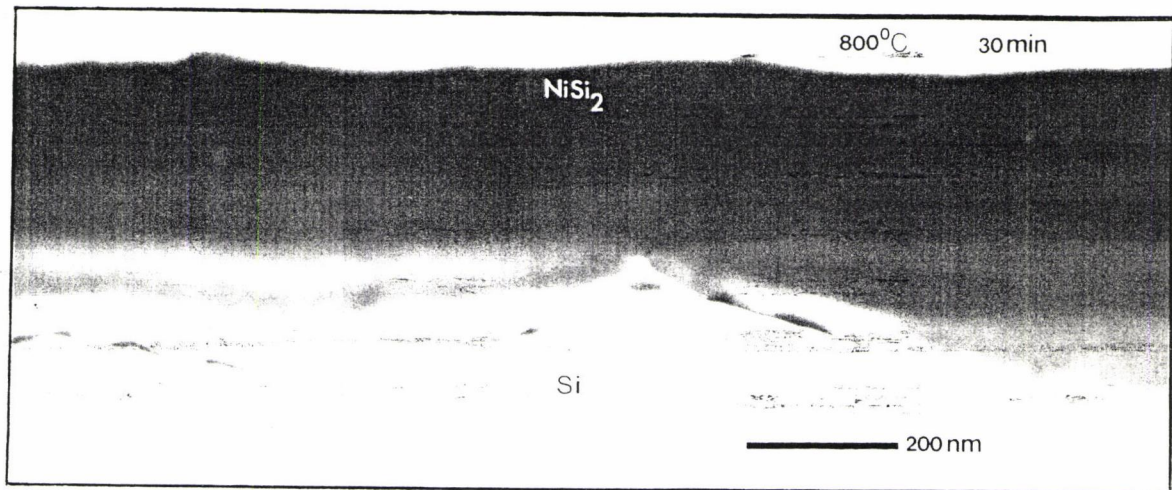
Figure 4.30 : *A cross-sectional brightfield image of a sample annealed for 30 minutes at 800°C showing a Si-silicide interface morphology analogous to that grains D¹ and E¹ combined as illustrated in figure 4.29.*

cleanliness, nucleation is more likely to occur in some grains than in others. In cases where nucleation does occur, a corrugated interface results as described in a model proposed by Lau and Cheung [La-80]. This model is describe in section 3.3. Unfortunately this model only caters for nucleation processes.

From this investigation it is apparent that $NiSi_2$ is formed by a reaction which is controlled both by normal diffusion as well as by nucleation processes. It is suggested therefore that both the proposed model from this investigation as well as that from Lau and Cheung be combined to allow for both types of interface morphologies. The final result of the interface morphology between an $NiSi_2$ layer and silicon substrate is illustrated in figure 4.31 with some grains showing more faceting (mainly as a result of nucleation) than others. If the new grains D¹ and E¹ happen to be of similar orientation, the vacancies on the grain boundary between these two grains will disappear. Grains D¹ and E¹ would then form a single crystal similar to that in figure 4.30 . This is illustrated in figure 4.32. Figure 4.32 is the most general appearance of a fully fledged $NiSi_2$ layer on Si (100). Note that with longer annealing times or for higher annealing temperatures, adjacent grains can gain enough energy

108

times or for higher annealing temperatures, adjacent grains can gain enough energy
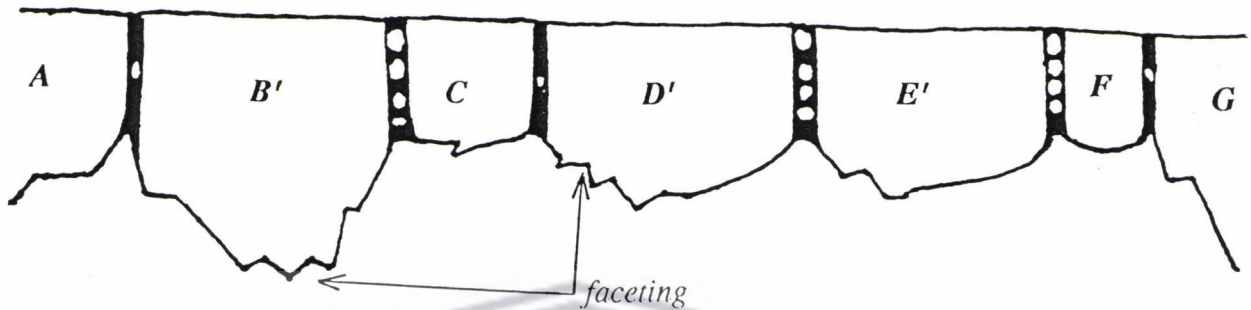
Figure 4.31 : *The formation of facets on some grains in which crystal structure alignment of the growing silicide with the silicon substrate takes place along certain crystallographic planes in which common atoms are shared.*

to align themselves with each other to facilitate diffusion of Ni across the grain boundaries, resulting once again in the growth of some grains at the expense of others. Eventually most grain boundaries will disappear to give rise to almost a continuous single crystal NiSi$_2$ film (as demonstrated in figure 4.32). Grains C and F in figure 4.32 has deliberately been indicated to show that because of their extreme difference in orientation with respect to the surrounding grains, they tend to remain less influenced by the processes around them but eventually does change to NiSi$_2$ independently. An example of such grains can be seen in figure 4.8(b).

The most general case for a fully fledged NiSi$_2$ layer will therefore be a mixture of both nucleation and faceting as well as normal diffusion processes. This model is well supported by the cross-sectional TEM study as well as the topographic SEM investigation. These

109

observations are in turn complemented by the results from RBS, AUGER and XRD.

formation of a continuous 'hole' to the Si substrate
due to an accumulation of many vacancies ────

position of previously existing
grain boundary

fused NiSi₂ grain
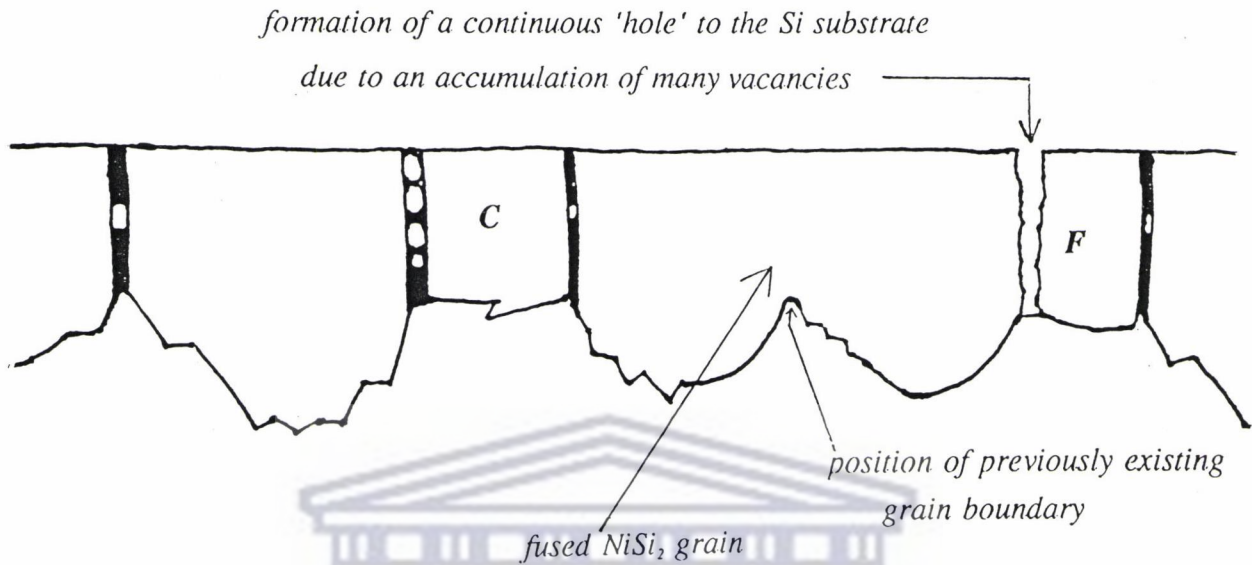
Figure 4.32 : *The most general case for the formation of NiSi₂ on Si (100). Most of the grain boundaries has practically disappeared to form a continuous film of NiSi₂.*

This model can be tested using microdiffraction on samples annealed at very short times in order to follow the phase transition process more closely. The proposed model can be summarized as follows :

(1) Lattice diffusion of Ni causes grain bulging into the Si substrate

(2) NiSi grains convert to NiSi₂, some grains taking longer than others

(3) These grains grow laterally at the expence of unconverted grains

(4) Excess vacancies in the grains are swept into the remaining grain boundaries and coalesce into continuous holes from the silicon substrate to the surface.

110

4.3   AN EVALUATION OF THE MODEL

The proposed model is based on the assumption that Ni is the main diffusing species during $NiSi_2$ formation. Four references quoted in table 1.1 point to the fact that Ni is the major diffusing species.

To test this model from a thermodynamic point of view, we consider the following values of enthalpy and entropy which are quoted for the formation of $NiSi_2$:

element or compound	$\Delta S°$ (J/deg.mole)	$\Delta H°_f$ (kJ/mole)
Si	0	0
NiSi	-4.35	-85.4
$NiSi_2$	-2.26	-86.6

The reaction for $NiSi_2$ formation is: $NiSi + Si \rightarrow NiSi_2$

The change in enthalpy and entropy for this reaction can thus be calculated respectively as:

$$\begin{aligned}
\Delta H &= \Delta H°_f (NiSi_2) - \Delta H°_f (NiSi) \\
&= -86.6 \quad - (-85.4) \\
&= -1.20 \text{ kJ/mole}
\end{aligned}$$

and

$$\begin{aligned}
\Delta S &= \Delta S° (NiSi_2) - \Delta S° (NiSi) \\
&= -2.26 - (-4.35) \\
&= +2.09 \text{ J/deg.mole}
\end{aligned}$$

It can also be shown that a 10% uncertainty of the values of the heats of formation [Pr-78] could result in a positive heat of formation for $NiSi_2$ from NiSi. Therefore, having, a heat of formation close to zero, the contribution to the free energy from the $T\Delta S$ - term (in $\Delta G = \Delta H - T\Delta S$) becomes decisive. Because ΔS has a positive value, $T\Delta S$ contributes towards lower free energy at increasing temperatures, for example at 750°C (1023 K):

At 1023 K $\quad \Delta G_{NiSi2} = \Delta H - T\Delta S$

$$= -1.20 - (1023 \times 2.09 \times 10^{-3}) \text{ kJ/mole}$$

$$= -3.34 \text{ kJ/mole}$$

This result indicates that at 750°C NiSi is unstable and therefore the reaction becomes thermodynamically favourable to transform NiSi to $NiSi_2$. Owing to the relatively small driving force needed at this temperature for $NiSi_2$ formation one would expect that NiSi should switch over to $NiSi_2$ within a very short time.

This study has, however, proved that even after 15 minutes of annealing at 750°C, some grains were still NiSi (identified by micro diffraction). This means that there is more than just the thermodynamic aspect involved in deciding when NiSi should transform to the final phase. According to the proposed model one of the major factors in determining the time lapse for transformation to take place, is the question of grain orientation with respect to each other and with respect to the silicon substrate. This is said keeping in mind that it is possible that differences in grain orientation (or crystal orientation) could hamper Ni diffusion (to a certain extent) across grain boundaries as well as across the silicon-silicide interface. This is regarded by the proposed model as the main reason why a time lapse of up to 10 minutes or more is encountered for some grains to switch to $NiSi_2$. Other factors like the cleanliness of the Si-silicide interface, grain size and substrate orientation will also undoubtedly play a role.

The bulging effect observed after only 5 minutes of annealing at 750°C is most probably caused by lattice diffusion. Once Ni diffuses out of a NiSi grain to cause the bulge, one would like to assume that this is the initial stage of $NiSi_2$ formation. The fact, however, that even some slightly bulged grains were identified as NiSi (and not $NiSi_2$), indicates an uncertainty regarding the degree of bulging before switching to $NiSi_2$. It is suggested by the model that NiSi can loose a certain amount of Ni atoms while still maintaing the original NiSi lattice but with vacant Ni sites (although perhaps chemically closer to $NiSi_2$). Since the crystal structure determines the phase (and not a slight change in relative concentration), such

112

grains, although slightly bulged due to some Ni diffusion are still NiSi. These grains are unstable and will switch to $NiSi_2$ when a critical Ni to Si ratio is reached. The actual switching probably occurs within manoseconds. There is absolutely no way, other than by a technique similar to microdiffraction, that the true identity of a specific grain can be determined.

This model suggest that, for the start at least, $NiSi_2$ formation is mainly diffusion controlled i.e. normal diffusion processes are involved. Even at higher temperatures or for longer annealing times, similar Si-silicide interface morphologies to that at 750°C for 5 minutes were encountered which suggest a similar kind of diffusion process. However, this model does not rule out nucleation processes completely. It is interesting to note that $NiSi_2$ decomposes at 993°C by a peritectic reaction [Ha-69]. Such a low temperature instability, relative to other silicide compounds, might indicate that the $T\Delta S$-term indeed becomes a significant factor in the formation of $NiSi_2$. Thus, having such a relatively small driving force at low temnperatures ($< 750°$), impurity or intrinsically related defects at the Si-NiSi interface may cause nonuniform nucleation of $NiSi_2$ in the way described by Lau et.al. (see figures 3.10 and 3.11). As a result of this laterally non-uniform growth the $Si-NiSi_2$ interface will become jagged due to faceting. The Ni-profile in an RBS spectrum would therefore assume intermediate values between that of Ni in NiSi and Ni- in - $NiSi_2$. The same effect can be caused by an undulating $NiSi_2$ - Si interface as encountered in this investigation.

This model therefore allows for both diffusion (as in lattice diffusion) and nucleation (i.e. starting from a point and growing outward in all directions) processes.

113

CHAPTER 5

SUMMARY AND CONCLUSIONS

Several review papers have been written on transition metal silicides which have attracted considerable attention in recent years because of the potential usefulness of these silicides in silicon integrated circuits [Ar-65,We-67]. Thin-film silicides formed by reaction between thin films and between thin films and substrates were reviewed by Tu and Mayer [Tu-78] and Ottaviani [Ot-79]. Murarka [Mu-80] considered the silicides for application in silicon integrated circuits. Most of the silicide research which were performed from the beginning of this century through to the 1960s used powder metallurgical techniques to produce silicides. These studies revealed important silicide properties such as electrical resistivities, high-temperature stability, corrosion resistance, silicide crystal chemistry and metal-silicon phase diagrams. The possibility of using silicides as conductors, gates and interconnects ([Le-69],[Mu-79]) in silicon integrated circuits motivated thin film research. Besides the measurements of Schottky barrier heights and resistivities, the intermetallic formation in the metal-silicon systems, reaction and interdiffusion kinetics, stability at the integrated circuit processing and operating temperature, mechanical stability, oxidation and etching characteristics, and epitaxial growth on silicon have all been investigated in the last three decades.

Since the application of metal silicide films in VLSI devices demands a very high degree of uniformity, stability and reproducibility, such strict control on the formation of these silicide can only be achieved by knowing and understanding, amongst other things, the growth mechanisms and kinetics of the various metal silicide systems, the deposition technique, ambients during heat treatment and the temperature of growth. Some of these growth parameters were addressed in this work and investigated for Ni-silicide forming systems in the context of existing models and theories of diffusion [Ki-61,Wa-69], reaction kinetics [Ha-67], phase sequence [Pr-84] and growth mechanisms [La-80].

114

In this investigation the growth mechanism of nickel silicide formation received prime attention. With the use of Rutherford Backscattering Spectrometry, cross-sectional Transmission Electron Microscopy, Auger emission Spectroscopy and X-ray Diffraction a wealth of information regarding the growth processes were extracted. Interface morphology between silicide and silicide as well as between silicide and silicon were inspected. The crystalline nature of the various phases were also investigated. The transition process of NiSi to $NiSi_2$ was of considerable interest and a model has been proposed for the growth mechanisms involved in $NiSi_2$ formation.

First phase formation (Ni_2Si) was investigated at 290°C. It was found that after 5 minutes of annealing 25 nm of Ni_2Si has formed. This was a polycrystalline silicide layer of uniform thickness. RBS reflected a sharp interface between silicide and unreacted nickel as well as between silicide and silicon substrate. Cross-sectional TEM confirmed this to be the case. After 20 minutes of annealing all the nickel was consumed to give a fully grown Ni_2Si layer. It was found that after 30 minutes of annealing some degree of diffusion of Ni in Ni_2Si has taken place to prepare the way for second phase formation (NiSi). At no instant did Ni_2Si and NiSi co-exist with unreacted Ni-metal. These results were confirmed by an Auger analysis.

NiSi formation was studied at 330°C and at 350°C. After 20 minutes of annealing at 330°C all the Ni-metal was consumed to form a NiSi layer about half the thickness of the full silicide layer, the other half being Ni_2Si. After annealing at 330°C for 30 minutes a thin Ni_2Si layer still existed. At 350°C for 10 minutes only a trace of Ni_2Si still existed, the bulk of the silicide being NiSi. The interface between the Ni_2Si and NiSi layers was irregular resulting in non-uniform thickness for the two silicides. The emerging NiSi grains seemed to assume on orthorhombic crystal structure, thereby showing some form of columnar layer by layer growth. Once the full thickness was reached, lateral growth took place, some grains growing at the expense of others. During initial NiSi formation electron diffraction showed the presence of smaller NiSi crystallites scattered amongst larger ones, all assuming a random orientation, thus confirming the polycrystalline nature of NiSi. At 550°C, well developed cubic NiSi grains were encountered. This phase remained stable up to about 700°C.

115

Upon further annealing at 750°C for 5 minutes Ni diffusion in NiSi takes place to bring about NiSi$_2$ formation. Rutherford Backscattering Spectrometry, cross-sectional TEM, SEM and XRD showed the presence of both NiSi and NiSi$_2$. Microdiffraction was extremely useful since individual grains could be analysed. Silicide phases as well as crystal structure and orientation of various grains could be identified. For instance in the above-mentioned sample, rhombohedral and cubic NiSi$_2$ grains as well as orthorhombic and cubic NiSi grains were encountered. The cubic NiSi$_2$ grains, which have a CaF$_2$ - type crystal structure, were found to grow expitaxially onto the Si - substrate. NiSi$_2$ takes place mainly via a nucleation process resulting in columnar growth. This is a fast process. Once these columns shoot through the entire silicide thickness, lateral growth takes place. The NiSi$_2$ - Si interface is extremely non-uniform with immense facets extending into the Si-substrate. This is a direct result of nucleation. NiSi$_2$ grains, which initially grow as columns in NiSi, grow into the silicon substrate after nucleating on the original NiSi - Si interface. If the lateral growth rate is much faster than the nucleation rate at the remaining unreacted NiSi - Si interface, the grains will grow until impingement, thus leading to a relatively flat NiSi$_2$ - Si interface between the initial nucleation sites where the grains protrude into the silicon substrate. This type of silicide formation would then lead to a jagged interface. Channelling results were extremely poor for NiSi$_2$ structures with channelling minimum yield (χ_{min}) values of 60% and above. These poor results are speculated to be attributed to misfit dislocations resulting in strain and ultimately fracture. Faceting can also hamper the epitaxial nature of NiSi$_2$ on the Si - substrate.

If viewed from the surface, NiSi$_2$ initially seems to grow laterally in a concentric fashion from a central point. These circular islands of NiSi$_2$ grow in size until, at 750°C for 15 minutes of annealing, impingement with other NiSi$_2$ areas occur. The boundaries, after impingement of different NiSi$_2$ grains, are characterized by vacancies suggesting vacancy diffusion of Ni in the formation of NiSi$_2$. A model has been proposed in this regard to explain the growth processes involved in NiSi$_2$ layer formation after annealing a sample at 750°C for 30 minutes. The channelling minimum yield at χ_{min}, was found to be about 60%. A SEM study showed a conglomeration of large grains, some differently oriented w.r.t others. Samples annealed at 800°C for 30 minutes showed even larger grains, some facing towards and others away from the backscattered electron detector. This caused some degree of contrast between grains

116

for all samples analysed in which NiSi$_2$ formation has taken place.

An interesting finding from cross-sectional TEM is that some grains seem to have grown via a diffusion process and not via nucleation. This is reflected in some grains maintaining the same kind of morphology at 800°C after annealing for 30 minutes as in a sample annealed at 750°C for 5 minutes where a diffusion process has primarily been encountered. The only difference was the size of the grains since more grain boundaries had disintegrated after an 800°C anneal to form larger grains. At this temperature some NiSi$_2$ grains were also found to be slightly differently oriented w.r.t. the rest of the epitaxial NiSi$_2$ layer.

The results of this investigation were extremely useful in understanding the growth processes involved in Ni-silicide formation. The fact that diffusion as well as nucleation processes are involved in the transition from NiSi to NiSi$_2$ is of special interest.

117
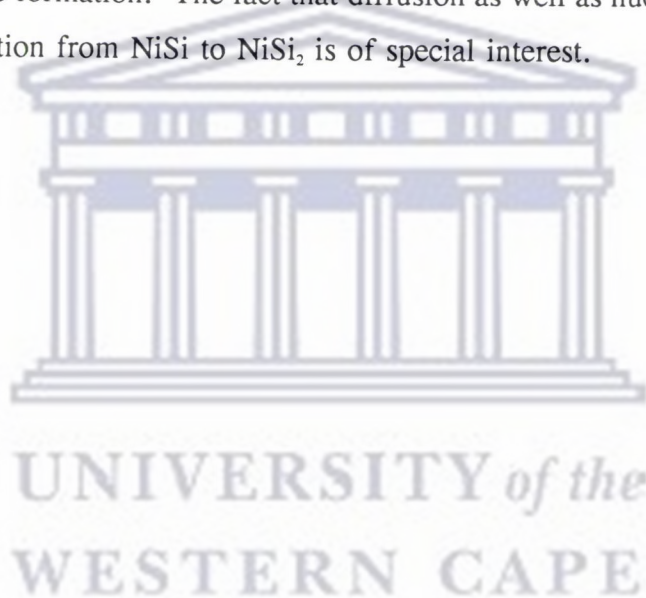
REFERENCES

[Af-85]   K. Affolter, X. - A.Zhao and M.-A. Nicolet; *J Appl. Phys.*, **58** (1985) 3087.

[Ar-65]   B.A. Aronsson, T.Lundstrom, S.Rundquist om *Borides, Silicides and Phosphides* edited by B.A. Aronsson et al (New York: Wiley, 1965)

[Ar-77]   A. Armigliato, *Electrochemical Soc.* 77-2,638 (1977).

[Ba-74]   E.B. Badtiev, O.S. Petrushkova, and L.A. Panteleimonov, *Vestm. Moskov, Univ. Khim.* **29**, No. 3, 367-368 (1974).

[Ba-78]   J.E.E. Baglin and J.M Poate; *Thin Films Interdiffusion and Reactions,* ed. by J.M. Poate, K.N. Tu and J.W. Mayer, Wiley-Interscience, 1978, Chapter 9.

[Ba-80]   J.E.E. Baglin and F.M. d'Heurle, W.N. Hammer and S.Peterson; *Nucl. Instr. and Meth.,* **108** (1980) 491.

[Ba-80(a)] J.Baglin, F.d'Heurle and S.Petersen, in *Thin Film Interfaces and Interactions* edited by J.Poate, J. Baglin, Electrochemical Soc, Princeton (1980), p.341.

[Ba-82]   J.E.E. Baglin, H.A. Atwater, D.Gupta and F.M d'Heurle; *Thin Solid films,* **93** (1982) 255.

[Be-82]   R.W. Bené, *Appl. Phys. Lett.* **41**, 529 (1982).

[Bo-33]   B. Borén, *Ark. Kemi Min. Geol.* **11A** (1933) no.10.

[Bo-80]   A.P. Botha, R.Pretorius and J.C. Lombard, *Annu. Res. Rep.,* 1980, P.62 (Southern Universities Nuclear Institute, Faure, South Africa).

[Bo-81]   A.P. Botha and R. Pretorius; *Proc. Conf. Mater. Res. Soc., ed. by P.S. Ho*

118

and K.N. Tu, vol 10 (1981)129.

[Bo-82]   *A.P.Botha and R. Pretorius, Thin Solid Films,* **93** (1982)127.

[Bo-82(a)] A.P. Botha; *Solid State Diffusion in Metal Silicides,* PhD. Thesis, 1982, Univ. of Stellenbosch, South Africa.

[Br-82]   L.J, Brillson; *Thin Solid Films,* **89** (1982) 461.

[Ca-79]   C.Canali, G. Majni, G.Ottaviani and G.Celotti, *J. Appl. Phys.,* 50 919790 255.

[Ch-74]   W.K. Chu, H.Kvaütle, J.W.Mayer, H.Müller, M.A. Nicolet and K.N. Tu; *Appl. Phys. Lett.* **25** (1974) 454.

[Ch-78]   W.K. Chu, J.W. Mayer and M.A. Nicolet *Backscattering Spectrometry* (Academic Press, New York, 1978).

[Ch-83]   D.Chescae and P.J. Goodhew in *The operation of the transmission electron microscope* edited by D.Chescae and P.J. Goodhew, Royal Microscopial Society, Oxford University Press, New York (1984)

[Co-76]   D.J. Coe and E.H. Rhoderick; *J.Phys.* D.: Appl. Phys. **9** (1976) 965.

[Co-82]   S.S. Cohen, *J. Appl. Phys,* **53** 8856 (1982).

[Cr-80]   C.A. Crider, J.M. Poate and J.E. Rowe; *Symp. Proc. Thin Film Interfaces and Interactions; Electrochem. Soc.,* ed. by J.E. E. Baglin and J.M. Poate, val **10** (1980) 135.

[Da-27]   Davison, C. and L.H. Germer. 1927 *Physical Rev.* **30** (pp 705-740).

[dB-24]   deBroglie, *Phil Mag.* **47** pp 446-458 (1924).

[Do-73]   J.D.M. Donnay and H.M. Oudik, *Crystal Data- Determinature Tables,* Vol. Z.U.S. Department of Commerce, National Bureau of Standards and the Joint Committee on Powder Diffraction Standards, 1973.

[Do-85]   L.R. Doolittle, *Nucl. Instr. and Meth.* B4, 344(1985)

[Fi-78]   T.G. Finstad; *Phys. Stat. Sol (a),* **63** (1981) 223.

[Fi-81]   T.G. Finstad, *Phys. Status Solidi A,* 63 (1981) 223.

[Ga-65]   P.Gage and R.Bartlett, *Trans. AIME* **233**, 832 (1965).

[Gö-82]   U.Gösele and K.N. Tu; *J.Appl. Phys.* **53** (1982) 3252.

[Go-92]   P.J. Goodhew an F.J. Humphreys in *Electron Microscopy and Analysis* edited by P.J. Goodhew and F.J. Humphreys, Burgess Science Press, Basomgstoke, Hampshire (1992)

[Gu-77]   G.J. van Gurp, in *Semiconductor Silicon,* H.huff and E. Sirtl, eds. The Electrochemical Society, Princeton, (1977), p. 342.

[Gu-78]   D.Gupta, D.R. Campbell and P.S. Ho, in *Thin Films. Interdiffusion and Reactions,* edited by J.M. Poate, Kn Tu and J.W. Mayer (Wiley, Nwe York, 1978) Chapter 7.

[Ha-58]   M. Hansen, *Constitution of Binary Alloys, 2nd edition* (McGraw-Hill, New York, 1958) pages 1040 and 1141.

[Ha-65]   M. Hansen and K. Anderko, *Constitution of Binary Alloys* (McGraw-Hill, New York, 1965).

[Ha-65]   H.Hansner, *Coatings of High Temperature Materials,* ed., Plennnum Press, New York (1965).

[Ha-67]   N.B. Hannay; *Solid State chemistry,* Prentice - Hall Inc., New Jersey, 1967

[Ha-69]   M.Hansen; *Constitution of binary alloys,* McGraw-Hill, New York, 1969.

[Ha-90]   C.Hammond in *Introduction to Crystallograhpy* edited by C. Hammond, Oxford University Press, Royal Microscopial Society (1990)

[d'H-82]   F.d'Heurle, S. Peterson, L. Stolt and B. Stritzker; *J. Appl. Phys.,* **53** (1982) 5678.

[d'H-84]   F.d'Heurle, C.S. Peterson, J.E.E. Baglin, S.J. la Placa and C.Y. Wong, *J. Appl. Phys.,* **55** (1984) 4208.

[He-85]   J.C. Hensel, A.F.J. Levi, R.T. Tung and J.M. Gibson; *Appl. Phys. Lett.,* **47** (1985) 151.

[Ho-84]   K.T. Ho, C.D. Lien, M.A. Nicolet and D.M. Scott; *Symp. Proc. Thin Films and Interfaces II,* MRS, ed. by J.E.E. Baglin, D.R. Campbell and W.K. Chu, val **25** (1984) 123.

[Hu-85]   L.S. Hung, J.W. Mayer, C.S. Pai and S.S. Lau; *J. Appl. Phys.,* **58** (1985) 1527.

[Hu-85(a)] L.S. Hung, E.F. Kennedy, C.J. Palmstrom, J.O. Olowolafe, J.W. Mayer and H. Rhodes; *Appl. Phys.* Lett., **47** (1985) 236.

[Ki-61]   G.V. Kidson; *J. Nucl. Mater.,* **3** (1961)21

[Ki-73]   C.J. Kircher, J.W. Mayer, K.N. Tu and J.F. Ziegler, *Appl. Phys. Lett., 22*

121

(1973) 81.

[Kn-85]   *J.A. Knapp., S.T. Picraux, C.S. Wu and S.S. Lau; J. Appl. Phys.* **58** (1985) 3747.

[Kr-74]   H. Kräutle, M.A. Nicolet, and J. Mayer, *J. Appl. Phys.* **45**, 3304 (1974).

[Ku-79]   O. Kubashewski and C.B. Alcock; *Metallurgical Thermochemistry,* 5th edition, Pergamon Press, 1979.

[La-75]   S.S. Lau, J.S. -Y. Feng, J.O. Olowolafe and M.-A. Nicolet; *Thin Solid Films,* **25** (1975) 415.

[La-80]   S.S. Lau and N.W. Cheung; *Thin Solid Films,* **71** (1980)117

[Le-69]   M.P. Lepselter, J.M. Andrews in *Ohmic Contacts to Semiconductors,* ed. B. Schwartz (Electrochem Soc, Princeton, N.J, 1969) p159-86

[Li-84]   C.-D. Lien, M. Bartus and M. A. Nicolet; *Proc. Symp. o n Thin Films and Interfaces II*, MRS, ed. by J.E.E. Baglin, D.R. Campbell and W.K. Chu, val. 25 (1983) 51.

[Li-84(a)] C.-D. Lien, M. -A. Nicolet and S.S. Lau., *Phys. Stat. Sol.* (a), **81** (1984) 123.

[Li-84(b)] C.-D. Lien and M.-A. Nicolet; *Symp. Proc. Thin Films and Interfaces II,* MRS, ed. by J.E.E. Baglin, D.R. Campbell and W.K. Chu, val **25** (1984) 131.

[Lo-73]   L. Locler and C. Capio, *J. Appl. Phys.* **44**, 4366 (1973).

[Ma-68]   J.R. Manning, *Diffusion Kinetics for Atoms in Crystals* (D van Nostrand

Company, Inc. Princeton, New Jersey, 1968) Chapters 1 and 2.

[Ma-80]   A. Martiney, D. Esteve, A. guivarch, P.Auvray, P. Heuse and G. Pelons; *Solid State Electronics,* **23** (1980) 55.

[Ma-93]   T.K. Marais; *Phase Formation Sequence in Metal-Semiconductor and metal-metal Binary Thin Film Systems,* PhD. Thesis, 1993, University of the Western Cape, South Africa.

[Mo-78]   W.G. Moffat, *Handbook of binary Phase Diagrams* (General Electric Company, New York, 1978).

[Mu-79]   S.P. Muraka, IEEE-IEDM 1979 *Technical Digest.* (IEEE, New York, 1979) pp 454-457

[Mu-80]   S.P. Murarka, *J.Vac.Sci. Technol,* **16**, pp 775-792 (1980)

[Mu-83]   S.P. Murarka, *Silicides for VLSI Applicataions* (Academic Press, New York, 1983).

[Na-76]   K.Nakamura, J.O. Olowolafe, S.S. lau, M.-A. Nicolet and J.W. Mayer; *J.Appl. Phys.,* **47** (1976) 1278.

[Ni-83]   M.A. Nicolet and S.S. Lau, in *VLSI Electrons; Microstructural Science,* edited by N. Einsrpuch (Academic Press, New York, 1983).

[Oa-72]   Oatley, C.W. *The Scanning Electron Microscope,* Campbridge Univ. Press. Campbridge, UK, p194. (1972)

[Oe-88]   M.Oeffino, *J. Appl. Phys,* **64**, 607 (1988).

[Ol-76]   J.O. Olowolafe, M.-A. Nicolet and J.W. Mayer; *Thin Solid Films,* **38** (1976)

143.

[Os-39]   A. Osawa and M. Okamoto, *Sci. Rep. Tohoka Univ.*, First Series, **27** (1939) 326.

[Os-82]   C.M. Osburn, *Proc 1st Int. Symp. on VLSI Sci and Tech Electrochemical Society,* (82-1 213 (1982).

[Os-90]   C.M. Osburn *"Formation of Silicated, Ultra - Shallow Junctions using low Thermal Budget Processing"* J. Electron Mater, 18 67 (1990).

[Ot-79]   G.Ottaviani, *J. Vac. Sci. Technol,* **16**, pp1112-1119 (1979)

[Ot-86]   G. Ottaviani, *Thin Solid Films* **140**,, 3 (1986).

[Pa-48]   L. Pauling, A.M. Soldate, *Acta Cryst.*, **1** (1948) 212.

[Pe-65]   Pease, R.F.W., and W.C. Nixon 1965t. *High resolution scanning electron microscopy. J.Sci Instr.* 42: 81-85.

[Pe-79]   S. Peterson, J. Baglin, W. Hammer, D. d' Heurle, T.S. Kuan, I. Ohdamari, J. de S. Pires and P. Tove; *J. Appl. Phys.,* **50** (1979) 3357.

[Po-80]   M.T. Postek, K.S. Howard, A.H. Johnson and K.L. McMicheal in *Scanning ELectron Microscopy - A student's handbook* edited by M.T. Postek, Ladd Research Industries (1980)

[Pr-78]   R. Pretorius; *J. Appl. Phys.,* **48** (1977) 3379.

[Pr-78(a)]   R. Pretorius, J.M. Harris and M.A. Nicolet;   *Solid State Electronics,* **21** (1978)667.

[Pr-81] R. Pretorius; *J. electrochem. Soc.*, **128** (1981) 107.

[Pr-84] R. Pretorius, *MRS Proc.* **25**, 15 (1984).

[Pr-86] R. Pretorius, M. Wandt, A.P. Botha, M.C. Comrie and J. McCleal.

[Pr-90] R. Pretorius, *Vaccum* **41**, 1038 (1990).

[Pr-90(a)] R. Pretorius, R. de Rens, A.M. Vredenburg, and F.W. Saris, *Materials Letters* **9** 494 (1990).

[Pr-91] R. Pretorius, R de Rens, A.m Vredenberg, and F.W. Saris, *J. Appl. Phys.* **70**, 3636 (1991).

[Pr-92] R. Pretorius, T.K. Marais, A.E. Muller and D. Knoesen, *MRS Proc*, **238**, 475 (1992).

[Pr-92(a)] R. Pretorius, C.C. Theron, T.K. Marais and H.A. Ras, *Materials Chemistry and Physics* (1992).

[Ra-87] H.A. Ras; The *Solid State Chemistry of Co-Si and Ni-Si Binary thin film systems*, PhD. Thesis

[Ro-83] M. Ronay, *Appl. Phys. Lett.* **42**, 577 (1983).

[Sa-80] G.V. Samsonov and I.M. Vinitskii, *Handbook of Refractory Compounds*, IFI/Plenum Press, New York, 1980.

[Sc-81] D.M. Scott and M.A. Nicolet; *Phys. Stat. Sol.* (a), (1981) 773.

[Sc-81(a)] D.M. Scott and M.-A. Nicolet; Nucl. Instr. and Meth., 182/183 (1983) 655.

[Sc-82] D.M. Scott; *The effects of oxygen on the formation of Ni Pd and silicides,*

PhD. Thesis, Caltech, Pasadena, California, 1982.

[Sh-81]   T. Shibata. *IEDM Tech.* digest 647 (1981).

[Su-73]   K.E. Sandström, S. Peterson and P.A, Tove; *Phys. Solid State A*, **20** (1973) 653.

[To-51]   K. Toman, *Acta Cryst.*, **4** (1951) 462.

[Ts-81]   B.Y. Tsaur, S.S. Lau, J.W. Mayer, and M.-A. Nicolet, *Appl. Phys. Lett.* **38**, 922 (1981).

[Tu-74]   K.N. Tu, E. Allessandrini, W.-K. Chu, H. Kräutleand J.W. Mayer. *Jpn J. Appl. Phys.*, Suppl. 2 Part 1 (1974) 669.

[Tu-75]   K.N. Tu, W.K. Chu and J.W. Mayer; *Thin Solid Films*, **25** (1925) 403.

[Tu-77]   K.N. Tu; *J. Appl. Phys.*, **48** (1977) 3379.

[Tu-78]   K.N. Tu and J.W. Mayer in *Thin Films Interdiffusion and Reactions*, edited by J.M. Poate, K.N. Tu and J.W. Mayer (Wiley-Interscience, New York, 1978).

[vA-80]   M.von Allmen, S.S. Lau, D.M Scott, J.W. Mayer, W.F. Tseng, T.T. Tseng, P. Williams and J.E. Baker; Proc. Symp. *Thin Film Interfaces and Interactions*, ed. by J.E.E. Baglin and J.M. Poate, Electrochem. Soc., val **80**-2 (1980) 195.

[vdH-88]   L van den Hove *"Advanced Interconnection and contact schemes based on TiSi₂ and CoSi₂:* Relevant Materials Issue PhD Thesis Universiteit Leuven, June (1988).